Title

Arctic ocean long-term acoustic monitoring : ambient noise, environmental correlates, and transients north of Barrow, Alaska

Author

Roth, Ethan H.

Publication Date

2008

UNIVERSITY OF CALIFORNIA, SAN DIEGO

Arctic Ocean Long-Term Acoustic Monitoring:
Ambient Noise, Environmental Correlates, and Transients North of Barrow, Alaska

A Thesis submitted in partial satisfaction of the requirements
for the degree Master of Science

in

Engineering Science (Applied Ocean Sciences)

by

Ethan H Roth

Committee in charge:

Professor John Hildebrand, Chair
Professor Carl Gibson
Professor Stefan Llewellyn Smith

2008

The Thesis of Ethan H Roth is approved and it is acceptable in quality and form for publication on microfilm and electronically:

Chair

University of California, San Diego

2008

This thesis is dedicated to
Donald Ross
for his mentorship, guidance, and friendship.

“Our culture, the very deepest part of our being, rises or falls with the fate of the whales and seals and other species in Arctic waters. The ancient values that define us as a people are transmitted through participation in traditional whaling and hunting activities. If we lose the hunt, we lose our identity. It's that simple.”

Edward Itta,
North Slope Borough Mayor & Inupiat Whaling Captain

TABLE OF CONTENTS

LIST OF FIGURES

ACKNOWLEDGEMENTS

I would like to acknowledge John Hildebrand for his support as my graduate advisor, and Sean Wiggins for his guidance over the past few years. The SIO Whale Acoustics Lab has been an amazing learning environment because of the people comprised within it. Beve Kennedy especially helped to make this work possible.

I couldn’t ask for a better mentor than Don Ross, or a better friend than Josh Jones.

I would like to thank Robert Small, from the Alaska Department of Fish & Game, for his support and sponsorship of this project. Hopefully the work we’ve started will continue to grow with our endeavor to observe and understand the changes taking place in the Arctic.

Thanks to Caryn Rea from Conoco-Phillips, for her logistical support that made the 2006 instrument deployment possible. Thanks to Larry Mayer from CCOM-UNH, for his generous logistical support that made the 2007 recovery and redeployment possible, and soon to be the same in 2008.

I’d like to especially acknowledge the crew members of the USCGC Healy and M/V Torsvik, for helping to make this field work possible in such an extreme and remote environment. Thanks to the Barrow Arctic Science Consortium for providing shelter, food, and good company on land.

I would like to thank Mati Kahru for helping me obtain sea ice satellite data to work with in his software package, Windows Image Manager.

ABSTRACT OF THE THESIS

Arctic Ocean Long-Term Acoustic Monitoring:

Ambient Noise, Environmental Correlates, and Transients North of Barrow, Alaska

by

Ethan H Roth

Master of Science in Engineering Science (Applied Ocean Sciences)

University of California, San Diego, 2008

Professor John Hildebrand, Chair

The Arctic Ocean has experienced wide-spread decreases in sea ice concentrations that may impact various marine ecosystems. This study analyzes yearlong ocean acoustic recordings from north of Barrow, Alaska, to provide baseline measurements prior to possible increases in anthropogenic activities. In September 2006, two autonomous High-frequency Acoustic Recording Packages (HARPs) were deployed to the seafloor (250m), where sound was continuously recorded by hydrophones for nine months. Ice conditions during the recordings included open water, pack ice formation, shore-fast canopies, and thermal breakup, providing a wide range of Arctic Ocean acoustic measurements.

Spectral-averaging was used to determine received sound-pressure levels. Across the low-frequency band, fall was the noisiest season, reaching 87dB re µPa between 20–60Hz, while 10% of October was exposed to noise above 130dB re µPa at 10Hz and 112dB re µPa between 20–30Hz; seismic airguns were present from September to November. Acoustic data was compared with sea ice concentration and wind speed; during summer and fall, sound-pressure spectrum levels correlate directly with high wind speeds, typically indicative of low-pressure atmospheric events. Throughout winter and spring, strong winds and thermal fracturing in sea ice opens leads, resulting in correlations with spectral energy-peaks.

Bioacoustic recordings of cetaceans and pinnipeds were analyzed using long-term spectral-averages to determine presence or absence on an hourly basis. Combined with ancillary measurements, long-term acoustic monitoring is an effective tool for observing changing levels of ambient sound related to sea ice dynamics, environmental noise-generating mechanisms, and anthropogenic noise, while simultaneously detecting marine mammals.

I. INTRODUCTION

Current State of the Arctic Ocean

The summer of 2007 set a new record low for Arctic sea ice extent (see Figure 1.1), leaving the environment on the verge of a fundamental shift towards seasonal ice cover, which may be realized as early as 2030 (Stroeve et al, 2007). Multiyear ice has been disappearing and being replaced by newly formed frail and thin seasonal ice that is more easily disturbed by low-pressure winds and warmer sea temperatures. Recently, some 965,300 square miles of perennial ice have been lost — a 50% decrease between Feb. 2007 and Feb. 2008 (Meier quoted by Kaufman, 2008).

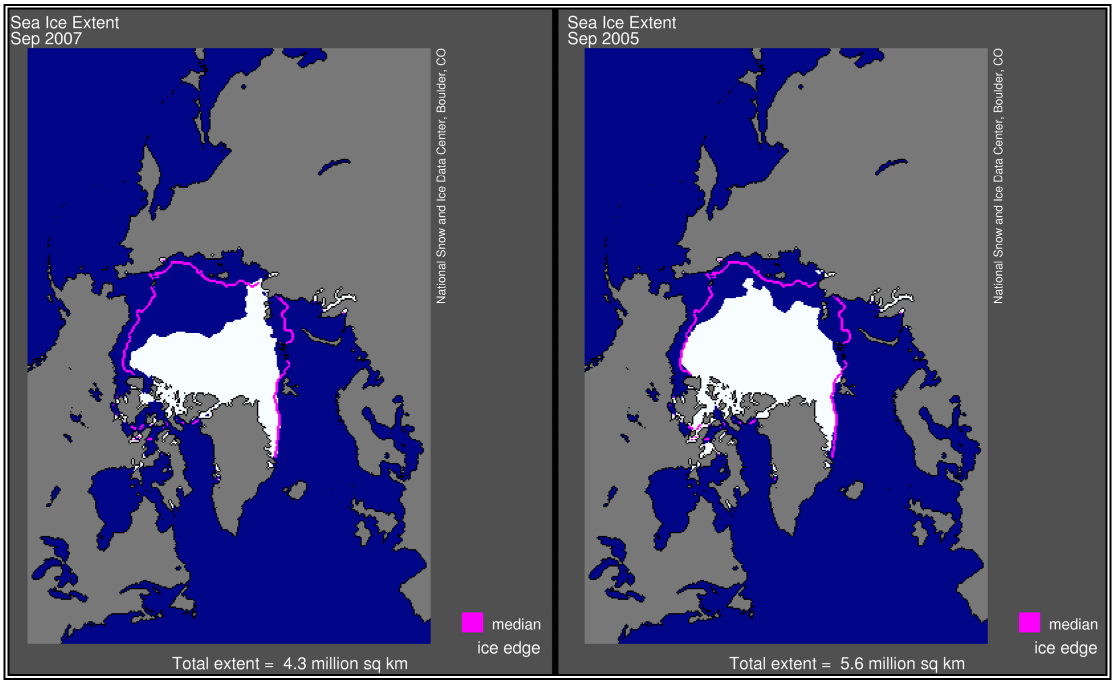

Figure 1.1 – A comparison between the average sea ice extent for September 2007 and September 2005; the magenta line indicates the long-term median from 1979 to 2000. September 2007 sea ice extent was 4.28 million square kilometers (1.65 million square miles), compared to 5.57 million square kilometers (2.14 million square miles) in September 2005. This image is from the NSIDC Sea Ice Index.

Computer models suggest Arctic sea ice is a sensitive climate indicator, demonstrating how the rise in global temperatures may accelerate further reductions in ice cover. An important factor that has contributed to sea ice extent minimums in recent years is the weakened and thinner state of spring ice, which takes less thermal energy to melt than thick multiyear ice. Another factor that was particularly significant during the summer of 2007 was an unusual atmospheric pattern, with persistent high atmospheric pressures over the central Arctic Ocean and lower pressures over Siberia. Clear skies under the high-pressure cell and wind patterns pumping warm air into the region promoted strong melt while pushing ice away from the Siberian shore (Stroeve et al, 2007).

For the first time in human-recorded history, the Northwest Passage was completely open, bolstering the vision for a shorter sea route between the Pacific and Atlantic Oceans. On the other hand, the Northern Sea Route along the Eurasian coast was completely blocked by a band of ice. As the Arctic system continues to warm, spring melt will come earlier and fall ice formation will begin later, extending the length of the summer melt season. This has already begun to affect native subsistence hunting, made traveling across tundra difficult, and buildings on permafrost unsafe.

The recent widespread decreases in sea ice concentrations may severely impact marine ecosystems, which makes it imperative to establish baseline acoustic measurements for ambient noise levels in the Arctic underwater environment prior to possible increases in Arctic anthropogenic activities. By initiating a study across large temporal scales, it’s possible to determine the sources of sound that are attributed to different seasonal variations. Long-term acoustic monitoring can help to fully understand these changes, as year-long data collection exploits the seasonal variability of sea ice in a specific region. Local contributions to the soundscape include sea ice, wind, biological vocalizations, and anthropogenic sources of noise such as seismic oil exploration and shipping activities. To fully understand the unique noise-generating mechanisms inherent to the Arctic Ocean environment, it’s useful to examine what past studies have been conducted.

Underwater acoustics in the Arctic Ocean was given a great deal of attention during the Cold War due to the fear of submarine warfare in the circumpolar north. Sonar detection algorithms used in open ocean conditions were not well adapted to deal with the highly-impulsive, non-Gaussian nature of ambient noise distinct to an ice-covered environment. The role of a dynamic sea ice boundary in dictating the seasonal variation of acoustic propagation was poorly understood. Several acousticians carried out field experiments to identify and describe the transient sources of noise generation that correspond with the different spatial and temporal characteristics of sea ice. In addition, a great deal of theoretical work focused on propagation modeling to understand the effects that under-ice scattering strength and reflection loss had on sound transmission. It was found that the physical mechanisms attributed to sea ice dynamics serve as both the principal control of sound propagation over long ranges, as well as the dominant noise source in the local region.

Arctic Ambient Noise

Underwater ambient noise is described as the composite noise arising from all sources in the sea (Kibblewhite and Jones, 1976) as well as processes occurring at or above the sea surface. Urick identified surface waves, rain, biological activity, oceanic turbulence, shipping and other anthropogenic noise, seismic disturbances, thermal noise, and most significantly the hydrostatic effects of tides and waves as sources of ambient noise in the deep ocean (see Figure 1.2). When introducing sea ice as an upper boundary layer, it is the sea ice itself that governs underwater ambient noise levels. While the sources described by Urick are still present, ice cover on the surface can effectively inhibit these mechanisms from contributing to underwater noise, especially the generation of wind-driven surface waves. On the other hand, sea ice acts as an interface between the atmosphere and ocean, inducing noise through perpetual mechanical changes that are influenced by variations in temperature and wind speed. For this reason, sea ice is also a significant noise source and at high frequencies contributes to excess noise above the thermal noise threshold (Kibblewhite and Jones, 1976).

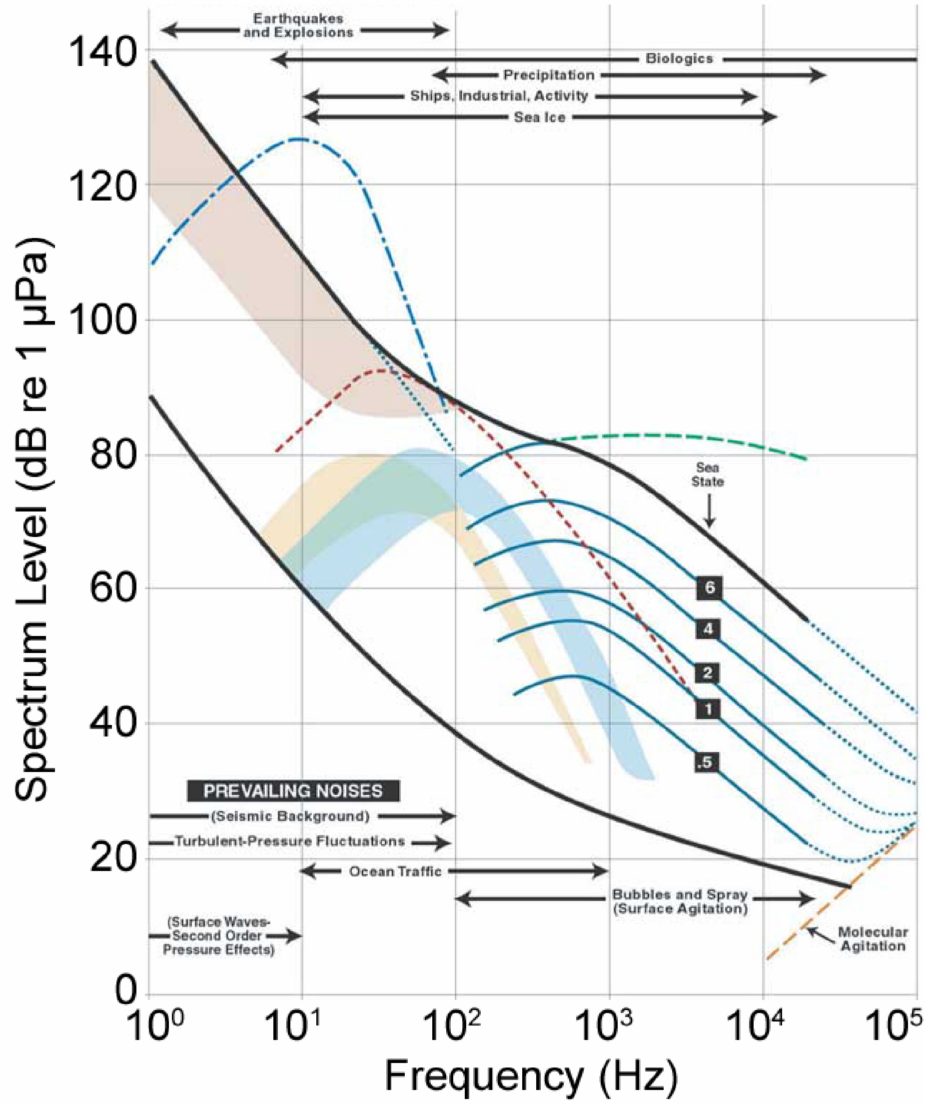

Figure 1.2 – Typical sound-pressure levels of open ocean ambient noise, as measured by Wenz (1962). Reprinted from the National Research Council, 2003 – Ocean Noise and Marine Mammals.

The Arctic waveguide is typically defined by a nearly isothermal water column, an ice canopy at the sea surface that is spatially and temporally variable, and a positive sound speed gradient. Acoustic ray paths are usually refracted upwards and subsequently reflected and scattered from the rough underside of sea ice, as illustrated in Figure 1.3. Even low-frequency (10-100 Hz) transmission loss is more substantial than most free-surface scattering theories since acoustic waves interfere regularly due to this strongly upward refracting surface duct (LePage and Schmidt, 1994). Reflection loss is not only a function of frequency but depends on the change in density between the interface of two mediums (i.e. water-air or water-ice), as well as the depth of the ice (Diachok, 1976).

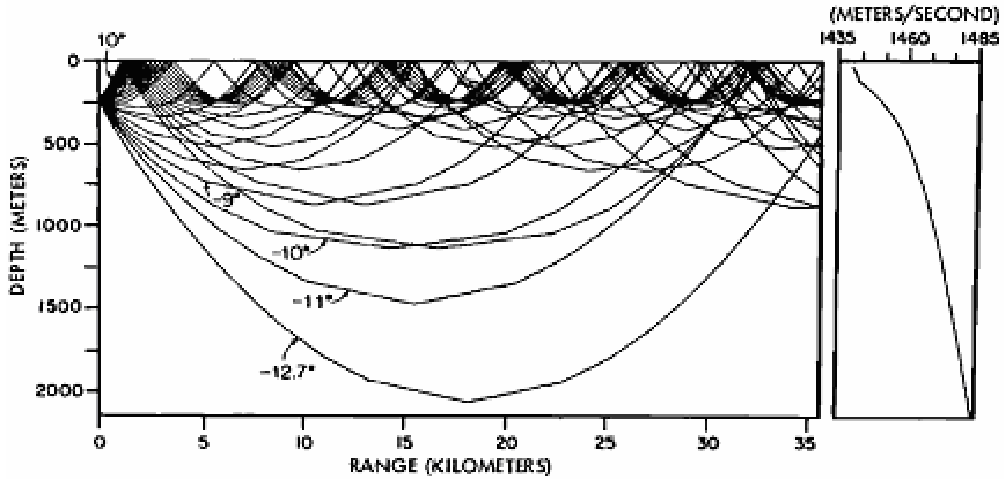

Figure 1.3 – Typical ray diagram and corresponding sound-speed profile for acoustic propagation in the Arctic Ocean (Diachok, 1976).

Ambient noise is unusually impulsive and highly non-Gaussian in contrast to uniform, open ocean ambient noise measurements. Spectra exhibit noise levels that are not exceptionally low though, especially in winter when pressure levels are equivalent to sea-state three conditions (Milne and Ganton, 1964). Comparing sound-pressure levels for thermally-generated under-ice noise with those of open-ocean noise can be misleading, since the nature of the two signals is so different. Ambient noise levels are highest in the marginal ice zone and decrease rapidly with distance from the ice edge into the ice field more so than into open water. Under the cover of a hardened ice canopy, ambient noise levels are consistently lower than open ocean noise levels (Diachok and Winokur, 1974). Under continuous shore-fast ice cover and rising air temperatures, noise levels between 10-1000 Hz can be up to 25 dB below those observed for sea state zero in the open ocean (Kibblewhite and Jones, 1976).

Acoustic Monitoring from the Seafloor

For an ambient noise study, it's essential to ask from what direction an omni-directional hydrophone receives most transient signals. If a hydrophone is positioned on the seafloor off the slope of the continental shelf (done for safety reasons to avoid ice scours and pock marks), is it more exposed to acoustic propagation from the shelf or the deep ocean? (see Figure 1.4)

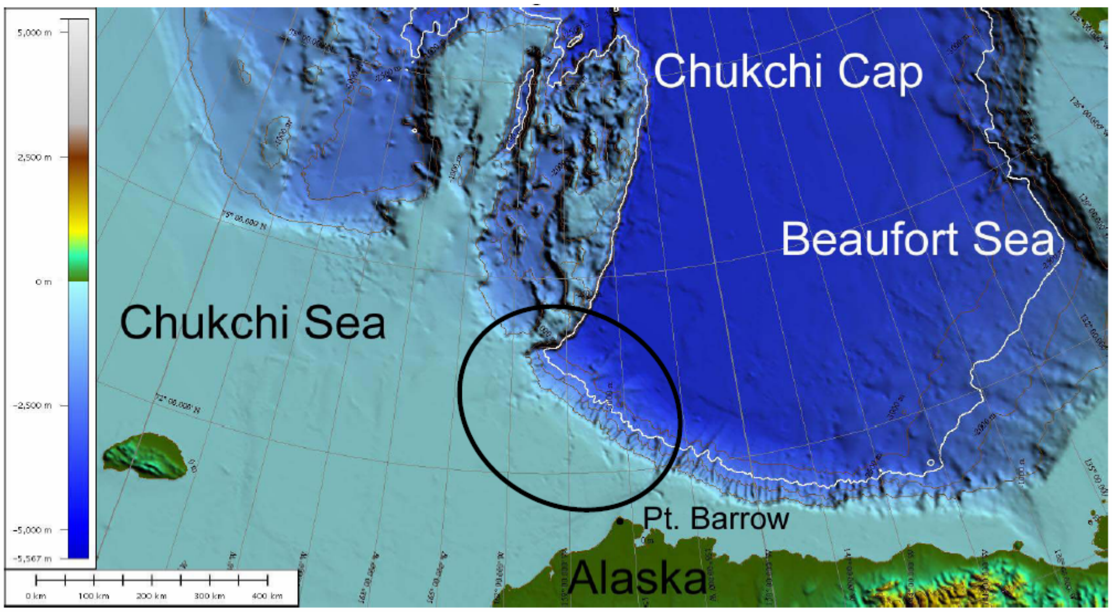

Figure 1.4 – Study Area: shallow vs. deep ocean acoustics

Spherical and cylindrical spreading are two simple approximations used to describe how sound pressure levels decrease as a sound wave propagates away from an acoustic source (see Figure 1.5). Spherical spreading describes the decrease in pressure level when a sound wave propagates away from a source uniformly in all directions. This situation occurs for an acoustic source at mid-depth in the deep ocean, and the magnitude of intensity decreases as the inverse square of the range. Beyond some range the acoustic wave eventually hits the sea surface or sea floor. A simple approximation for spreading loss in a medium with upper and lower boundaries can be obtained by assuming the sound is distributed uniformly over the surface of a cylinder.

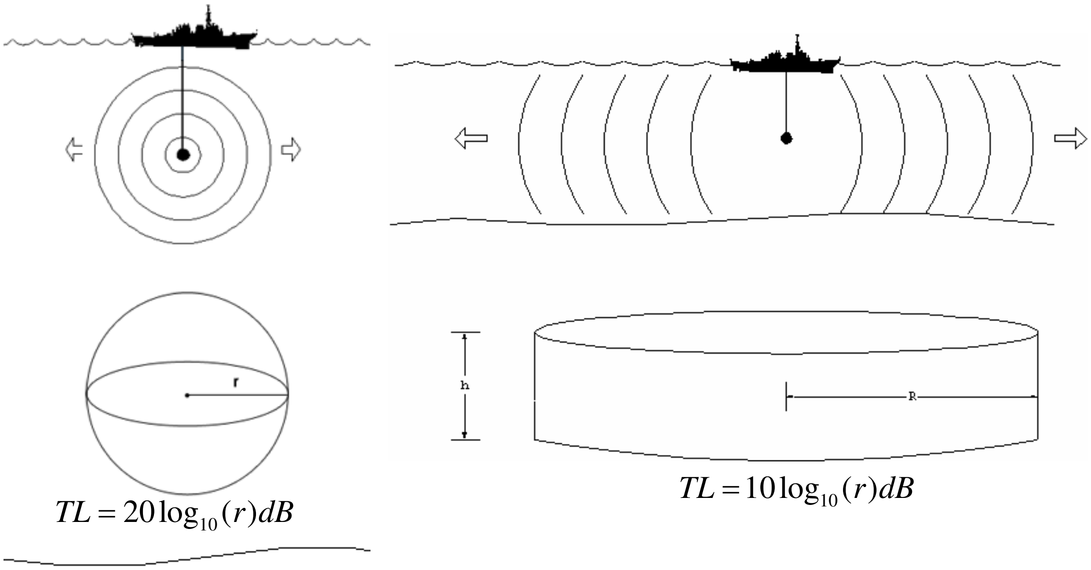

Figure 1.5 – Spherical vs. Cylindrical Spreading

In the ice-covered Arctic, transmission loss is much greater than cylindrical spreading. Due to the surface duct formed by a shallow thermal gradient, sound waves tend to refract off the duct and propagate towards the surface, which then reflect off the underside of rough ice, characteristic of high scattering strength. Therefore sound will attenuate rapidly the more it reflects off the ice, and as frequency increases so does reflection loss and surface scattering. This suggests high frequency sound cannot travel across long distances and the hydrophone is mostly receiving locally produced noise at high frequencies. Reflection and transmission coefficients are generally proportional to the thickness of sea ice, and as a result determine the frequency-dependent shape of the ambient noise spectrum (Diachok & Winokur, 1974).

As a theoretical exercise, several models were developed using the underwater acoustic propagation modeling software AcTUP V2.2L (A. Maggi and A. Duncan, Curtin University of Technology) in MatLab. Since the goal is to replicate the continental shelf sloping down to abyssal bathymetry, the RAMGeo algorithm was used because it provides a fully range dependent parabolic equation code for a fluid seabed. Figure 1.6 is a model simulation with an open water upper boundary. The shallow water source at 20 meters depth is transmitting 50 Hz across a range of 30 kilometers; the receiver is positioned on the slope just off the shelf at approximately 250 meters depth. Acoustic energy propagates very well in a shallow waveguide and channels it through the upper layer of the deep ocean.

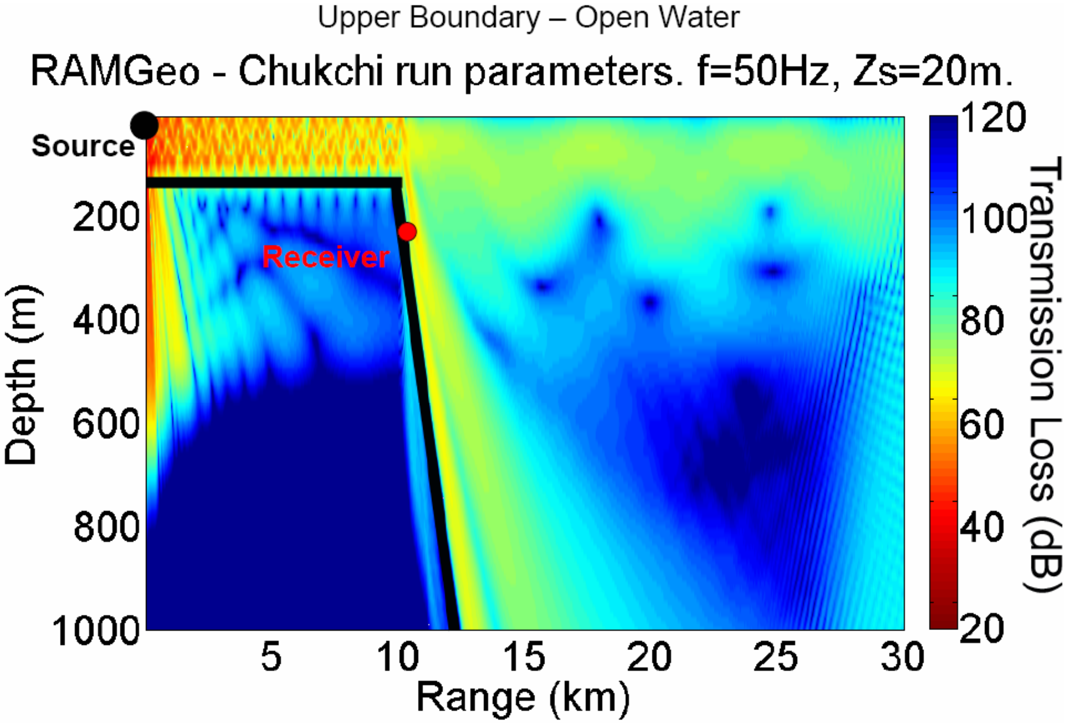

Figure 1.6 – Propagation Model with shallow source and open water surface layer.

Figure 1.7 illustrates a propagation model where sea ice is the upper boundary layer with properties of 4 meters thickness and 2 meters roughness (i.e. frequency dependent, high scattering strength). Transmission loss increases much faster by the time 50 Hz propagates across the shallow shelf waveguide and disperses once it enters the deep ocean; the hydrophone still appears to receive some of that sound transmission though, which is important since many transient acoustic events occur on the shelf.

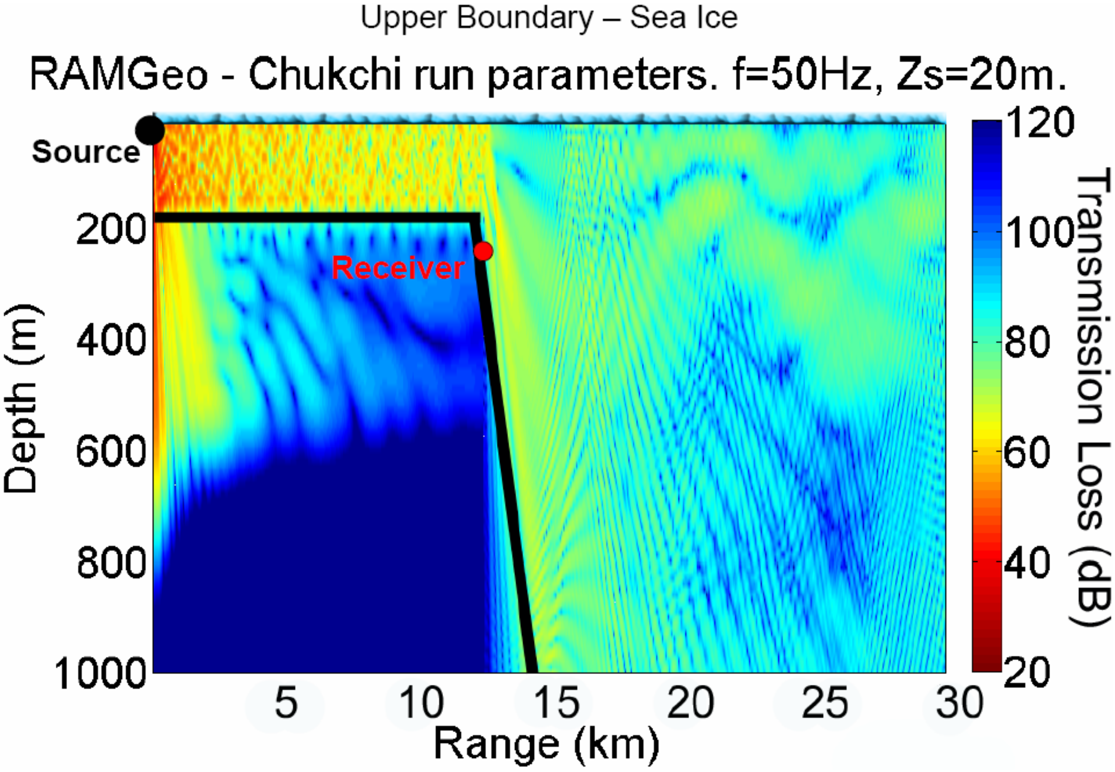

Figure 1.7 – Propagation Model with shallow source and ice-covered surface layer.

The model in Figure 1.8 still has sea ice as the upper boundary layer, but now the source is placed in deep water and transmits towards the receiver on the shelf slope. In this scenario, the hydrophone receives more multipath propagation from lower frequencies. Due to upslope conversion, not much acoustic energy will converge up onto the shelf. Perhaps background ambient noise measurements are representative of both the continental shelf and the deep ocean, with more multipath from the deep, while more localized and impulsive acoustic events are received from the shallow shelf near to the hydrophone receiver.

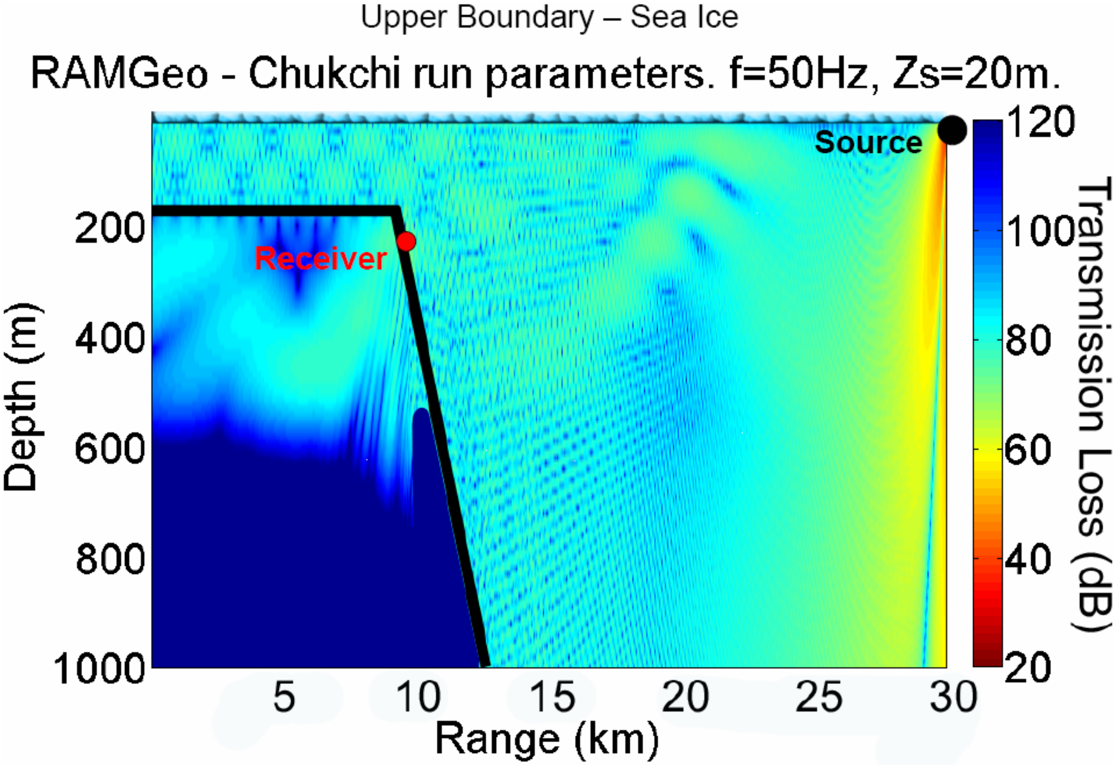

Figure 1.8 – Propagation Model with deep source and ice-covered surface layer.

Baseline Study

There have been few comprehensive long-term comparisons between underwater acoustic pressure levels and sea ice dynamics (Squire et al., 1995). Before the advent of long-term monitoring technology, in order for acousticians to determine if the Arctic ambient noise environment was uniquely anisotropic, it was necessary to examine the dependency of specific source locations of noise in relation to the dynamic state of sea ice (Greene and Buck, 1964). This was generally done on ice camps while moving with the drifting floe pack, suspending hydrophones a few meters below the ice. Milne towed hydrophones across the Beaufort seafloor at depths of 451 m; Lewis and Denner deployed an array of drifting buoys in the Beaufort Sea, providing one of the most complete records of long-term variability and spatial coherence of low-frequency sound in the Arctic (Webb, 1992). Autonomous monitoring from the seafloor allows one to not only understand the spatial variability, but more importantly the temporal variability that controls the relationship between ambient noise and sea ice. What makes a continuous dataset like this so crucial, especially at this point in time, is the fact that since 2005 there has been extremely pronounced declines in sea ice concentrations.

The primary objective for the first-year of this study is to establish and characterize long-term baseline measurements for underwater ambient noise north of Pt. Barrow, Alaska, while examining the variability and distinct mechanisms that are inherent in the different seasons. The broader purpose of this first-year study is to have a baseline for which to compare future data from continuing instrument deployments. The aim is to maintain autonomous, long-term acoustic data collection at sites around the North Slope of Alaska for the next several years, and develop an extensive time series where inter-comparison can reveal shifts in seasonal trends. The time-variant impact of sea ice decline due to climate change provides adequate motivation for a long-term study of this nature. It seems plausible that the continual thinning and disappearance of sea ice will effectively reduce transmission loss and thus alter underwater propagation during several months that have not previously been exposed to acoustic sources such as anthropogenic noise. Seismic oil exploration and increased shipping activity may possibly contribute to significant increases in ambient noise levels. By initiating the experiment in 2006, it will still be feasible to use future data to help monitor possible shifts in the acoustic baseline and determine the transient sound sources and noise-generating mechanisms associated with noise augmentation in the underwater sound environment.

During the summer of 2006, seismic activities associated with oil exploration and other types of man-made noise contributed significantly to low-frequency ambient noise levels. Fall is distinctly characterized by environmental noise such as pressure ridging associated with ice-floe interactions, in addition to storm-generated winds. The onset of low temperatures in early winter – when the Arctic Ocean is fully covered with shore-fast pack ice – bring about localized thermal fracture noise; the composite of these impulsive events exhibits a near-normal Gaussian distribution. In late winter and spring, ambient noise is characterized by fewer impulsive events, so while thermal fracturing is still present in addition to man-made noise, the background noise continually decreases until reaching its lowest levels in May. Analyzing the fluctuating trends in sound-pressure spectrum levels throughout nearly an entire year helps to understand the effects of declining sea ice concentrations in the region, providing the groundwork to observe changes in acoustic propagation as the current trend continues.

The methods which made this data collection possible will be described, including details that outline the instrumentation used and subsequent field work.

Sensor calibration was performed since ambient noise measurements are represented as received pressure levels. Data analysis methods included digital signal processing and spectral averaging in MatLab, and there was additional consideration for electronic noise issues. Spectral curves are represented as monthly averages for background noise levels as well as statistical density distributions that include all transient signals.

Time series analysis was performed on sea ice concentration data from the NASA AMSR-E satellite and wind speed data from a NOAA meteorological station in Barrow. These are compared with time series of acoustic data – analyzed at different frequencies in spectral space – to investigate possible correlations between sound and the dynamic underwater environment. Several cetacean and pinniped species were recorded, including bowhead and beluga whales, ringed and bearded seals, and walrus. Long-term spectral-averaged time series indicate the presence or absence of three species on an hourly basis in addition to investigating vocal repertoires throughout varying seasonal periods. It will be shown that combined with ancillary measurements, long-term acoustic monitoring provides an effective tool for observing changing levels in ambient sound related to sea ice, wind, anthropogenic noise, and can simultaneously detect marine mammals.

II. METHODS

HARP Instrumentation

Two autonomous, seafloor High-frequency Acoustic Recording Packages (HARPs) were assembled and deployed for this experiment with the goal of recording sound for an entire year; the instrumentation was similar to that described by Wiggins (2007). The three main categories of components that make long-term acoustic data collection possible are the hydrophone sensor (32 kHz sampling), data-logging system, and instrument packaging.

A passive acoustic hydrophone has been designed to be broad-band in frequency, have high sensitivity (i.e. increased gain), and low self (i.e. system) noise. Sensor components include two types of transducers and a pre-amplifier circuit board housed inside a pliable polyurethane tube (Φ_{OD} = 2 inches), and immersed in inert mineral oil to match the acoustic coupling impedance of water (see Figure 2.1). In order to achieve substantial dynamic range over such a broad range of frequencies, it's beneficial to split the hydrophone element into two separate channels and combine them later. A bundle of six Benthos AQ-1 cylindrical transducers connected in series was used for the 10-3000 Hz band and provide a total sensitivity of approximately -187 dB re 1 $V_{rms}/\mu Pa$ with a flat response (+/- 1.5 dB). One omni-directional ITC-1042 spherical transducer was used for the 1-16 kHz band and has a flat (+/- 2 dB) sensitivity response of about -200 dB re 1 $V_{rms}/\mu Pa$. As acoustic pressure waves propagate through the transducer elements, piezoelectric crystals inside the hollow ceramics are electrically excited by compression, and in turn emit a small analog voltage signal. Treating a transducer like an electric capacitor, the voltage potential can be measured between two wires soldered to the inside and outside of the ceramic.

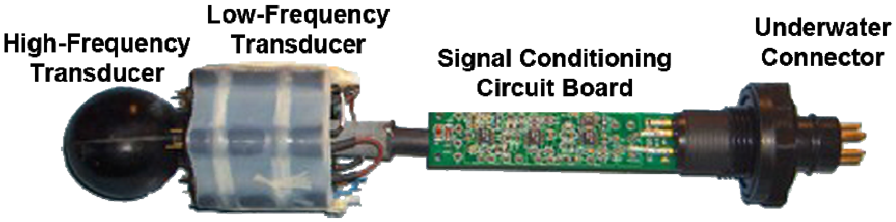

Figure 2.1 – The hydrophone sensor components consist of one ITC-1042 and six Benthos AQ-1 transducers, a custom-designed pre-amplifier, and Impulse underwater connector (Wiggins, 2007).

Two signals are then inputted into separate stages of the pre-amplifier (i.e. signal conditioning) circuit board. The board must be positioned as close as possible to the transducers to avoid creating an antenna for electronic noise. Approximately 40 dB of gain is added to the low-frequency stage and 80 dB to the high-frequency stage. The goal is to pre-whiten the signals so their frequency response is similar to the reciprocal of ocean ambient noise. In general, more gain is added at higher frequencies where ambient noise levels are lower and sound attenuation is higher (Wiggins, 2007). High-pass filters on both stages create low-end roll offs below 30 Hz on the low-frequency stage and below 10 kHz on the high-frequency stage. A 4-pole low-pass (i.e. anti-aliasing) filter reduces high-frequency aliasing effects above 2 kHz for the low-frequency stage and above 100 kHz for the high-frequency stage.

Amplified signals travel through a 10 meter underwater cable and bulkhead connector to a differential receiver onboard the datalogger, where the two stages of the analog sensor signal are mixed and passed through another 4-pole low-pass filter with a -3 dB rolloff point at 16 kHz, further reducing any possible high-frequency aliasing effects. The filtered signal is converted into digital data using a low-power, low-noise Analog-to-Digital Converter from Analog Devices. The A/D circuit board provides 16-bit resolution and up to 250,000 samples/second sample rate. Also included on the A/D card is a power supply (+5 V) for the low-power hydrophone sensor (50 mW).

The datalogger CPU card is a 32-bit, 20 MHz micro-controller from Motorola, and runs all processes onboard the datalogger (see Figure 2.2). The CPU circuit board contains FLASH memory for data buffering, and a RS232 transceiver for a HARP user to communicate with and program the datalogger through a standard computer terminal with a serial communications port. After the sensor data has been digitized, the CPU passes the binary information to the SRAM circuit board, which consists of 32 MB for data buffering. Once 30 MB of this space has been filled, the Ethernet/IDE card spins up a hard disk and writes the SRAM buffer into a 60,000 block binary file, while the A/D converter continues to fill up the data buffer from the back end. Each datalogger has 16 integrated drive electronics (IDE) laptop disk drives (2.5” form-factor), each with 120 GB of capacity (1.92 TB total). While all the disks are arranged in a block, each disk is addressed and powered one at a time, in sequential order; this maintains low-power consumption in the datalogger.

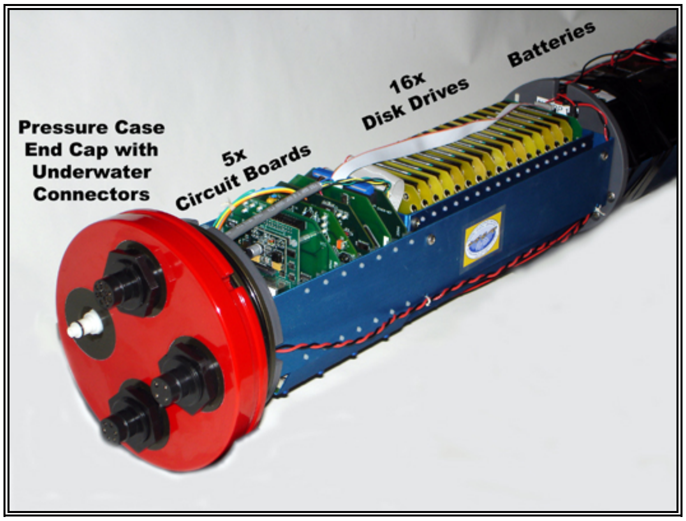

Figure 2.2 – The datalogger components consist of a CPU, A/D converter, RAM buffer, clock card, and IDE controller for sixteen 120 GB hard drives (Wiggins, 2007).

For data evaluation in the field, the Ethernet/IDE circuit board also provides 10BaseT file transfer protocol (FTP) and telnet connectivity in order to upload individual 30 MB files from a datalogger hard disk. The fifth circuit board housed inside the datalogger is a Clock card, populated with a temperature compensating phase-lock circuit and a low-power Seascan clock oscillator module which provides low, long-term clock drifts on the order of 1 part in 10^{-8}. Precise clocks are beneficial when sensors are deployed in an array configuration and the measured difference in arrival times of transient signals can be useful for various signal processing techniques (i.e. tracking).

Both storage capacity and battery life dictate the monitoring duration and sampling rate of a HARP (Wiggins, 2007). 1.92 TB of data storage capacity allows for approximately one year of recording duration if sampling continuously at 32 kHz. For this particular instrument configuration, a total of 336 D size alkaline cells (140 grams each) are arranged into five sub-packs. Housed within a separate pressure case composed of 7075 aluminum, four of the sub-packs contain 72 D cells arranged in four layers of 18 cells. The fifth sub-pack is housed along with the electronics inside the datalogger pressure case (6061-T6 aluminum), and contains 48 D cells arranged in four layers of 12 cells. Each sub-pack provides 12 volts of power by assembling either nine or six parallel strings of 8 cells in series. All the sub-packs are connected in parallel; power is transferred from the battery pressure case housing to the datalogger using an underwater cable and bulkhead connectors from Impulse.

From this configuration of forty-two 12 volt strings, an estimated 588 Amp-hours were available for the deployment. It was overlooked though that operating temperatures for depths greater than 100 meters in the Arctic Ocean reach as low as -2° C, while environmental conditions required for alkaline batteries to operate efficiently are rated for 0° C and above. The consistent cold temperature “drained” the battery voltages faster than anticipated; at the same time, the hard disks required more current draw than usual in order to “spin up” in cold temperatures. At some point during the deployment, the batteries could no longer provide sufficient current for digitized data to be written to the hard disks. This occurred on January 31, 2007 for Site A, and on May 30, 2007 for Site B.

Seafloor packages are easy to deploy and recover from mid-sized research, fishing, or merchant vessels. The frames for these seafloor packages were originally used to deploy an older generation of Ocean Bottom Seismometers. They are constructed of fiberglass bars fastened together into a rectangular frame with approximate dimensions 66 in. by 32.5 in. by 40.25 in. high (see Figure 2.3), and contain a compact arrangement of mounted flotation, mooring ballast, and release system. Flotation consists of eight Benthos 17" glass spheres housed in polyethylene hard hats, and rated to 6000 meters depth. Each sphere provides 56 pounds of buoyancy (448 pounds total), a majority of which is necessary due to the weight of the batteries. A two-inch thick steel plate weighing approximately 340 pounds is rigidly fixed to the bottom of the seafloor frame by securing it to two EG&G acoustic releases. The OBS package is also where the datalogger and battery pressure cases are mounted, while the hydrophone sensor is tethered 10 meters above the instrument frame to provide a quieter acoustic background than near the sea surface.

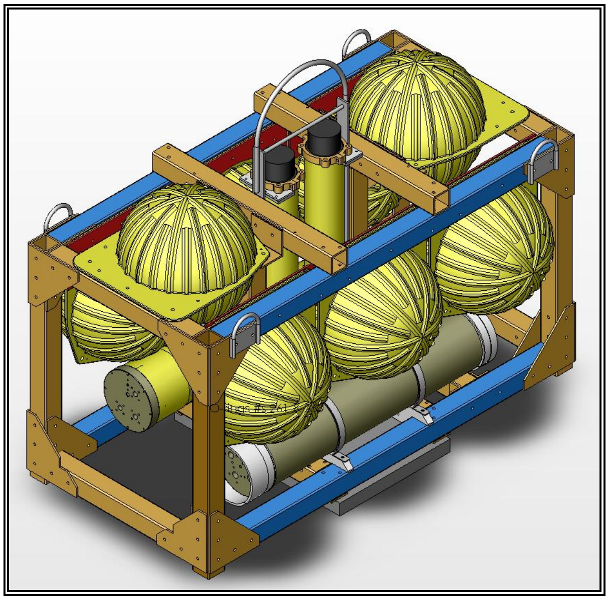

Figure 2.3 – The seafloor package components consist of glass-sphere flotation, acoustic transponder releases, and ballast weight, in addition to housing the datalogger and battery pressure cases.

Field Work & Data Collection

On September 25, 2006, two autonomous HARPs were deployed to the seafloor – approximately 250 meters deep – due north of Point Barrow, Alaska in the Chukchi Sea (see Figure 2.4). The field work effort was aided by Conoco-Phillips Oil

Exploration, who provided logistical support and use of their seismic chase boat, the M/V Torsvik. While scouting the southern edge of the Marginal Ice Zone (MIZ), both instruments were deployed along a contour of the slope dropping off the northern edge of the continental shelf. The HARP at Site A was deployed at location 72° 10.569 N, 156° 33.176 W, at a depth of 230 meters, and Site B was deployed at location 72° 27.523 N, 157° 23.364 W, at a depth of 246 meters. This was the farthest north the Torsvik would navigate due to rough packs of sea ice scattered around the region, and the fact that the Torsvik did not have an ice-hardened hull.

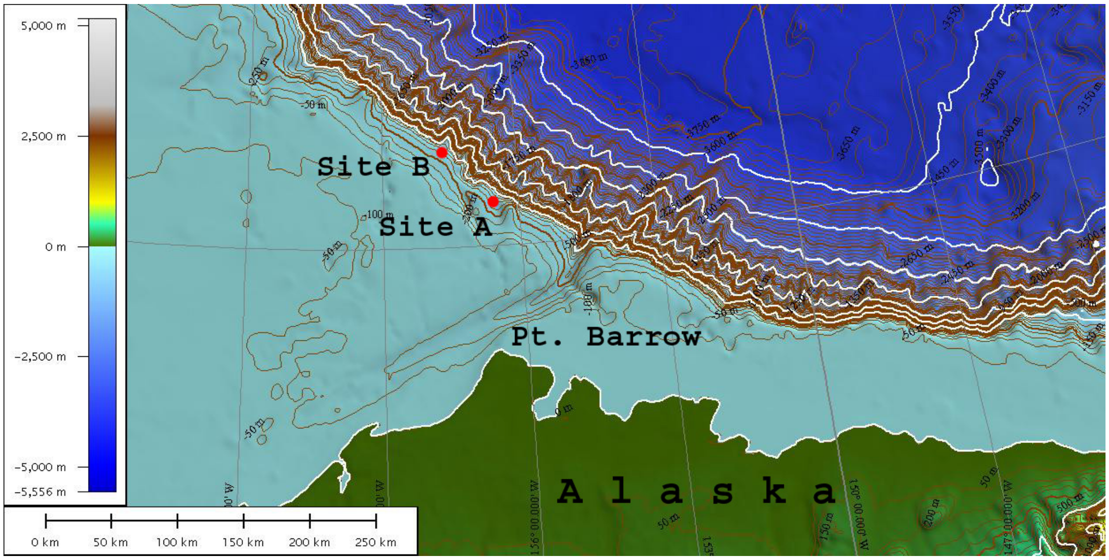

Figure 2.4 – HARP instrument locations: Site A (72° 10.569 N, 156° 33.176 W, 230 m depth) and Site B (72° 27.523 N, 157° 23.364 W, 246 m depth). Map courtesy of Larry Mayer, CCOM-UNH.

Most of the Chukchi Sea is relatively shallow (50–100 meters), which raises many concerns when assessing the risk involved in leaving a HARP on the seafloor for an entire year. Besides the fact that more oxygenated seawater leads to an increased rate of metal corrosion, there is always the possibility an ice keel – formed through pressure ridging – can scour the seafloor, leaving a deep pockmark. High resolution imagery acquired from multibeam sonar data suggests that there are several ice scours on the seafloor in the vicinity of Point Barrow. The instrument locations were chosen to avoid these pockmarks and be on the edge of the continental shelf drop-off so that the hydrophones would record both shallow water sound propagation from the eastern Chukchi Sea and deep ocean (~4000 meters) acoustics from the western Beaufort Sea.

Both HARPs were successfully recovered on August 17, 2007 aboard the United States Coast Guard Cutter Healy, a heavy-class icebreaker used for polar research. At each site, the ship's 12 kHz hull transducer was used to transmit a series of coded sonar pings to the EG&G acoustic release onboard the HARP. Measuring the time of arrival between acoustic communications and approximating the speed of sound allows for reasonable slant range estimation. Transmission of a final release command triggered a solenoid firing mechanism and released the ballast weight, allowing the positively buoyant HARP package to float up to the sea surface (see Figure 2.5). Once sighted at the surface, a small rib boat maneuvered toward the packages and towed them to Healy's starboard quarter, where a crane transferred the instruments onto the fantail deck. The HARPs were evaluated for data quality, all necessary hardware was refurbished, and the instruments were redeployed on September 14, 2007 for another year of autonomous recording.

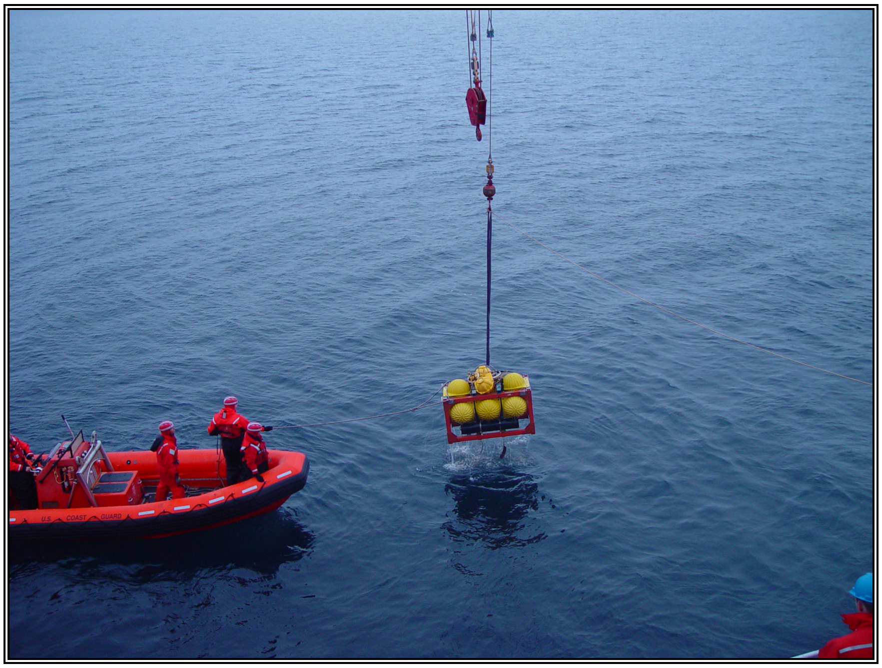

Figure 2.5 – After the ballast weight is released, the HARP floats to the surface and is recovered aboard the Healy.

During both the deployment and recovery cruises, with ice conditions permitting, a contingent of expendable Sparton AN/SSQ-57SPC sonobuoys were deployed to opportunistically record marine mammal vocalizations and underwater sea ice events. Activated by a seawater battery, sonobuoy hydrophones convert underwater sound waves into electrical signals, which are amplified and frequency modulated for real-time VHF transmission through a radio transmitter on the surface float to an omni-directional antenna positioned atop the vessel's radio mast. A VHF radio receives the signal and a PC sound card samples the acoustic data at 48 kHz. In addition, a two-channel hydrophone – sampling at 192 kHz – was dropped into the water on a few occasions when the vessel was stationary long enough for a sufficient recording. This ancillary data was used only to familiarize the data analyst with Arctic acoustics by observing transient signals and the sources that generate them.

Hydrophone Calibration

Calibration of the HARP hydrophone in several configurations was conducted at the U.S. Navy's Transducer Evaluation Center (TRANSDEC) in San Diego, California on January 30 and April 30, 2007 (see Figure 2.6). TRANSDEC is a transducer calibration and underwater acoustic test facility; hydrophone calibration is ideal in this controlled environment due to low levels of ambient noise and convenient access. The large, man-made anechoic pool is 300 ft. by 200 ft. by 38 ft. deep, and contains 6 million gallons of chemically treated fresh water, continuously circulated to maintain isothermal conditions.

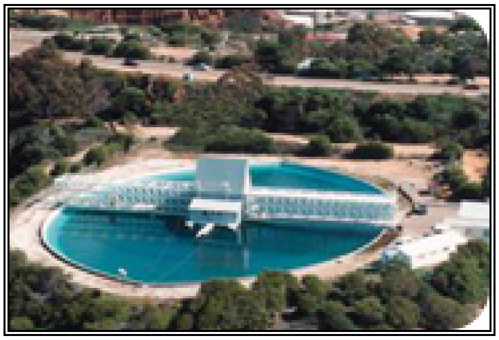

Figure 2.6 – An aerial view of the U.S. Navy's Transducer Calibration Center.

When making underwater sound measurements in a tank, one must consider constructive and destructive interference from standing waves in the sound field, since reflections off the sides, surface, and bottom of the tank are necessarily close to the projector (i.e. source) and hydrophone (i.e. receiver). The boundary at the surface is the most significant contributor since an air-water interface is a near perfect reflector (see Figure 2.7). This makes it difficult to generate and measure a progressive plane sound wave.

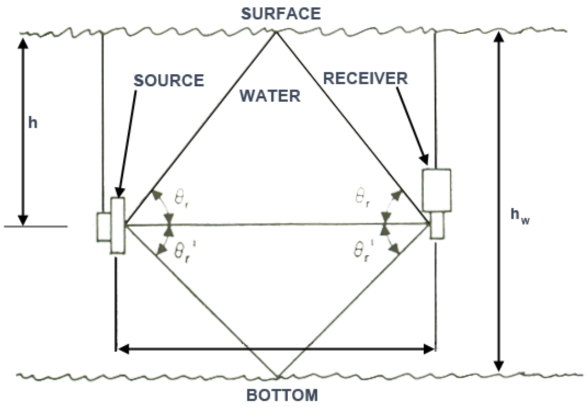

Figure 2.7 – Geometry of source and receiver in a calibration station showing the direct path of sound transmission as well as reflected paths from the surface and bottom. Reproduced from NDRC Technical Report, Vol. 10, Ch. 5.

If an omnidirectional receiver measures sound pressure at an arbitrary point in the near-field, the values may fluctuate about the measured pressure in the direct beam as frequency varies. If the tank environment is shown to have a negligible effect on measurements, then the sound-field intensity typically varies inversely with the square of the distance between the projector and hydrophone (Albers, 1965). According to Foldy (1945), the expression for sound pressure at a depth *h*, operating frequency *f*, sound speed *c*, and distance *d* between a point-source projector and omnidirectional hydrophone is

$$p = \left[p_0^2 + \frac{p_0^2 d^2}{d^2 + 4h^2} - \frac{2 p_0^2 d}{(d^2 + 4h^2)^{1/2}} \cos \frac{2\pi f}{c} \left(\sqrt{d^2 + 4h^2} \right) - d \right]^{1/2},$$

where p_0 is the pressure that would exist if the water surface was not present.

Several calibration runs were performed at a depth of six meters to measure the received sensitivity of each hydrophone in response to a source transducer transmitting different frequencies from a distance of 2 meters. The J15 (2.7 V_{rms}) transducer swept through 10-1200 Hz, and an ITC-1007 (0.4 V_{rms}) transducer swept through 1-30 kHz.

There was also an interest in determining the directivity pattern of the hydrophone based on the geometric arrangement of the transducer bundle. Consider that for an omnidirectional projector, the hydrophone could receive more signals as a result of reflected paths rather than direct path (Albers, 1965). Even at frequencies higher than 1 kHz, the hydrophone appeared to remain omni-directional while being rotated 180° relative to the source transducer (see Figure 2.8).

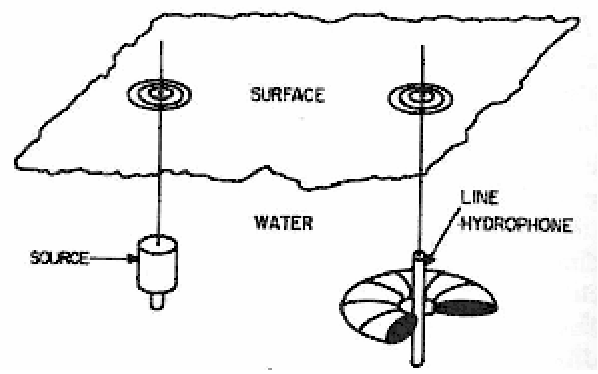

Figure 2.8 – Orienting a line hydrophone in a calibration station to minimize the effects of surface reflections. Reproduced from NDRC Technical Report, Vol. 10, Ch. 5.

TRANSDEC helps to verify the expected hydrophone response based on preamplifier measurements on the lab bench and theoretical sensitivity of the piezoelectric transducers (see Figure 2.9). The hydrophone from Site A was replaced during refurbishment in 2007 and brought back to San Diego, so the actual sensor used in the first year of study was calibrated prior to data analysis. Differences between the hydrophones at Sites A and B are expected to be less than 1 dB, due to slight variations in hydrophone sensitivity and circuitry. The calibration testing showed the expected response of the instrument to be within ±1-2 dB of the measured response.

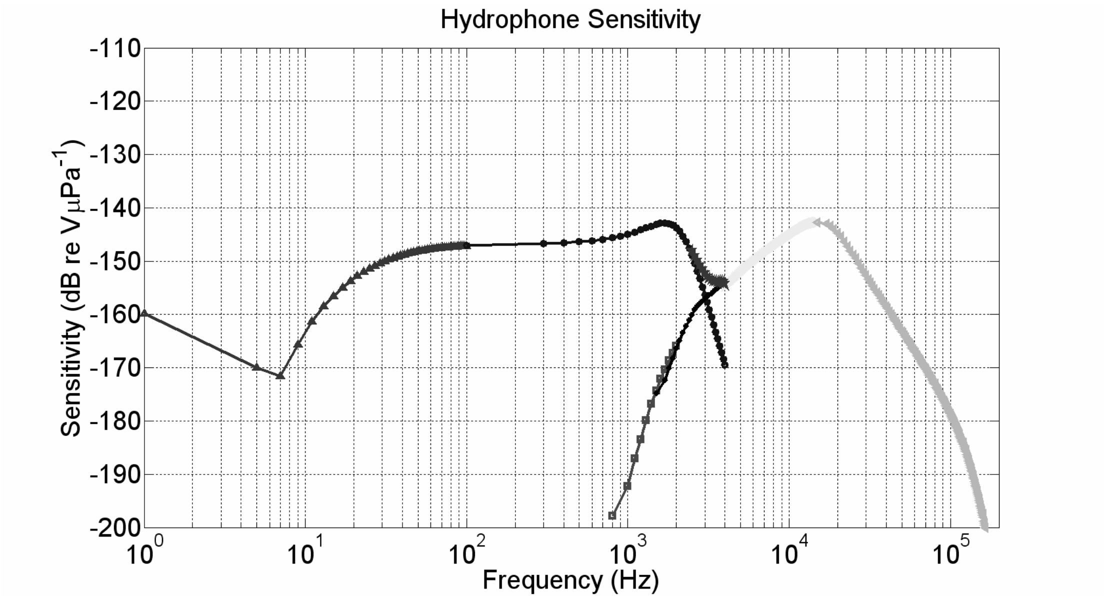

Figure 2.9 – The shape of the hydrophone sensitivity used in this study is determined by the transducer and pre-amplifier circuit. Stage one is the low-frequency band on the left, and stage two is the high-frequency band on the right.

The seafloor recorder is not expected to have a meaningful response below 10 Hz, while the high-frequency rolloff of the recorders used in the Arctic begin at 15 kHz, and provide 30 dB/octave of protection from aliasing. For the purposes of data analysis, a transfer function can be computed based on the sensitivity of the transducer elements in addition to the signal-conditioning provided by the pre-amplifier (see Figure 2.10). Once subtracted from the data, this allows for spectral measurements to be reported as absolute receive-pressure levels of ambient noise.

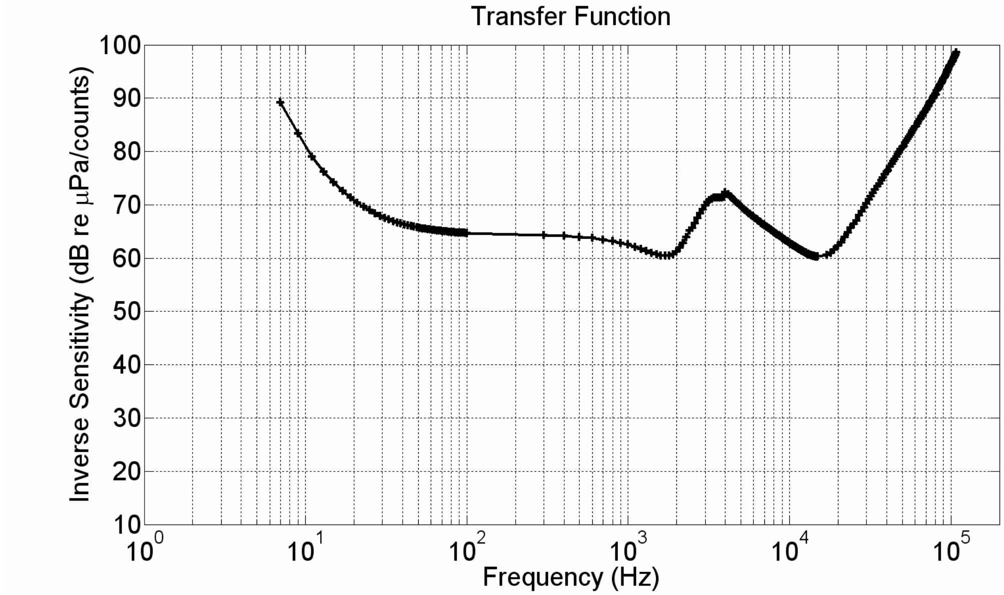

Figure 2.10 – The transfer function is applied to the data in order to correct for hydrophone sensitivity.

Digital Signal Processing with MatLab

Analyzing long-term, high-frequency acoustic data is challenging due to both the size and resolution of the time series. The "raw" binary data collected by the HARPs is processed into 1 GB files generated in a format called XWAV; this is similar to a WAV format but in addition contains header information such as experimental parameters and time stamps. The data can then be spectrally analyzed using the Signal Processing toolbox in MatLab.

Fourier analysis was performed on all data in the time-domain using the discrete Fourier transform (DFT) to produce frequency-domain representations of the acoustic signals. Discrete time requires that the input signal has non-zero values that are limited or finite in duration, which is achieved through uniform sampling of the continuous time signal. Conversion from continuous time to discrete-time samples changes the underlying Fourier transform of *x(t)* into a discrete-time Fourier transform, and generally includes aliasing distortion. If the Nyquist (i.e. cutoff) frequency is known to be 16 kHz, then the appropriate sample-rate is at least twice that value, or 32 kHz, in order to minimize aliasing effects. Similarly, transforming a very long sequence can result in spectral leakage, which leads to a reduction in DFT resolution; specifying an appropriate sub-sequence length, or NFFT length, is important in minimizing such effects. A standard technique is to perform multiple DFTs and create time-evolving spectrograms. To compute a power spectrum for data containing noise or random processes, averaging the magnitude components of multiple DFTs reduces the variance inherent in the spectrum.

Computationally, direct application of the DFT to a data vector of length n requires n multiplications and n additions — a total of $2n^2$ floating-point operations. Fast Fourier Transform (FFT) algorithms have computational complexity O(n log n) instead of O(n^2). For example, if n is a power of 2, a one-dimensional FFT of length n requires less than $3n \log_2 n$ floating-point operations. For $n = 220$, that is a factor of almost 35,000 faster than $2n^2$ (www.mathworks.com). The FFT is an efficient algorithm to compute DFTs, and is defined by the formula

$$X_k = \sum_{n=0}^{N-1} x_n e^{-\frac{2\pi i}{N} nk}, \quad k = 0, \ldots, N-1,$$

where $e^{\frac{2\pi i}{N}}$ is a primitive N^{th} root of unity. The complex numbers X_k represent the amplitude and phase of the different sinusoidal components of the input signal x_n. Euler's formula helps to express sinusoids in terms of complex exponentials, which are much easier to manipulate.

Welch's method (1967), commonly referred to as the periodogram method, estimates power spectral densities (PSD) by dividing the time signal into successive blocks, and averaging squared-magnitude DFTs of the signal blocks. Let $x_n(k) = x(k + nM)$, for $k = 0, 1, \ldots, M - 1$, denote the n^{th} block of the signal $x \in C^{NM}$,with N denoting the number of blocks. The Welch PSD estimate is given by

$$\hat{R}_x(\omega_k) = \frac{1}{N}\sum_{n=0}^{N-1} \left|DFT_k(x_n)\right|^2 \cong \left\{ \left|X_n(\omega_k)^2\right| \right\}_n$$

where the RHS denotes time averaging across blocks of data indexed by *n*. The function ‘pwelch’ implements Welch's method in MatLab’s Signal Processing Toolbox. Since $\left|X_n(\omega_k)\right|^2 = N \cdot DFT_k(\hat{R}_{x_n})$, and since the DFT is a linear operator, averaging magnitude-squared DFTs $\left|X_n(\omega_k)\right|^2$ is equivalent to estimating block autocorrelations $\hat{R}_{x_n}$, averaging them, and taking a DFT of the average. However, this process is slower than Welch’s method.

The ‘pwelch’ function uses the Goertzel algorithm to calculate the power spectral density by dividing the input signal vector *x* into *k* segments with no overlap. A Hanning window is applied to each segment of *x*, and a 32000-point FFT is then applied to the windowed data to obtain 1 Hz bins. The modified periodogram of each windowed segment is computed and the set of modified periodograms is averaged to form the spectrum estimate $S(e^{j\omega})$. The resulting spectrum estimate is scaled to compute the power spectral density as $S(e^{j\omega}) / F_s$, where the sampling frequency F_s = 32000 Hz. The number of segments *k* that *x* is divided into is calculated as $k = m / l$, where m is the length of the signal vector x, and l is the windowed length of each segment.

Welch’s method returns a power spectral density estimate yielding units of *power per frequency*. The units are crucial since a density can be integrated to obtain an estimate of the average power over a given frequency interval. Moreover, Welch’s method returns a single sided spectrum for real signals since the total power of the signal is contained in half the spectrum (i.e. 0-16 kHz). In other words, integrating a single-sided PSD estimate yields the average power estimate over the entire Nyquist interval. The same result occurs if integrating a double-sided PSD estimate over the entire sampling interval (i.e. 0-32 kHz).

Spectral Averaging

Preliminary assessment of the data was performed using Triton, GUI software code developed in MatLab by Wiggins (2003). Long-term spectral averages (LTSAs) - a scheme used for file compression and data overview (Wiggins, 2007) - were computed for successive spectra by averaging 32 Hz bins over 120 sec bins throughout the entire data set. The LTSA provides a time series of averaged-spectra arranged sequentially, as shown in Figure 2.11. This allows the analyst to efficiently search for and manually detect transient signals or unknown acoustic events such as marine mammal vocalizations, sea ice mechanics, and man-made noise. Triton has built-in functionality enabling the analyst to “zoom in” on an event in the LTSA and view its spectrogram - computed directly from the XWAV file - with finer-scale resolution in both the frequency and time axis.

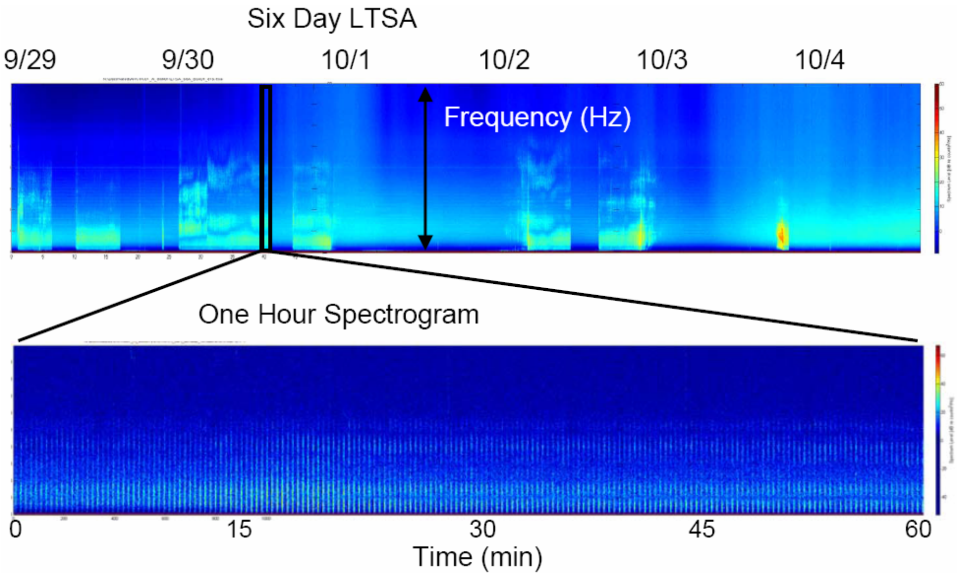

Figure 2.11 – Long-term spectral averages show when acoustic events occur in the time series.

Calibrated ambient noise measurements were produced using two different averaging schemes that pursued different analysis objectives. In both cases, 200 sec samples of continuous data were used with no overlap between each spectral average. All spectra were processed with a Hanning window and 32000-point FFT, yielding 1 Hz bins that provide high-resolution sound spectrums. The first method computed monthly averages using select 200 sec samples on a near-daily basis, where no acoustic events were observed. Of course these samples may potentially include hard-to-detect broadband sound sources like wind or surface waves coupling with the underwater environment. This is acceptable since the objective here is to quantify the background noise of the underwater environment in this specific region, and provide a conservative baseline estimate for comparison to other spectral analyses performed throughout this study.

The second method computed monthly averages using continuous 200 sec samples sequentially through the entire data set, including all transient signals and acoustic events. Each monthly spectrum was computed continuously with 200 sec spectrally-averaged samples, so there were approximately 17,000 spectra samples for each month. From the statistical density distribution of these samples, ambient noise curves were generated based on measured sound-pressure levels for the highest 1%, upper 10%, median 50%, lower 10%, and lowest 1% of the distribution samples. The mean curve was also computed in order to illustrate the deviation of ambient noise level distributions from a Gaussian or Poison probability distribution.

It is important to note that all spectral averaging was performed on a logarithmic scale rather than a linear scale. Mathematically this does not make sense, but statistically it is logarithmic quantities that are invariably dealt with in ocean propagation. This is because multipath propagation and scattering strength dominate transmission fluctuations in the ocean and lead to broad statistical distributions (Dyer, 1970). It is especially the case for the Arctic Ocean, where impulsive events dominate a sound spectrum that has ambient noise levels reported to be as much as 25 dB below those observed for sea state zero in open ocean for the 10 - 1000 Hz frequency band (Kibblewhite and Jones, 1976). Therefore the mean and standard deviation for any logarithmic measure, such as acoustic transmission loss over long distances from multiple sources, differ considerably from corresponding mean-square measures (see Figure 2.12) (Dyer, 1970).

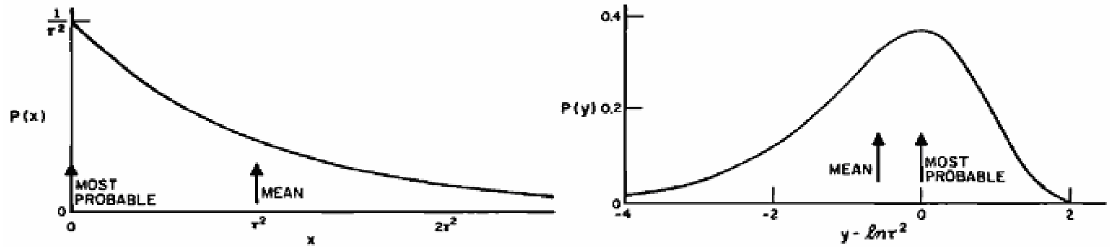

Figure 2.12 – Probability density function of the mean square (left) and logarithm (right).

Log probability density *P(y)* is obtained by the transformation $y = \ln x$, where x is the normalized mean-square ratio of received pressure over reference pressure, and is

$$\begin{aligned} P(y) &= (1/2\sigma_1^2)\exp(y - \exp y/2\sigma_1^2), \qquad -\infty < y \le \ln \tau_o^2, \\ \mu_y &= \ln 2\sigma_1^2 - \gamma = \ln \tau^2 - \gamma, \\ \sigma_y^2 &= \pi^2/6, \end{aligned}$$

where τ is mean transmission in a path, $\tau_0^2 = \tau^2 N$ and N is the number of independent paths, γ is Euler's constant (= 0.577…), μ is the mean, and σ is the standard deviation. The equation results in a broad and skew density, where the mean transmission loss is

$$\mu_H = -10\log\tau^2 + 2.5dB\,,$$

and the standard deviation of transmission loss is

$$\mu_H = 4.34\pi 6^{-1/2} = 5.6dB\,,$$

which is a constant independent of any metrics. Figure 2.13 illustrates the substantial difference between the mean and standard deviation when l = 1 tone and the densities are quite broad. For certain months in the Arctic data, probability densities were very broad, and logarithmic distributions were found to resemble chi-square distributions, not log-normal distributions as would be expected for open ocean measurements.

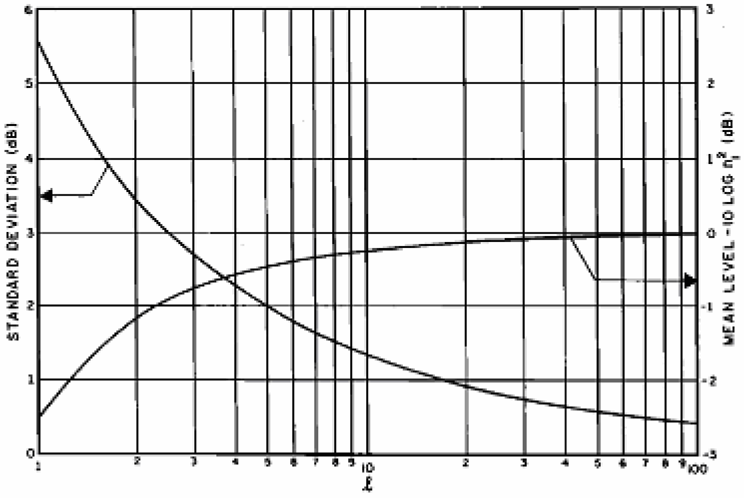

Figure 2.13 – Mean and standard deviation of noise level modeled by l tones, with n_l^2 the received noise power.

Electronic & System Noise

When making calibrated ambient noise measurements, one must be certain that the signals analyzed contain only recordings of the ocean environment and are not corrupted by other noise processes injected into the time series. Throughout the analysis, several issues relating to electronic and system noise from the HARP were encountered in the digitized data. It was crucial to identify these processes and implement digital signal processing techniques to subtract them from the original time series before conducting spectral analysis.

The first noise process discovered in the data logging system was generated by the First-In First-Out (FIFO) storage buffer in the A/D converter, used at the input for data flow control between digital conversion computations. Every 4000 samples (12.5 msec), analog signals are pushed off the FIFO, generating 16 impulsive electronic clicks. The periodicity of this repetition and period between clicks produced noise spikes in the sound spectrum with a fundamental frequency of 3.8 kHz and subsequent harmonics at 7.6 kHz, etc. To resolve this issue, several minutes of the time series were segmented into 4000-sample blocks, stacked on top of each other, and averaged together; the result was a clear, isolated reproduction of the FIFO noise (see Figure 2.14). A matched filter was then generated by creating an artificial time series with the FIFO noise repeated every 4000 samples. By subtracting the matched filter time series from the original data time series, the FIFO noise process disappeared completely before performing any spectral analysis.

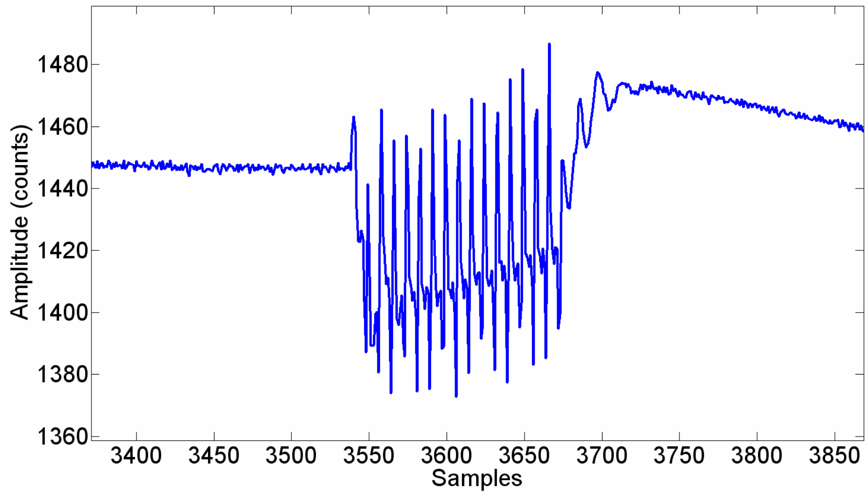

Figure 2.14 – Digital synthesis of the FIFO noise – sixteen amplitude-spikes occurring every 4000 samples in the data.

The source of the second noise process is still unknown and appears to have fluctuated in amplitude over time. Furthermore, unlike the uniform periodicity of the FIFO noise, this noise process evolved over time. Thus the matched filtering technique cannot effectively subtract the noise from the data time series. While further analysis is needed to generate the proper filter, for the purposes of this study, the noise was dealt with in the frequency domain in order to produce “clean” spectra. Noise spikes occurred at the fundamental frequency of 100 Hz and subsequent harmonics every 100

Hz across the entire frequency band. The data in these 1 Hz bins was removed and linear interpolation was performed between the bins before and after the noise spikes. This effectively subtracted the unknown noise process and smoothed the spectral plots.

A third noise process originating in the datalogger is known to be hard disks spinning up and writing for approximately one minute during every eight-minute sampling cycle (see Figure 2.15). Again, further analysis is necessary to generate the proper filter, but since a majority of the noise occurred within the band that is not being reported, it was decided that the noise would remain in the time series. Note that harmonics can be seen in the high-frequency band spectra, and should be regarded as electronic system noise.

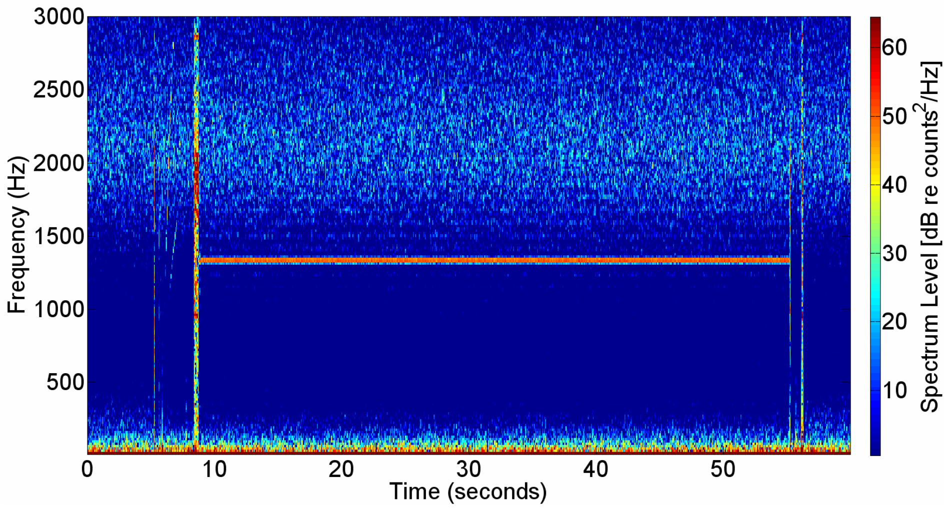

Figure 2.15 – Spectrogram of hard drive noise during spin-up and disk write, occurring approximately every 8 minutes in the data.

Since the hydrophone sensor is so broadband and sensitive, it can prove difficult at times to maintain a high signal-to-noise ratio across the entire frequency band. The summation of all noise sources - especially thermal noise - within a system is referred to as the noise floor. For any pressure measurement, the noise floor is dependent on the spectral shape being recorded and is time dependent due to normal voltage fluctuations within the electronics. The noise floor of the instrument for low frequencies is calculated to be near the lowest values observed in this study. At higher frequencies above 3 kHz however, the noise floor appears to be slightly above the lowest values observed (see Figure 2.16). The noise floor effectively limits the smallest measurement that can be taken with certainty since any measured amplitude can be no less than the noise floor level. This infers that at high frequencies when there is full ice coverage and low wind speed, the lowest acoustic pressure levels are not measured, and therefore cannot be reported here.

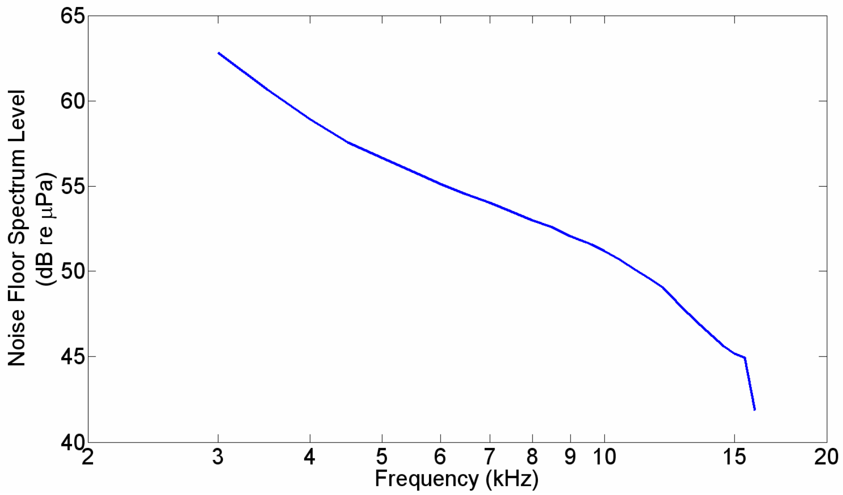

Figure 2.16 – The noise floor curve was empirically determined for the high-frequency band from flat values in the spectral time series, where it was apparent that the amplitude of ocean ambient noise fell below the electronic thermal noise of the hydrophone sensor.

AMSR-E Sea Ice Concentration Data

The Advanced Microwave Scanning Radiometer - Earth Observing System (AMSR-E) is one of six sensors aboard NASA's Aqua satellite. AMSR-E is passive microwave radiometer that observes atmospheric, land, oceanic, and cryospheric parameters, including precipitation, sea surface temperatures, ice concentrations, snow water equivalent, surface wetness, wind speed, atmospheric cloud water, and water vapor. From a near-polar low-Earth orbit, sea ice concentration can be determined indirectly by measuring the backscatter of microwave radiation (i.e. brightness temperature) reflected from the Earth's surface, taking advantage of the marked contrast in microwave emissions between sea ice and liquid water. The AMSR-E sensor records at twelve channels and six frequencies ranging from 6.9 to 89 GHz at both horizontal and vertical polarization.

Recent advances in sea ice concentration remote sensing now offer spatial resolutions of approximately 6 by 4 km at 89 GHz on a polar stereographic projection, nearly three times the resolution of the standard sensor SSM/I at 85 GHz (15 by 13 km). The Arctic Radiation and Turbulence Interaction Study conducted near Svalbard in 1998 led to development of the ARTIST Sea Ice (ASI) algorithm, which is made available to the public by the University of Bremen. The ASI algorithm enables estimation of sea ice concentration from the channels near 90 GHz, despite enhanced atmospheric influence in these channels. Full exploitation of their horizontal resolution is four times finer than that of the channels near 19 and 37 GHz; these frequencies are used by the most widespread algorithms for sea ice retrieval, the NASA-Team 2 and NSIDC Bootstrap algorithms. The ASI algorithm combines a model derived from SSM/I 85-GHz data with an ocean mask derived from the 18-, 23-, and 37-GHz AMSR-E data using weather filters (Spreen et al, 2008).

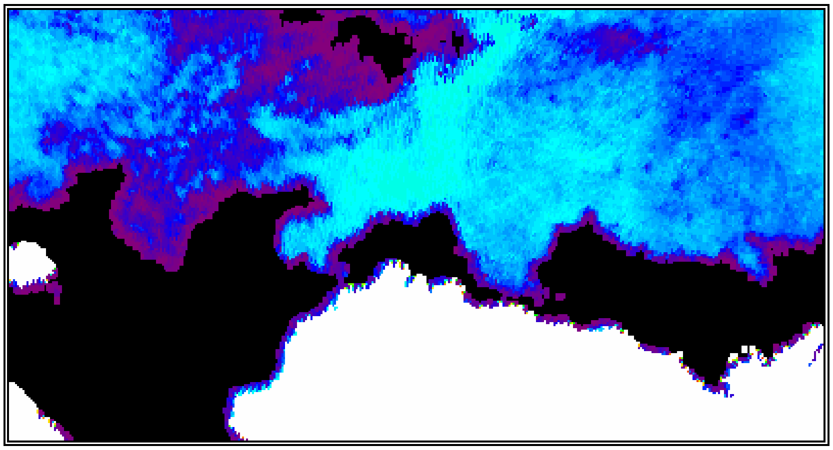

Figure 2.17 – An example of a daily-average of AMSR-E sea ice concentration data, viewed at a 4x4 km linear-pixel projection in WIM.

Derived data products are stored in Hierarchical Data Format (HDF) using the multi-file Scientific Data Set model, and depict gridded sea ice concentration as a floating point value. Daily mean values from July 2006 to July 2007 were extracted for an area between 68° to 76° N latitude and 180° to 130° W longitude. Time-series analysis was performed using Windows Image Manager (WIM) and WIM Automation Module (WAM) software developed by Kahru (2000) (see Figure 2.17). It was convenient to remap the 6.26 km pixels in polar stereographic projection to a 4 km pixel linear projection. Four different mask areas centered around each instrument site were determined (see Figure 2.18) – a circle with a 10, 40, and 100 nautical mile radius, and an ellipse with a 400 nautical mile horizontal radius. WAM computes the arithmetic mean, variance, and median for each day based on the extent of sea ice coverage as a percentage of the total mask area. On certain days there is no valid data in the mask area due to a periodic spatial gap in the polar-orbit satellite passes; linear interpolation was applied so that a data point exists for every day in the mean sea ice concentration time series.

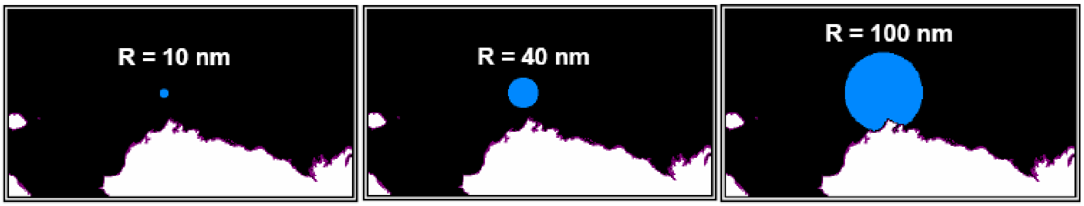

Figure 2.18 – Mask areas used to perform time series analysis on AMSR-E sea ice concentration data. Three circles were centered over the HARP sites, shown from left to right with radii of 10, 40, and 100 nautical miles.

Discrete or continuous random time series have several statistical properties that help characterize the variability of the series and allow for comparison between one another. The correlation function describes the covariability of given time series as functions of two different times, *t* and *t* + τ, where τ is the lag time. It uses the "raw" data series before removal of the mean, as opposed to the covariance function. If *y(t)* is a stochastic time series consisting of *N* values, the autocorrelation function R_{yy} is expressed as

$$R_{yy}(\tau) = \frac{1}{N-k}\sum_{i=1}^{N-k}(y_i y_{i+k}) ,$$

where $\tau = \tau_k = k\Delta t$ for $k = 0,\ldots,M$ is the lag time for *k* sampling time increments, Δt, and $M = N$. In general, the autocorrelation function will be more strongly correlated than the original time series *y(t)*. Replacing one of the *y(t)* with another function *x(t)*, the cross-correlation function R_{xy} between two time series is expressed as

$$R_{xy}(\tau) = \frac{1}{N-k}\sum_{i=1}^{N-k}(y_i x_{i+k}) .$$

Daily or weekly samples are not necessarily independent, so in order to determine the number of independent sea ice coverage and acoustic pressure level samples at each site, the integral time scale must be computed from autocorrelations of the sea ice concentration and acoustic pressure level data. The integral time scale *T* is defined as the sum of the normalized autocorrelation function ρ_{yy} over the length $L = N\Delta\tau$ of the time series for *N* lag steps, $\Delta\tau$. The estimate is expressed as

$$T = \frac{\Delta\tau}{2}\sum_{i=0}^{N'}\left[\rho_{yy}(\tau_i) + \rho_{yy}(\tau_{i+1})\right],$$

where $N' \leq N - 1$ provides a measure of the dominant correlation time scale within the time series – for times longer than *T*, the data become decorrelated. In general, the summation should continue until it reaches a near-constant value, which is taken as the value for *T*. The number of instrument deployment days is divided by the calculated integral time scale to determine degrees of freedom (i.e. bin size) within the time series, or the number of independent samples at each site (Emery and Thomson, 1998).

Sea ice concentration data had a longer integral time scale for independence of estimates at both sites than did acoustic pressure levels, ranging from two to three days depending on the size of the mask area. Pearson's coefficient of correlation was binned into two-day periods corresponding to the integral time scale. A *t*-test evaluated the null hypothesis that sea ice concentration and acoustic pressure levels are not related, using significance level $\alpha = 0.05$.

Barrow Wind Speed Data

Wind data was obtained from the U.S. National Weather Service at the NOAA Alaska Region Headquarters. Meteorological variables were measured at location 71°

17’07” N, 156° 45’57” W, by an Automated Surface Observing System (10 meters above sea level) at Wiley Post-Will Rogers Memorial Airport in Barrow, AK, which is approximately 60 nautical miles south of the instrument sites. This separation between recording sites may result in minor error. Daily-value time series ranging from July 2006 to July 2007 were collected for weather elements including peak wind speed (knots), average wind speed (knots), and peak wind direction.

Statistical time series analysis could not be performed on daily-averaged wind speed since only one data point exists for each day, but there was still interest nonetheless to determine if cross-correlations exist between wind speed and acoustic pressure levels at different frequency bands. The comparison was binned into two-day intervals so that the role of sea ice influencing the correlation between wind and ambient noise could also be examined with the same number of independent samples.

Sound Speed Profiles

The most significant environmental factor influencing acoustic measurements in the open ocean include refraction effects caused by thermal gradients. Albers (1965) emphasized that bathythermograph measurements should be included with all acoustic measurements made in the ocean so that corrections for refraction can be applied to the measurements.

While underway on the Healy in September 2007, vertical sound speed profile measurements were conducted at both instrument sites and several other locations in the Chukchi Sea (see Figure 2.19). These profiles cannot be representative of sound speed at other times throughout the year since water temperatures can fluctuate substantially in response to changes in sea ice coverage and solar radiation (i.e. ice albedo). The thermocline is probably shallower and subtle in winter, while deeper and more pronounced in summer. As with any scientific measurement in the Arctic Ocean though, it's always more difficult to collect vertical profile data during the winter season.

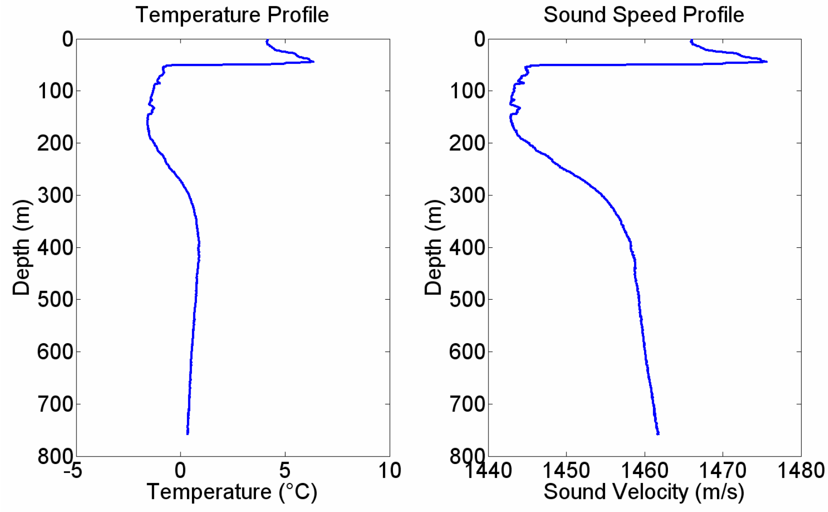

Figure 2.19 – Vertical depth profiles for water temperature (left) and sound speed (right) were measured by XBT probes during the summer of 2007.

Measurements were collected using expendable AN/SSQ-36B bathythermograph sonobuoys, a low-cost method for obtaining vertical temperature profiles. The 16-pound (7.3 kg) units are easily deployed from the deck of a surface vessel and provide a thermal gradient measurement scheme. Thirty seconds after water entry at the surface, a probe activates and descends at a rate of 1.5 m/sec (5 ft/sec). The buoy has an operating life of approximately 12 minutes, which allows the probe to reach depths between 0 and 800 meters (2625 ft). Thermistors located in the probe measure changes in seawater temperature during descent with a calibrated sensor accuracy of ±0.55° C (±1° F). VHF transmissions at 0.25 W are received via RF transmittal to a radio station aboard the surface vessel. The data can be processed and displayed as temperature versus depth using the following relationships:

temperature (°F), $T = \frac{f - 800}{20}$ and depth (m), $z = (1.5m/s)*t$,

where f is sound frequency transmitted and t is the length of time during transmission. The speed of sound in seawater depends on pressure (i.e. depth) and temperature (Δ1° C ~ 4 m/s) to first order, and salinity (Δ1‰ ~ 1 m/s) to second order. An empirical equation derived by Mackenzie (1981) accurately calculates sound speed from these variables (higher order terms using salinity measurements are neglected), given as

$$\begin{aligned} c(T,z) = 1448.96 + (4.591)T - (5.304\times10^{-2})T^2 + (2.374\times10^{-4})T^3 \\ + (1.63\times10^{-2})z + (1.675\times10^{-7})z^2 - (7.139\times10^{-13})Tz^3 \end{aligned}.$$

III. RESULTS

Ambient Noise Measurements

Due to an inductor – onboard the hydrophone's pre-amplifier circuit – failing during deployment from freezing temperatures, ocean ambient noise was not recorded in the frequency band between 250-3000 Hz. Instead only self-noise was recorded in the circuit tank, so therefore data will not be reported at these frequencies. Spectral plots are instead presented for a low-frequency band (10-250 Hz) and high-frequency band (3-16 kHz). It was also unanticiaped that alkaline batteries would be pushed beyond their operating conditions, but since there was consistent water temperatures of -2° C, the voltages eventually drained below the sufficient amount needed to draw current to the hard drives. Therefore, the site A instrument was only able to record data for five months while the site B instrument recorded for nine months.

Background-noise levels are shown in Figures 3.1 and 3.2 for site A from September, 2006 – January, 2007 and site B from September, 2006 – May, 2007. All acoustic events, transient signals, and electronic noise were removed from the spectral averages, in addition to applying a transfer function to correct for received pressure levels. In summer and early fall, broadband sources like storm-generated winds and surface waves couple with the underwater noise environment, but from late fall to late spring, it is the state of sea ice that inevitably influences the complex relationship between ambient noise and the environment. At 10 Hz, the site A spectra converge around 85-88 dB re µPa while site B is spread out between 80 and 93 dB re µPa.

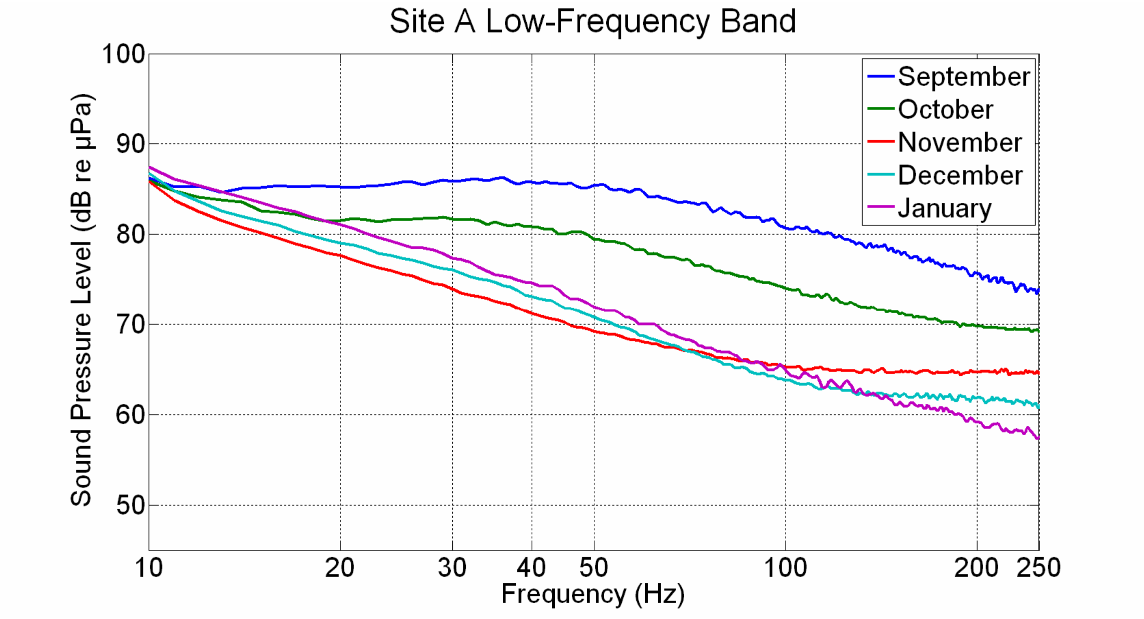

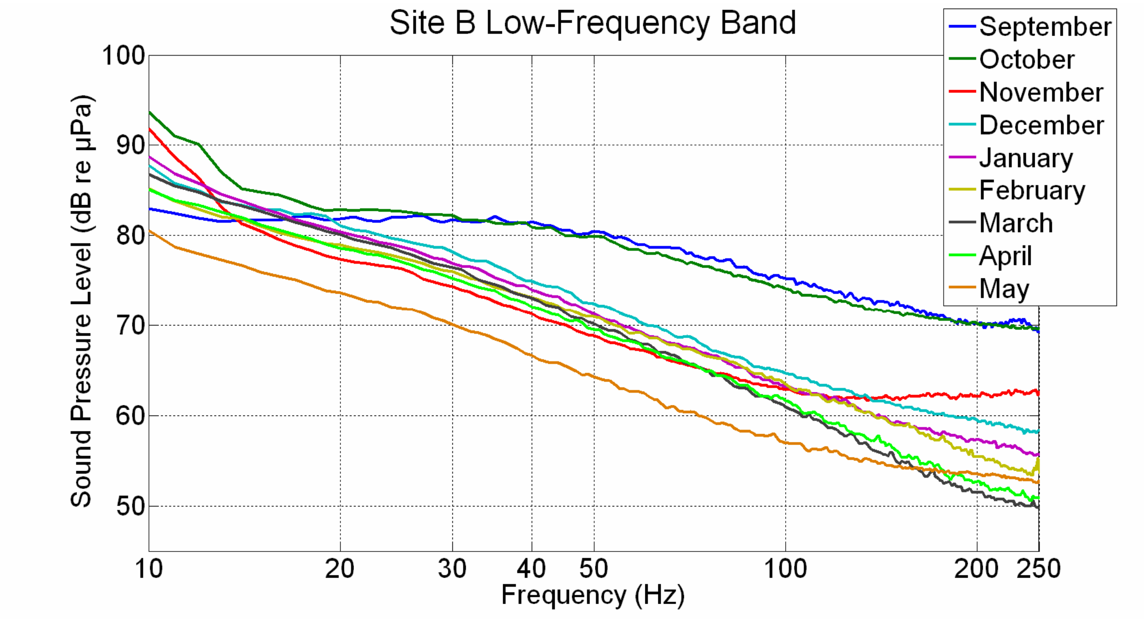

Figure 3.1 – Low-frequency background levels for sites A (Sep. 06 – Jan. 07) and B (Sep. 06 – May 07) during the duration of HARP deployment and successful data recording.

Across the entire low-frequency band, September and October are naturally the noisiest months – due to open-sea conditions – reaching peak noise-levels of 87 dB re µPa between 20 and 60 Hz at site A (see Figure 3.1). All other months that were recorded exhibit low spectrum levels, as sound-pressure levels decrease linearly approximately 8 dB/octave as frequency increases logarithmically. Typical levels for both sites at 50 Hz are shown to be slightly above or below 70 dB re µPa, with May reaching as low as 65 dB re µPa. By 200 Hz, noise levels at site B are as low as almost 50 dB re µPa in March, the month where sea ice extent reaches its maximum. The steep spectral slopes of ambient noise are most likely attributed to sea ice coverage in the region around the two instruments.

Heavy pack and shore-fast ice act like a rigid boundary for sounds propagating horizontally across the waveguide, except that the underside of sea ice is rough and dispersed with ridges and keels. As frequency increases so does scattering strength and thus transmission loss; plane waves that reflect off ice tend to attenuate rapidly and transmit over shorter distances. Figure 3.2 demonstrates that there is little variability between different months in the high-frequency band. Besides September, nearly every month at Site B converges and noise-spectrum levels are characterized as 63 dB re µPa at 3 kHz, 52 dB re µPa at 10 kHz, and drops off even further to as low as 45 dB re µPa at 15 kHz. At site A, there is a consistent spacing interval between sound-pressure level curves across the frequency band, which decrease in order from September through January.

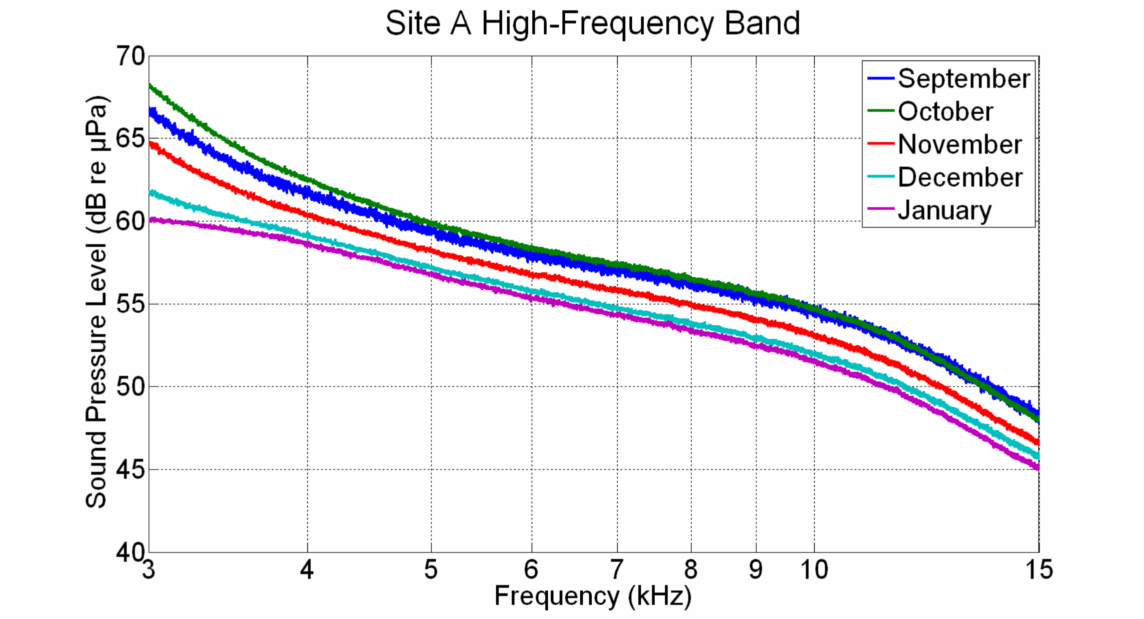

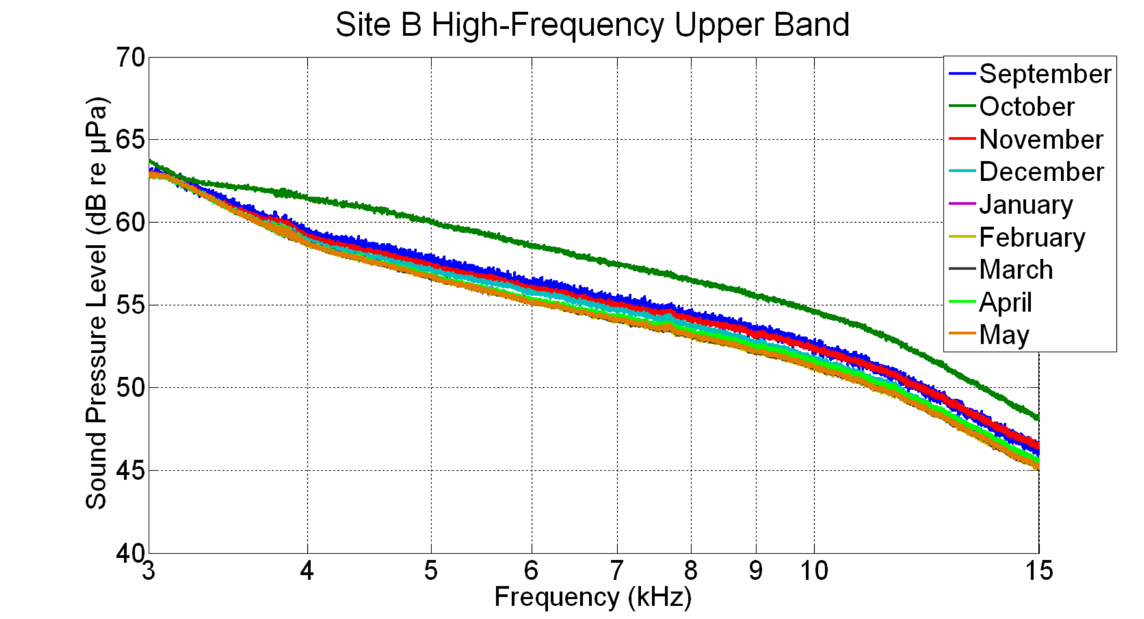

Figure 3.2 – High-frequency background levels for sites A (Sep. 06 – Jan. 07) and B (Sep. 06 – May 07) during the duration of HARP deployment and successful data recording.

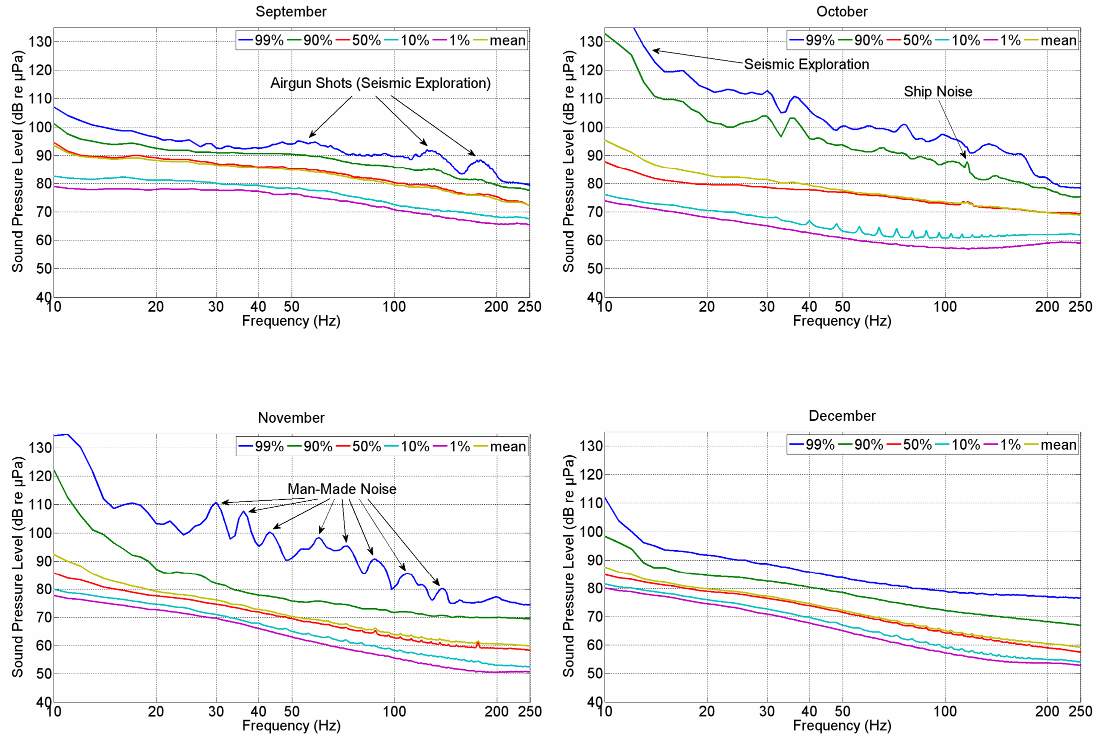

Figure 3.3 – Site B Low-Frequency Noise Distributions.

Seismic airguns are present from Sep. to Nov., while 10% of Oct. is exposed to noise above 130dB re µPa at 10Hz and 112dB re µPa between 20–30Hz. The harmonics present in Nov., Feb., and May are indicative of hydrophone strum noise. Background levels decrease approximately 8dB/octave, reaching 70dB re µPa at 10Hz and under 50dB re µPa between 150–250Hz.

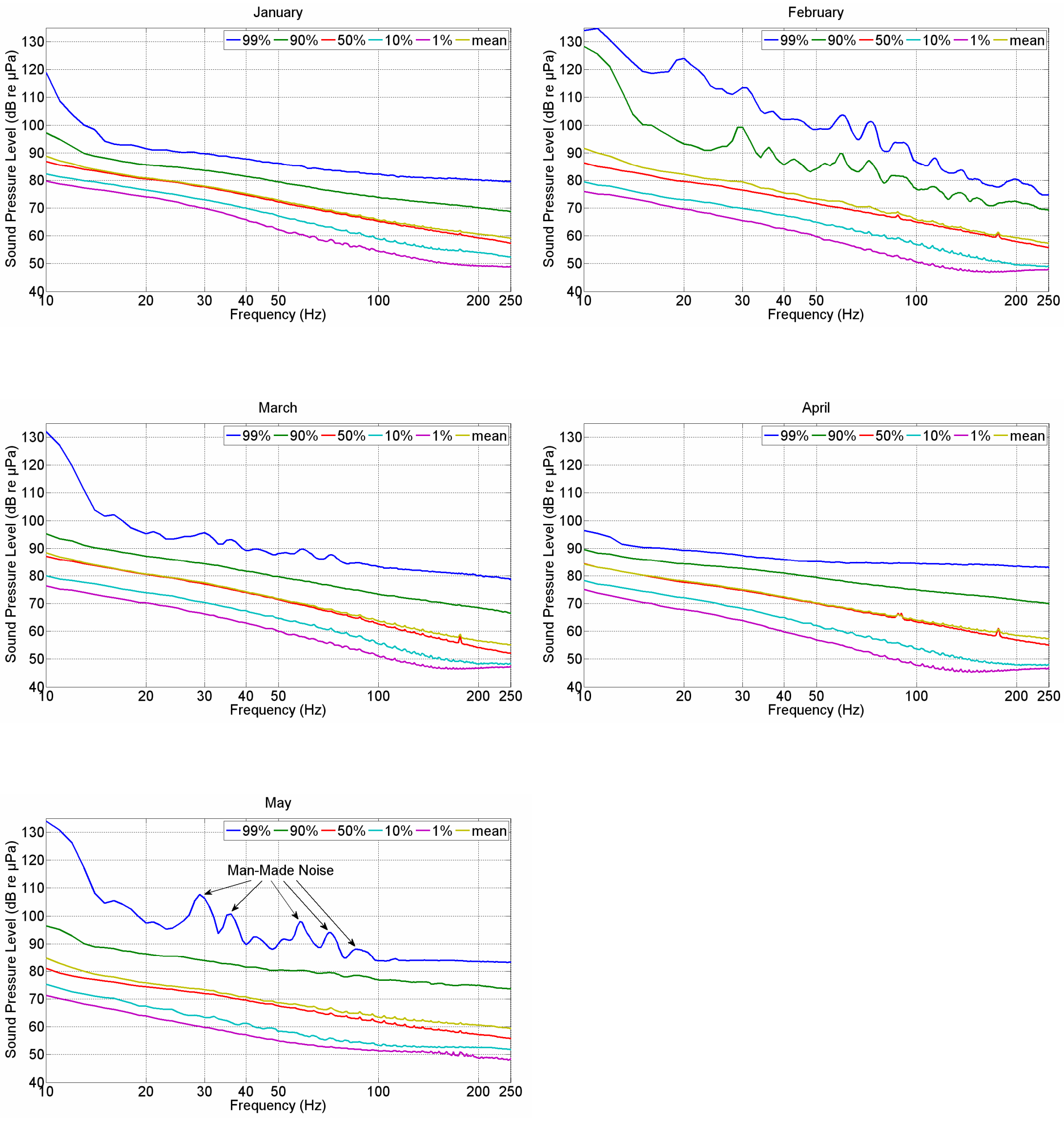

Figure 3.3 – Continued

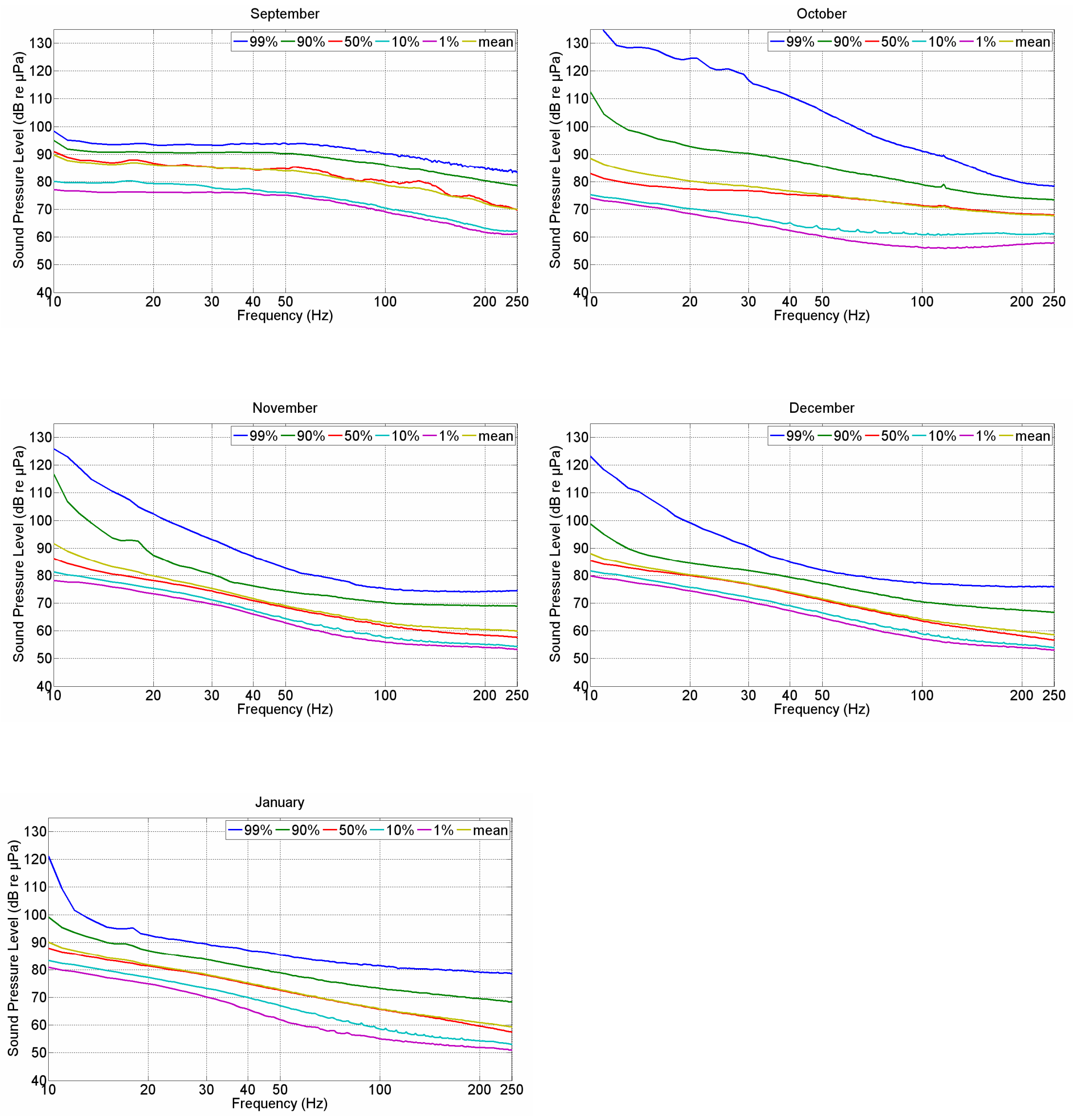

Figure 3.4 – Site A Low-Frequency Noise Distributions.
Much less transient energy was received compared to site B, possibly due to differences in bathymetry. Sep. and Jan. are good examples of a near-Gaussian distribution across the frequency band since the spectral curves are spaced apart evenly from the mean measurement. Most months for both sites exhibit non-Gaussian behavior due to a low background environment interposed by impulsive transient events such as dynamic sea ice mechanisms and man-made noise.

Figures 3.3, 3.4, 3.5, and 3.6 represent statistical pressure-density distributions for every month, each containing approximately 17,000 spectral-averaged, 200 sec samples. Sound-pressure spectrum levels are shown for distribution percentiles for the highest 1% (99%), upper 10% (90%), median (50%), lower 10%, lowest 1%, and mean distribution. Deviation of the mean from the median illustrates the assymetry of the density peak from Gaussian normal, while the upper and lower percentiles describe the shape of the tails. Because of the unique properties inherent in Arctic transmission loss, oceanic ambient background-noise is typically very low and characterized by a steeply decreasing slope as frequency increases. The composite of impulsive transient-sound events noticeably stands out above the ambient noise spectrum. Certain months have spectral-energy peaks at varying frequencies, which can be attributed to different acoustic sources such as the dynamic processes of sea ice, intermittent anthropogenic noise, and possibly marine mammal vocalizations at stereotypic calling bands. These transient signals will be discussed in the analysis section.

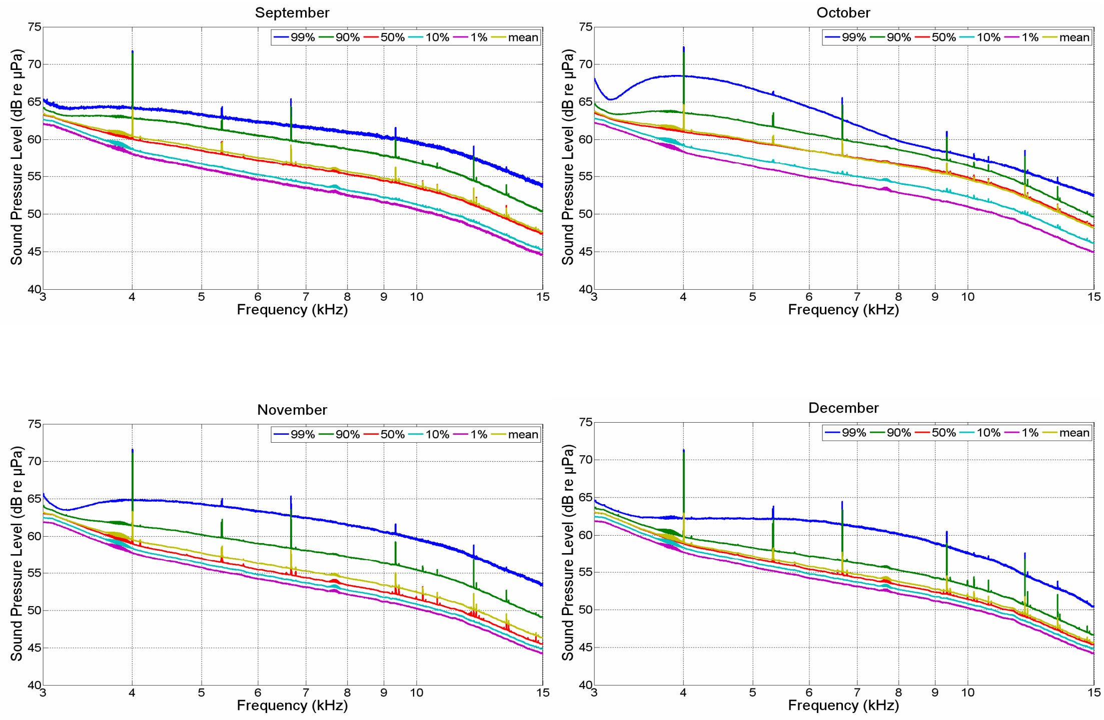

September

October

November

December

Figure 3.5 – Site B High-Frequency Noise Distributions.

Comparing noise levels to the similar background levels in Figure 3.2 show that transient signals do not really influence high-frequency ambient noise since attenuation is so high. At 3 kHz, noise levels range between 60–65dB re µPa, converge to around 50dB re µPa at 10 kHz, and decrease to less than 45dB re µPa at 15 kHz. Note that the frequency spikes are attributed to electronic instrument noise and should not be considered.

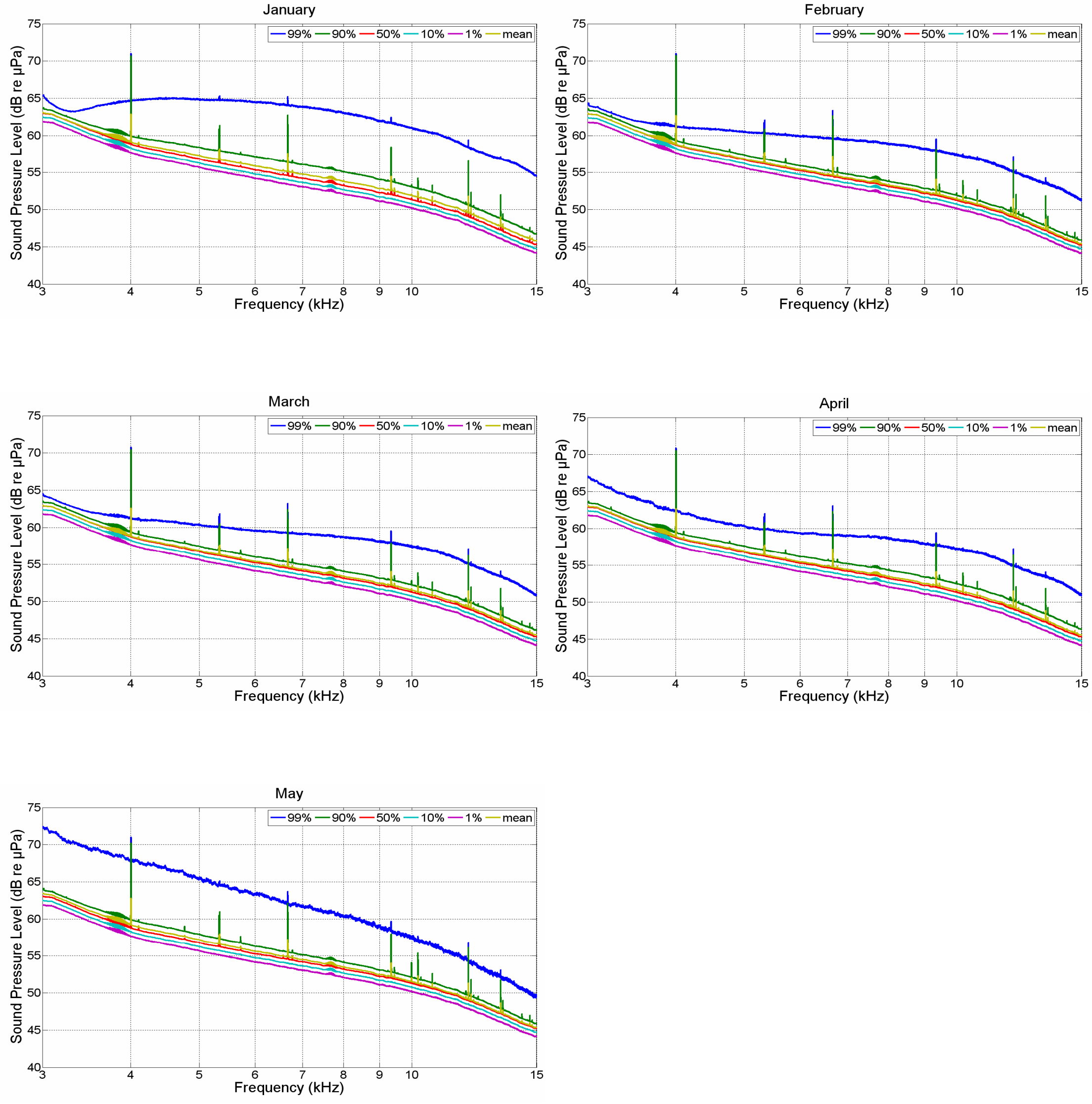

Figure 3.5 – Continued

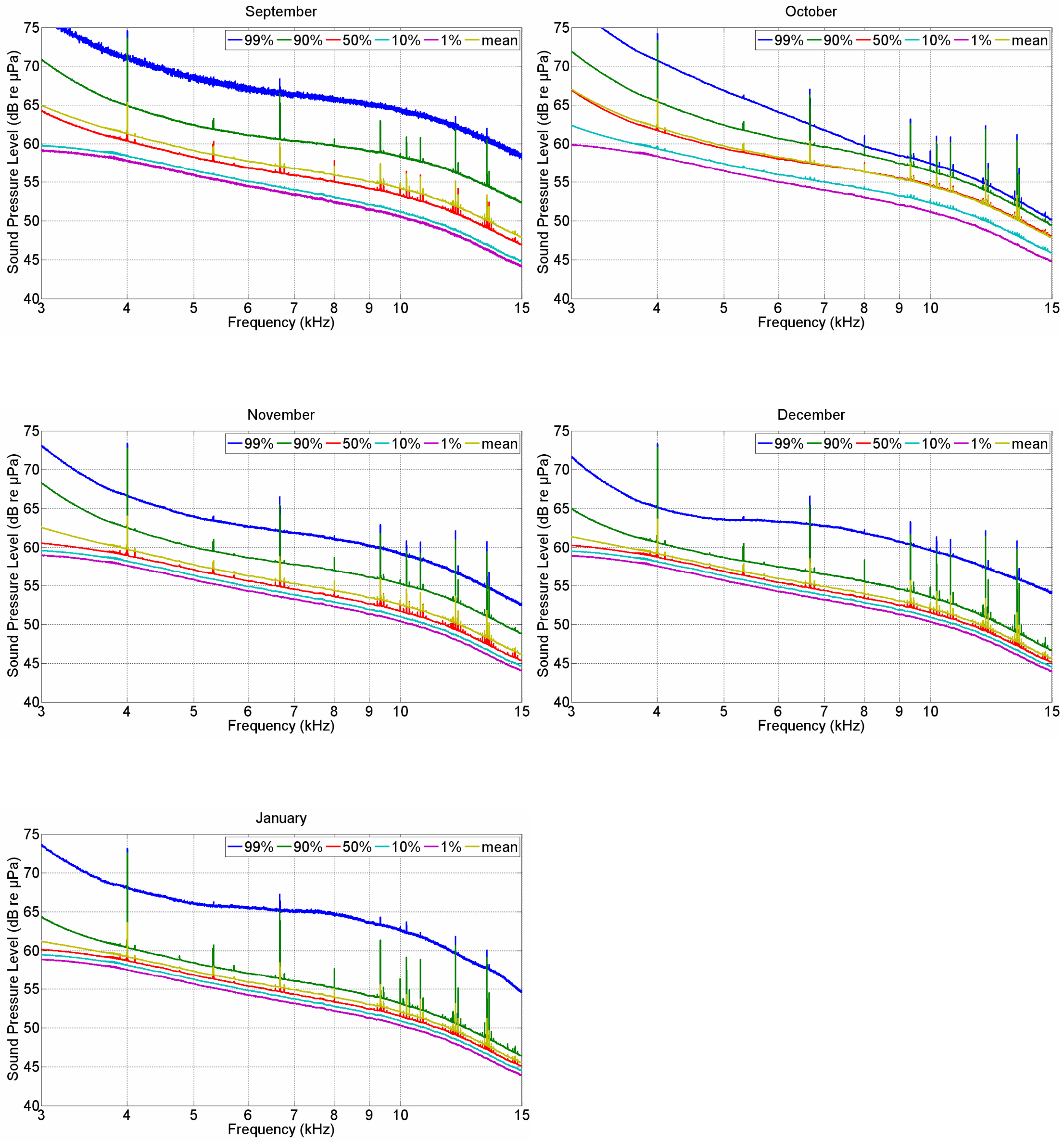
September

October

November

December

January

Figure 3.6 – Site A High-Frequency Noise Distributions.

For every month, the 99th percentile is measured well above mean and median spectrum levels, and is indicative of highly-impulsive and localized noise sources being received through direct ray path transmission by the hydrophone. In September, impulsive noise is derived from wind-driven wave interactions with the MIZ, while in January thermal fracturing is responsible for this non-Gaussian distribution.

Environmental Correlates

The three plots in Figure 3.7 show time series for acoustic pressure-levels simaltaneously with average wind speed and sea ice concentration data. The spatial areas used for time series analysis of sea ice coverage were chosen based upon the potential propagation range appropriate for three different frequency bands – 25 Hz over 100 nautical miles, 100 Hz over 40 nautical miles, and 5 kHz over 10 nautical miles.

During summer and fall when sea ice has retreated north and open-ocean conditions prevail (September through November), the peaks and troughs of sound-pressure spectrum levels correlate directly with those of high wind speed values, especially in early October; typically strong winds are indicative of storms or other low-pressure weather patterns. Throughout winter and spring, large-scale thermal fracturing opens up leads and causes sea ice coverage to sporadically decline for short periods, as a result of atmospheric circulation and wind-stress forcing. For cases such as in early February, the spectral energy-peaks of sound correlate very well with high wind speeds, but still depend foremost on sea ice conditions. During sea ice pack formation and subsequent pressure ridging in the fall, high-frequency noise levels around 5 kHz respond substantially to these localized noise-generating mechanisms. In fact, spectral-energy peaks in this frequency band seem to correlate best with wind speed, and occur across greater temporal variability. When sea ice maintains 100% coverage in the surrounding area and wind speed values are low, no correlations exist and ambient noise has reached its lowest sound-pressure levels.

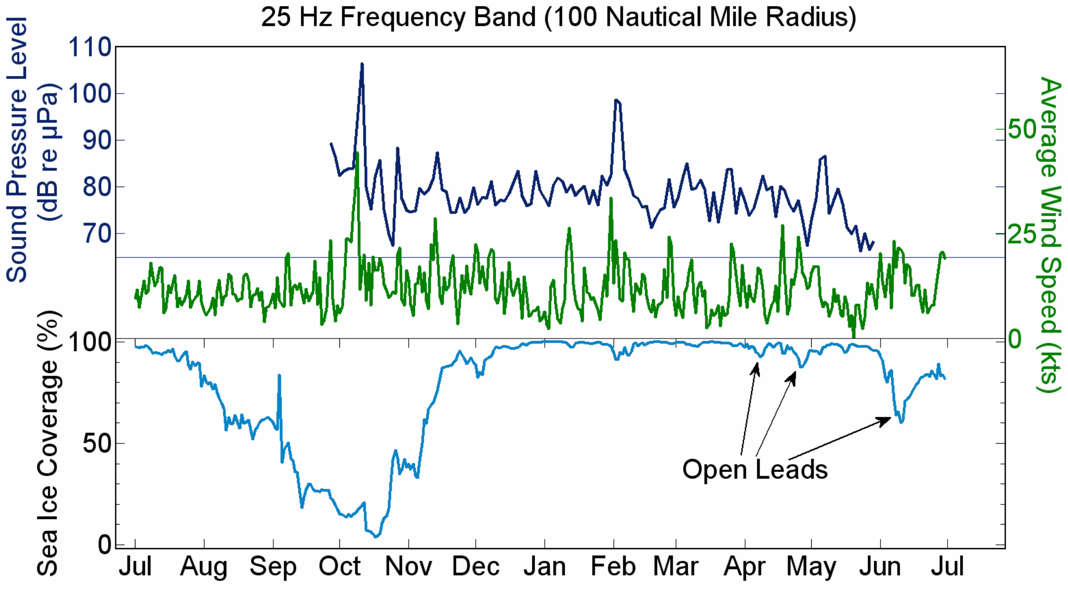

Figure 3.7 – Time series of sound-pressure spectrum levels (top/dark blue) for three different frequencies (25, 100, 5000 Hz) plotted with daily-average wind speed values (middle/green) over Barrow, as well as the percentage of sea ice coverage (bottom/light blue) for a specified area (10, 40, 100 nautical mile radius) centered around the instrument sites. Note that for the 5 kHz band, flat noise levels at 57 dB re µPa in the spectral time series indicate the noise floor of the HARP was reached, so in actuality it can be assumed that ambient noise levels at this frequency extend several dB below what is reported here.

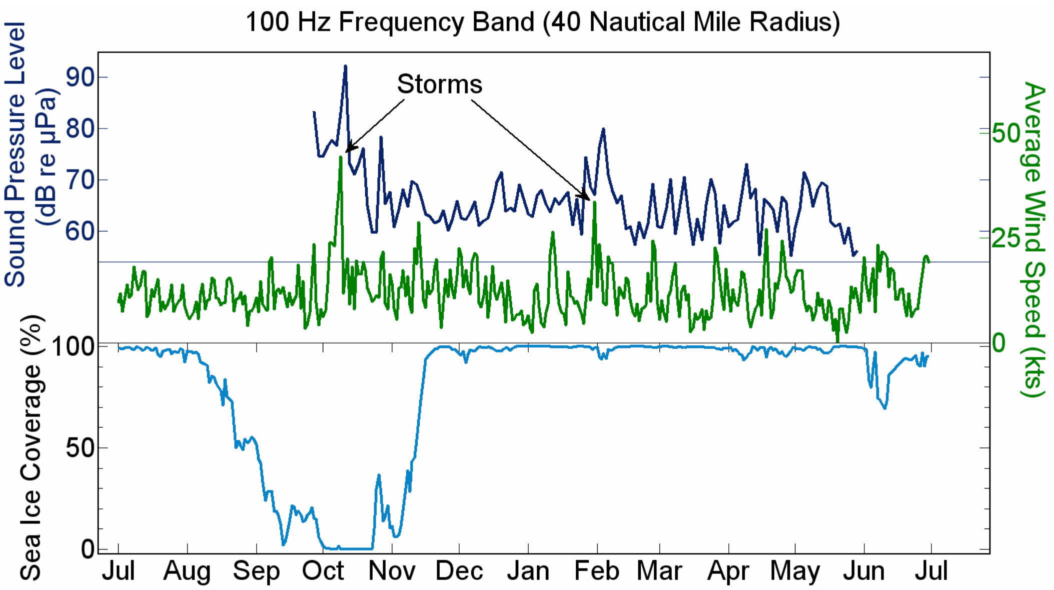
100 Hz Frequency Band (40 Nautical Mile Radius)

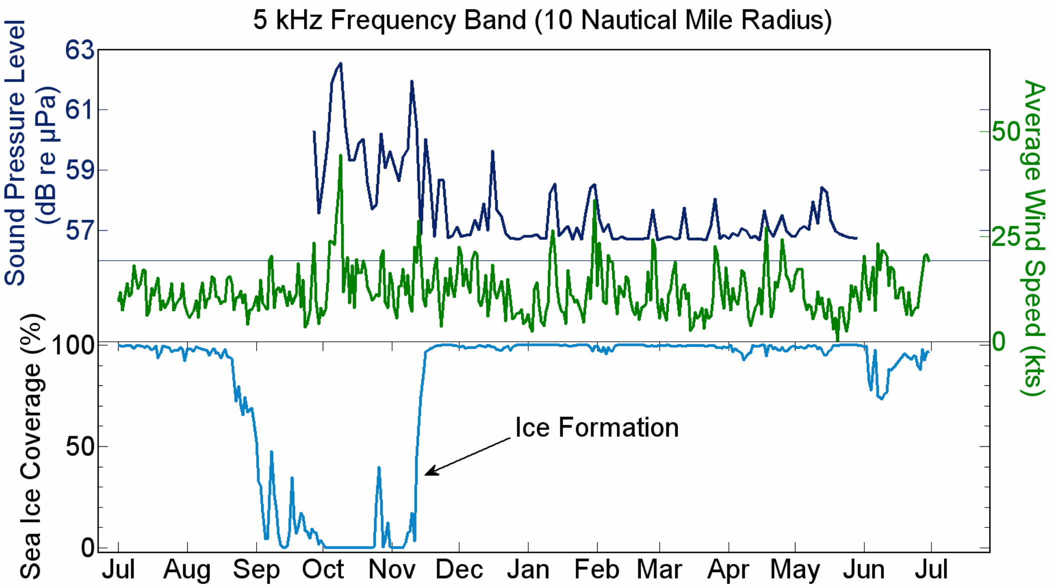
5 kHz Frequency Band (10 Nautical Mile Radius)

Figure 3.7 – Continued

IV. ANALYSIS

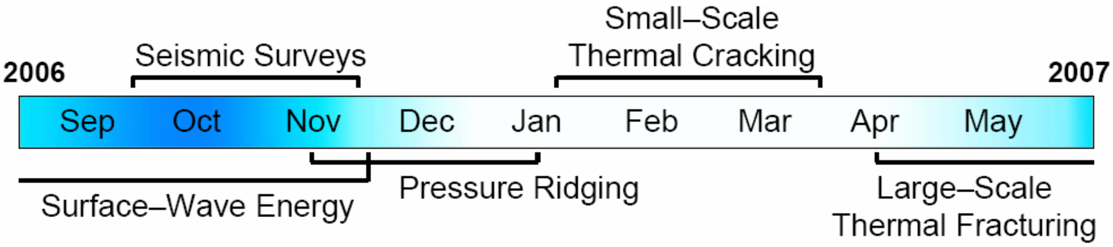

Figure 4.1 – Time scales of noise-generating mechanisms

Man-Made Seismic & Low-Frequency Noise

Airguns are used for seismic marine reflection and refraction surveys, which are currently taking place each summer across vast Arctic coastal regions for oil and natural gas exploration. The device consists of pneumatic chambers pressurized with air. An array of multiple airguns is submerged below the sea surface and towed behind a ship; when the air gun is fired, a bolt is retracted, allowing compressed air to escape the chamber and release a burst pulse of instantaneous high-acoustic energy.

According to modal theory, if the seismic source is near the sea surface, then only sound waves with quarter wavelengths longer than the water depth will penetrate the earth. This is of course frequency dependent, so if a vessel is conducting a seismic survey on the continental shelf of Alaska's North Slope – where the average depth is between 50 and 100 m – then theoretically around 7 or 8 Hz acoustic waves will reflect off the seafloor and propagate over great distances through the waveguide. Since it is completely open water (i.e. nearly perfect reflector) during summer in a shallow waveguide, the effects of Arctic transmission loss no longer apply, and the residual energy of airgun shots become trapped in the water column during transmission. Because of modal dispersion, the signal arrives at the hydrophone spread over time, since propagation velocity is not the same for all modes (see Figure 4.2). Throughout this section, note the color bar to the right of each spectrogram represents the spectrum level in dB re counts^2/Hz.

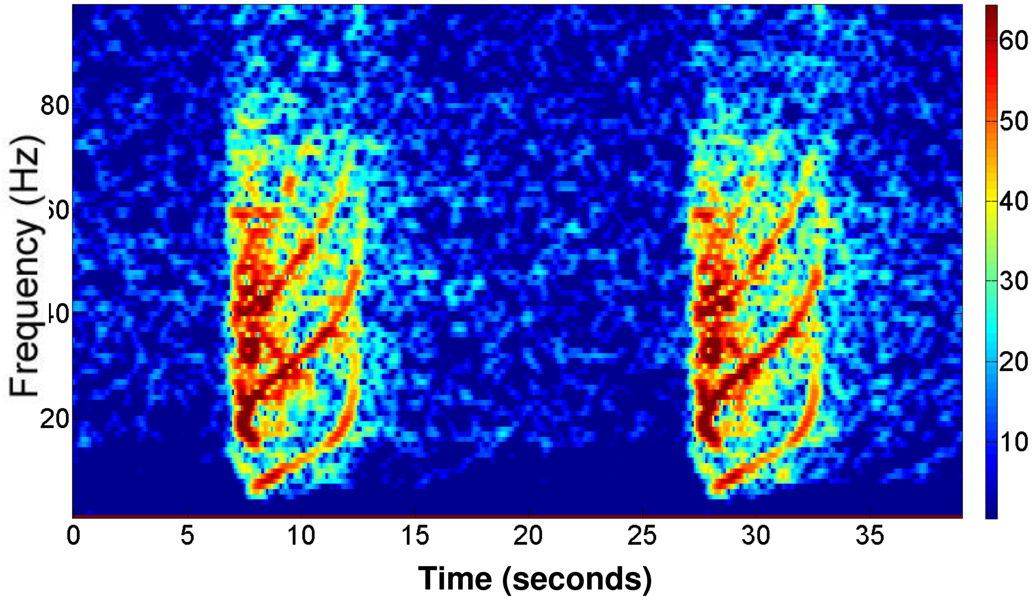

Figure 4.2 – Modal dispersion of airgun shots from a seismic oil exploration survey, as received by the HARP hydrophone on the seafloor.

Seismic surveys were carried out in the Chukchi Sea on a regular basis between September and November of 2006. For several hours at a time, airgun shots were produced at 10-20 second intervals, and the quality of signal that was received depended upon the distance between the source vessel and hydrophone receiver. On the shallow shelf of the Chukchi Sea, this anthropogenic noise is capable of long-range transmission without experiencing significant spectral energy losses.

Figure 4.3 illustrates another type of man-made noise that was found periodically throughout the data. Noise tonals and associated harmonics range from

10-150 Hz, produced from rotating or reciprocating machinery generated by ships radiating sound underwater, or by snowmobile engines coupling through the ice.

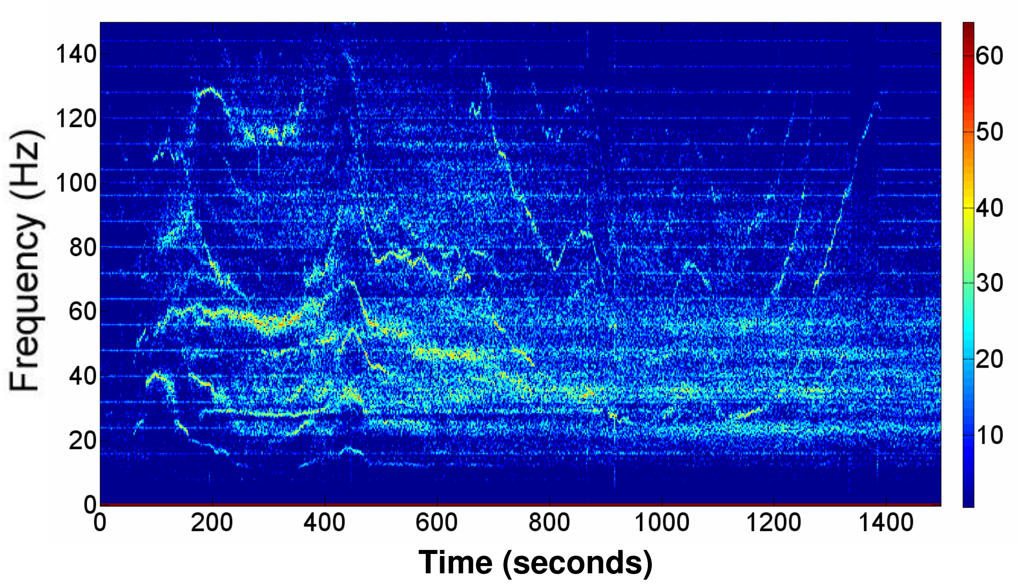

Figure 4.3 – Tonals like these have the acoustic signature of recipricating machinery.

Microseisms & Earthquakes

Low seafloor noise levels above 5 Hz provide a band for detection of small-magnitude local and regional earthquakes, which may have energy at frequencies extending up to 50 Hz (Webb, 1992). Webb proposed that most energy in the microseism band propagates from a wide source region in the Gulf of Alaska. Large earthquakes generate wave trains that occasionally dominate the sound-pressure spectrum across low frequencies, peaking at about a 25 second period (Webb, 1992).

Short-period microseism noise – usually related to storms at sea – falls significantly during periods of very light winds. Arctic seafloor measurements in the teleseismic frequency band (10^{-3} – 10^{1} Hz) during winter show that the generation of microseisms is suppressed due to near-continuous ice coverage preventing the excitation of ocean waves; Arctic seafloor sound-pressure levels in the microseism band provide possibly some of the quitest seismic sites on Earth (Webb, 1992). As a result, teleseismic noise levels on the Arctic basin are 20 dB less than those typical of the Atlantic Ocean and 40 dB less than those typical of the Pacific (Webb and Schultz, 1992). Figure 38 shows that the spectra of pressure fluctuations measured from the seafloor of the Beaufort Sea are unenergetic in comparison to measurements from the Pacific or Atlantic (Webb, 1992). At 10 Hz, noise levels in the Arctic are approximately 87 dB re 1 μPa^2/Hz, which match well with the measurements shown in Figure 4.4.

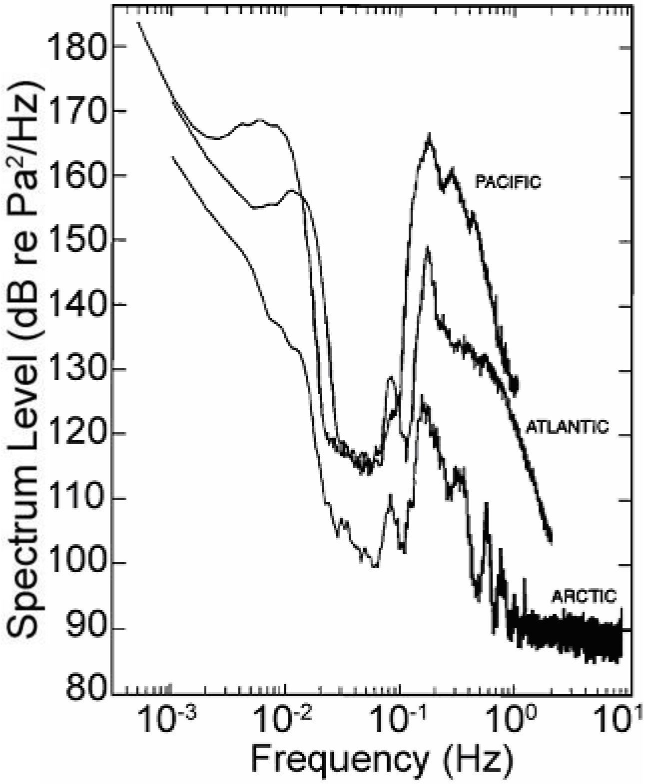

Figure 4.4 – Pressure spectra from the Pacific, Atlantic, and Arctic seafloors. The microseism peak is evident between 0.1 and 5 Hz. At 10 Hz, noise levels in the Arctic are approximately 87 dB re 1 μPa^2/Hz (Webb, 1992).

Transient Sea Ice Events

Makris and Dyer found that sea ice concentration correlates parametrically with ambient noise, implying that an increase in the density of potential acoustic sources is related to increases in the extent and concentration of the ice field. While noise-generating mechanisms such as ice-coupled tensile stresses and moments correlate well with low-frequency ambient noise in the ice canopy, they are poor correlates in the MIZ. The best environmental correlate of ambient noise in the MIZ is related to ice floe drift speed and the resultant interactions, which exhibit a semidiurnal periodicity corresponding with wind-driven inertial oscillations in the ice field. These oscillating bands of convergence and divergence zones result in high-energy noise (see Figure 4.5) related to increases in sea ice concentration and pressure ridging (Makris and Dyer, 1991).

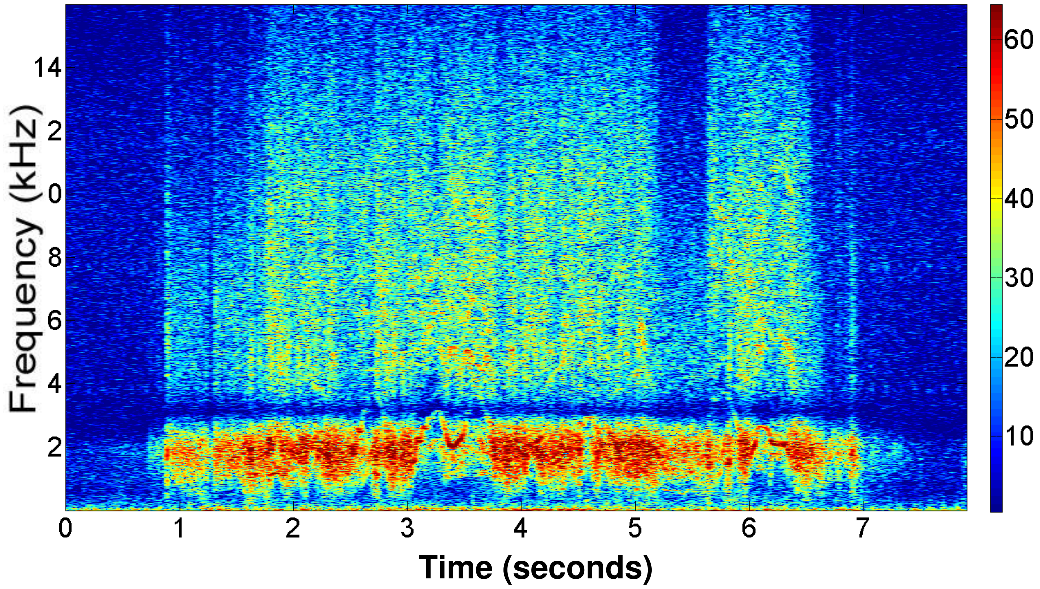

Figure 4.5 – Pressure ridging caused by interactions between adjacent ice floes.

The production of high-frequency noise increases almost immediately following decreases in air temperature and cloud cover conditions – typically associated with lower wind speeds – thus altering the radiation heat balance. However, thermal fracturing can be greatest when sensible heat flux – during periods of atmospheric warming – helps to warm sea ice prior to the onset of heat loss and rapid cooling (Lewis and Denner, 1988). The profusion of small-scale cracks originates from the hummocks and angular projections of pack ice, while longer cracks come from the uniform surfaces of frozen leads (Milne and Ganton, 1964). High spatial variability of such noise is likely the result of uneven snow cover due to wind forcing.

In winter, Gaussian "white" noise can be generated by the wind-induced motion of drifting granular snow being blown over rough sea ice, but this process is often masked during periods of decreasing air temperatures by high-energy impulsive events that reach spectral energy-peaks up to 40 dB above the Gaussian background. If air temperatures rise though, impulsive thermal ice fracturing noise tends to disappear (Milne and Ganton, 1964). The effects of thermal stress are found to be less prevalent in spring and summer than in winter, where thermally induced noise is prominent in the 2-15 kHz frequency band (see Figure 4.6); another correlate above 1 kHz is attributed to wind (Milne and Ganton, 1964).

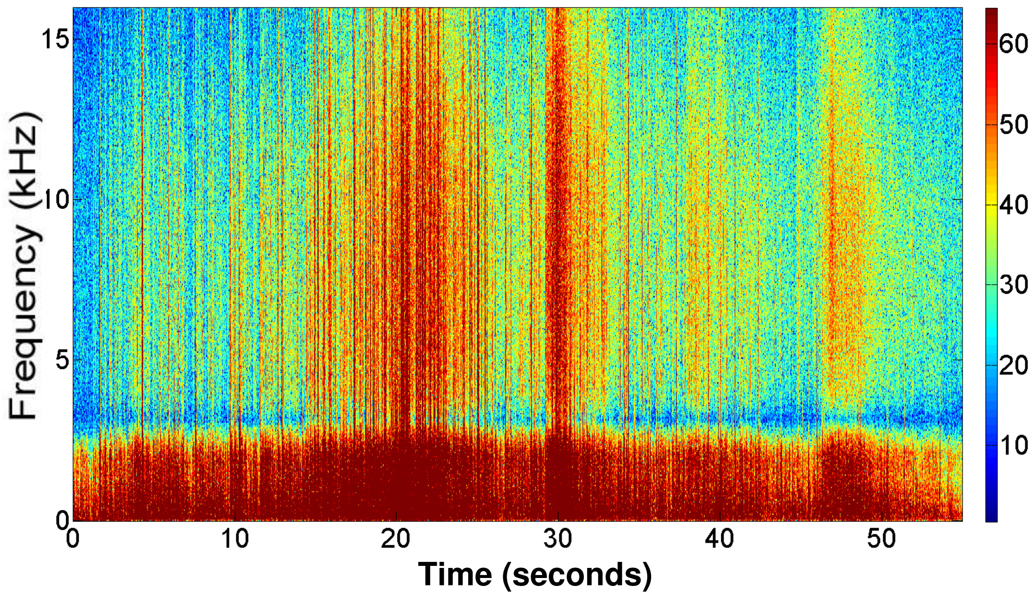

Figure 4.6 – Thermal fracturing due to atmospheric cooling.

Wind-Driven Noise

During fall, the ice pack receives a fresh blanketing of snow from advancing weather fronts. It is actually Arctic winds that then tend to strip snow from flatter regions while deposits of snow build up around the ridges and hummocks of pack ice; thus snow thickness exhibits a large variance in its spatial distribution. Lewis and Denner proved through their model of Arctic sound transmission that snow cover can consistently alter the degree in which sea ice responds to atmospherically induced thermal fracturing. Their heat-flux balance at the surface included short-wave solar radiation, long-wave atmospheric radiation, and long-wave ice radiation (i.e. albedo). Without snow cover, temperatures at the ice surface would drop due to reductions in cloud coverage or air temperature. Sensible heat flux from the atmosphere caused pack ice to warm whenever strong wind fronts approached. (Lewis and Denner, 1988)

The moments due to opposing wind and current stresses acting on sea ice correlate well with low-frequency noise generated from pack ice (Makris and Dyer, 1986). Ganton and Milne estimated – based on surface roughness and free-stream wind velocity – that for a Reynolds number greater than 125, the onset of wind at speeds ranging from 3-5 mph will penetrate the laminar sublayer of snow cover and prompt vortices to shed, thus producing noise coupled through the ice beneath (see Figure 4.7). Average wind speeds in the Arctic resemble a "white" Gaussian-noise distribution, and are attributed to be the major source of noise centered at 10 kHz (Ganton and Milne, 1965). Although wind-driven noise is much more pronounced under noncontinuous ice cover, according to Macpherson, ambient noise levels become independent of wind speed during periods of continuous pack ice coverage (Kibblewhite and Jones, 1976).

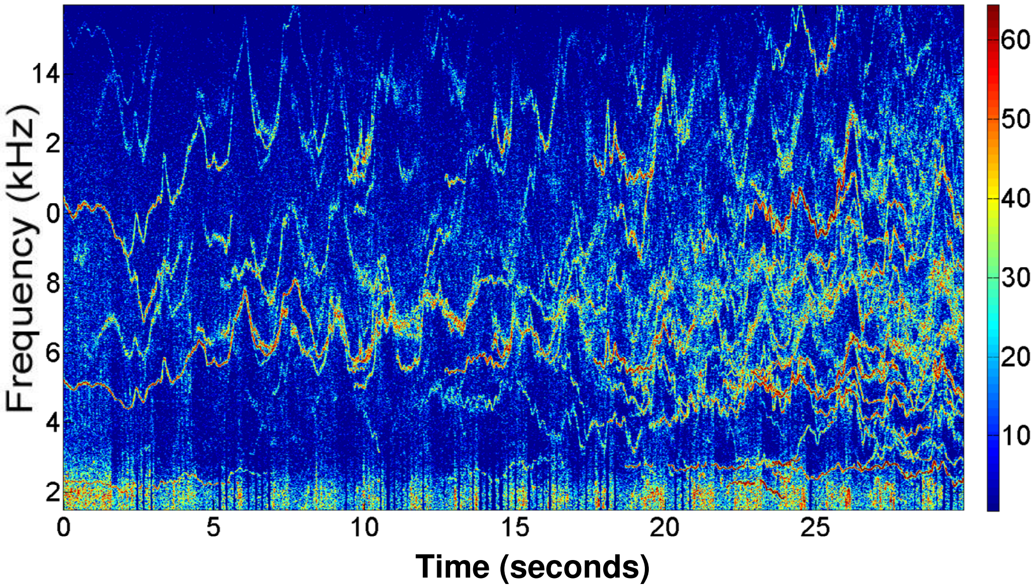

Figure 4.7 – Storm-generated winds produce noise related to snow blowing over ice or leads opening.

Ross observed that wind-driven wave noise significantly contributes to open-ocean ambient noise between 200 and 500 Hz (Ross, 1976). However, assessing spectral noise dependence in the Arctic based purely on wind presents a difficult problem in relation to the influence of ice cover. Sound-pressure levels at 250 Hz were plotted as a function of wind speed for the site B data from September 2006 – May 2007, and compared with Ross's measurements (see Figure 4.8). Ambient noise during late summer – when exposed to open water – correlates with wind speed and is apparent above 7 m/s (13.6 kts). There are also intermittent correlations in winter and spring associated with the opening of leads, but there is a time lag between wind speed and acoustic pressure levels. The median wind speed during this study was 12 kts, and the highest daily-average reached over 40 kts.

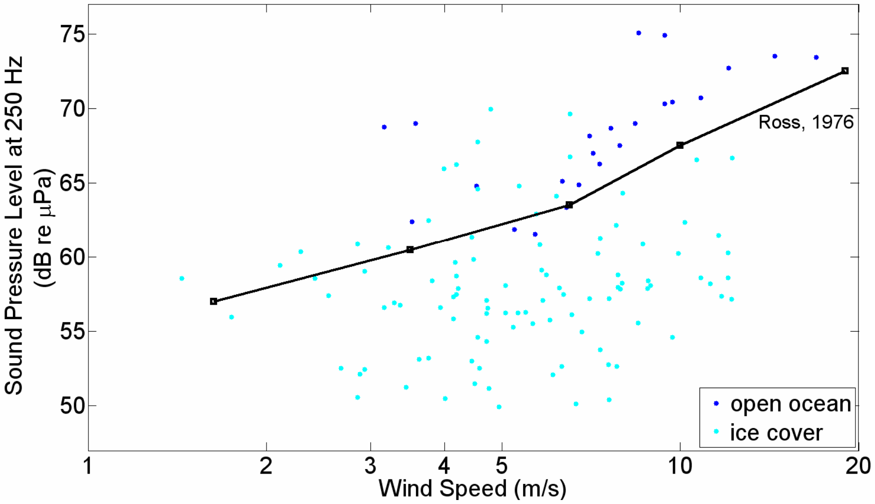

Figure 4.8 – The influence of wind-driven surface wave noise is only apparent in open ocean conditions above 7 kts, implying Arctic ambient noise generally has a stronger dependency on the seasonal variation of sea ice concentration.

Bioacoustic Detections

All species of marine mammals found in the Western Arctic produce characteristic calls that can be used for acoustic identification (Stirling 1983, Bel'kovitch 1993, Moore et al. 2006, Clark et al. 1996). Long-term averaged spectral time series were scanned visually for the presence of known call-types for the five most common species in the area of study – the bowhead whale, beluga whale, bearded seal, ringed seal, and walrus. Each detection was logged and the species identification confirmed by audio playback through headphones. Acoustic detections were grouped into hourly bins for the three most readily identified species – bowheads, belugas, and bearded seals – and the number of hours per day during which calls were detected, were plotted for each of these species.

Although extensive recordings have been made north of Barrow between April and June over the past 18 years (Van Parijs, Clark 2006), little or no acoustic recording has been undertaken in this area between the months of November and April. With the addition of winter and spring months, detection time series for bowheads, belugas, and bearded seals are presented along with representative spectrograms of recorded calls for late Sepember 2006 through the end of May 2007. Comparing the time series of detected calls for each species to environmental correlates (see Figure 3.7), especially the extent of sea ice coverage, provides some interesting insights into the timing of species movements and seasonal acoustic behavior.

Western Arctic bowhead whales have a well-documented migration route, passing north of Point Barrow while traveling between summer feeding grounds in the eastern Beaufort Sea and winter feeding areas in the Chuckchi and Bearing Seas. Bowhead calls were mainly detected during times of ice formation in the fall and then again during the spring breakup. However, an unexpected detection of bowhead whale calls occurred in the middle of January (see Figure 4.9). This appears to conincide with a case where strong winds sufficiently moved pack ice to open leads (i.e. ice cover <100%). Presence of bowhead whales off Barrow in the winter has been reported, but is not commonly observed. As this is the first over-winter deployment of an autonomous acoustic recording package in this area, one possibility that must be considered is that there has been insufficient observation to date during winter months to confirm whether bowhead whale occurence during winter is common.

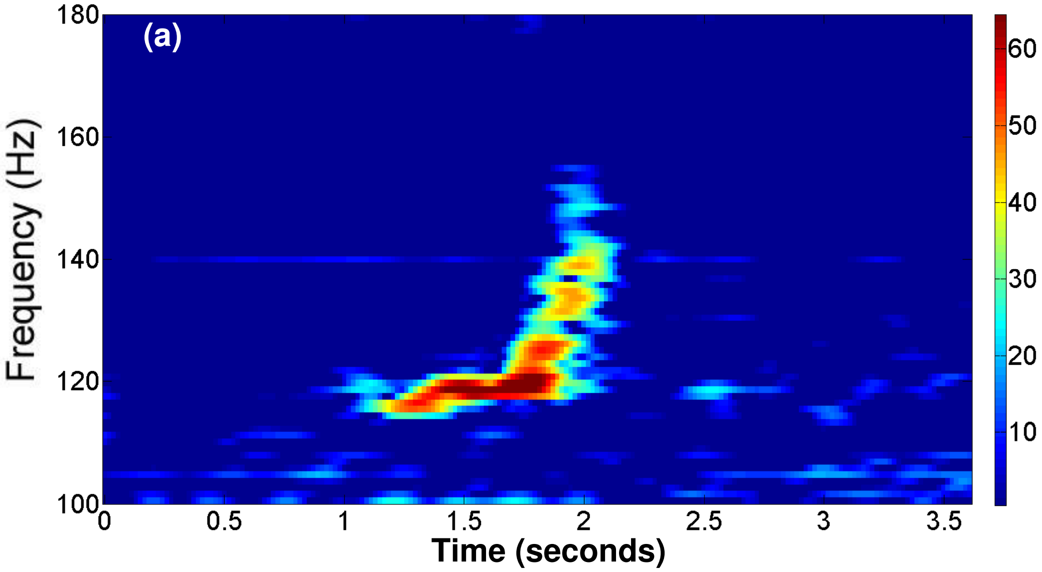

Figure 4.9 – Bowhead whale call detections: (a) typical bowhead whale upsweep call, (b) typical bowhead constant call, (c) plot showing the hours per day during which calls were present for all months of recorded data. The call detection in January represents a 20-minute period during which bowhead whale upsweep and constant calls were heard repeatedly. Fewer calls recorded in the fall could be due to the fact that the migration route is usually closer to the coast for foraging on the westward return at the end of summer. In spring is when bowheads are vocal and produce songs.

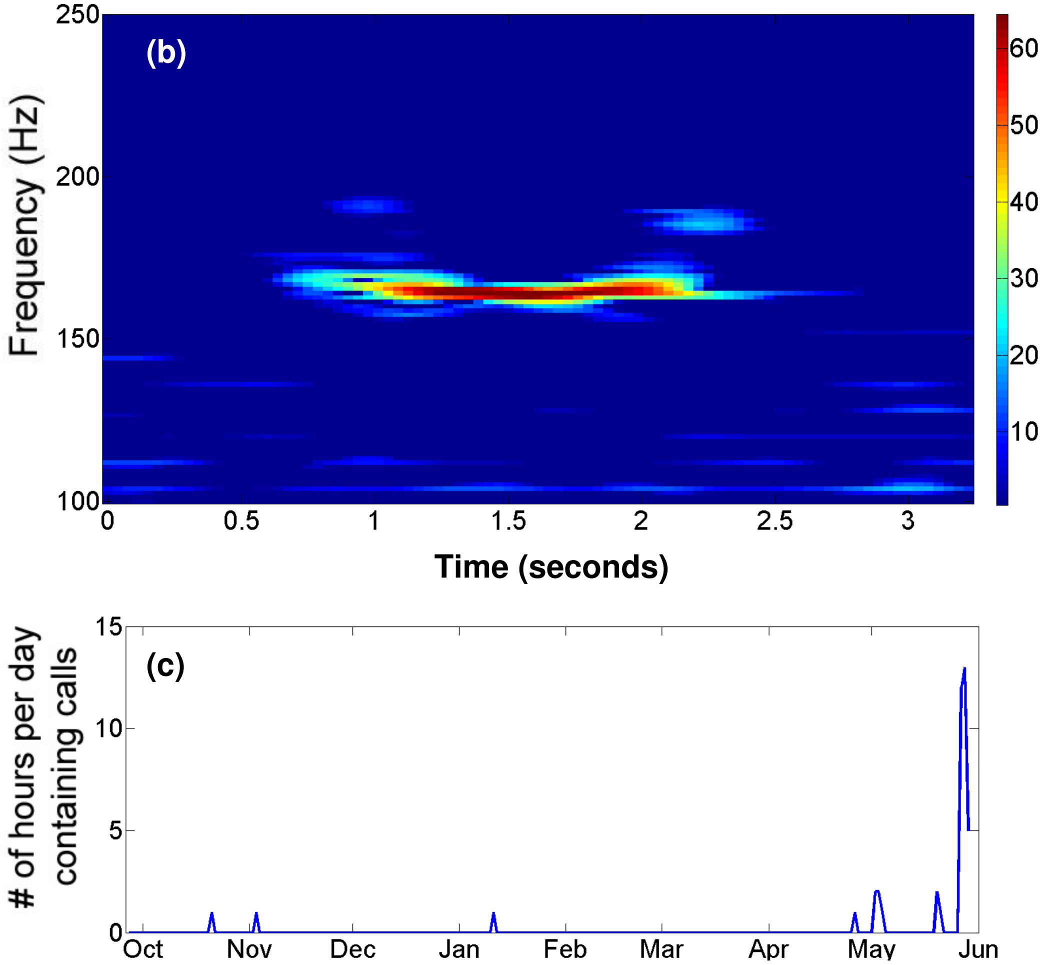

Figure 4.9 – Continued

Belugas from the eastern Chuckchi Sea have been observed by aerial surveys and satellite tracking to prefer the edge of the pack ice, but also to travel in open water as well as hundreds of kilometers into 90% ice cover (Suydam et al. 2001). As expected, beluga calls were detected throughout times of open water and into the late fall and early spring during ice formation and breakup. Beluga clicks and whistles were commonly present up until mid-November, occured again in early December after the ice cover had reached 100% and receded slightly, and then were not detected again until mid-April (see Figure 4.10).

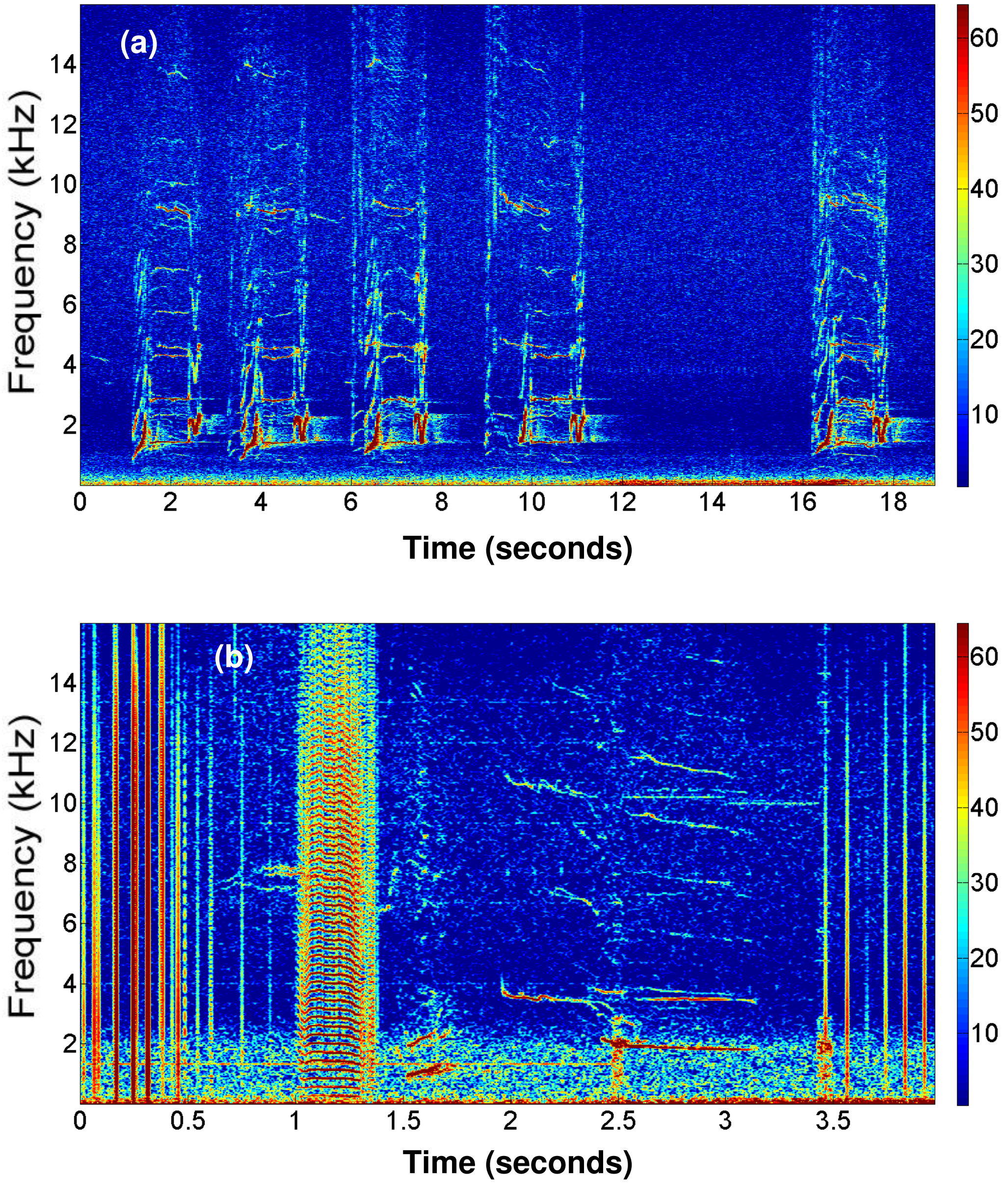

Figure 4.10 – Beluga whale call detections: (a) whistles, (b) clicks and whistles, (c) plot showing the number of hours per day during which beluga calls were present for all months of recorded data.

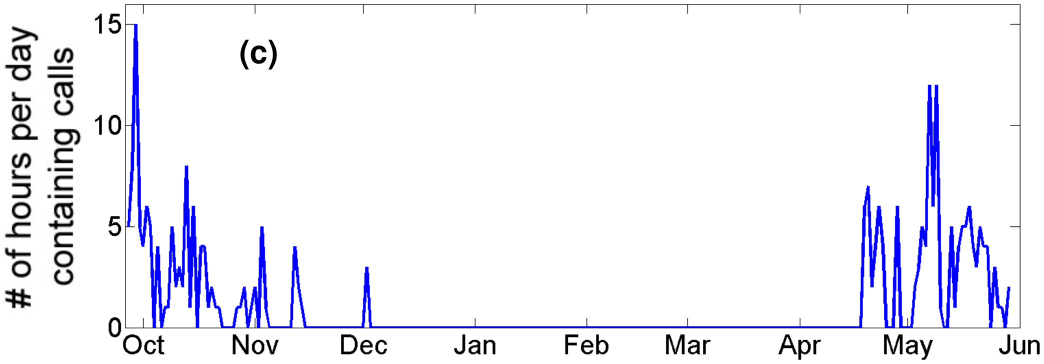

Figure 4.10 – Continued

Male bearded seals exhibit seasonal acoustic behavior associated with mating. This has been reported to take place most commonly from April to July (Van Parijs et al. 2001) with calls reported as early as late winter (Stirling, 1983). During this time males produce four categories of vocalizations – trills, ascents, sweeps, and moans. These calls are highly stereotyped with stocks having distinct repertoires that have remained stable on decadal timescales (Risch et al. 2007).

Most previously described bearded seal call-types for the western Arctic (Risch et al. 2007) were present in the data during the spring as expected, but also from December through the end of February. This mid-winter calling behavior has not been reported to date, which could be due to the fact that long-term recordings have not been made in this area earlier than April. One additional highly-stereotyped call was recorded during a two-week period of ice formation in November (see Figure 4.11a). This is likely a bearded seal sweep that has not been described for this population to date.

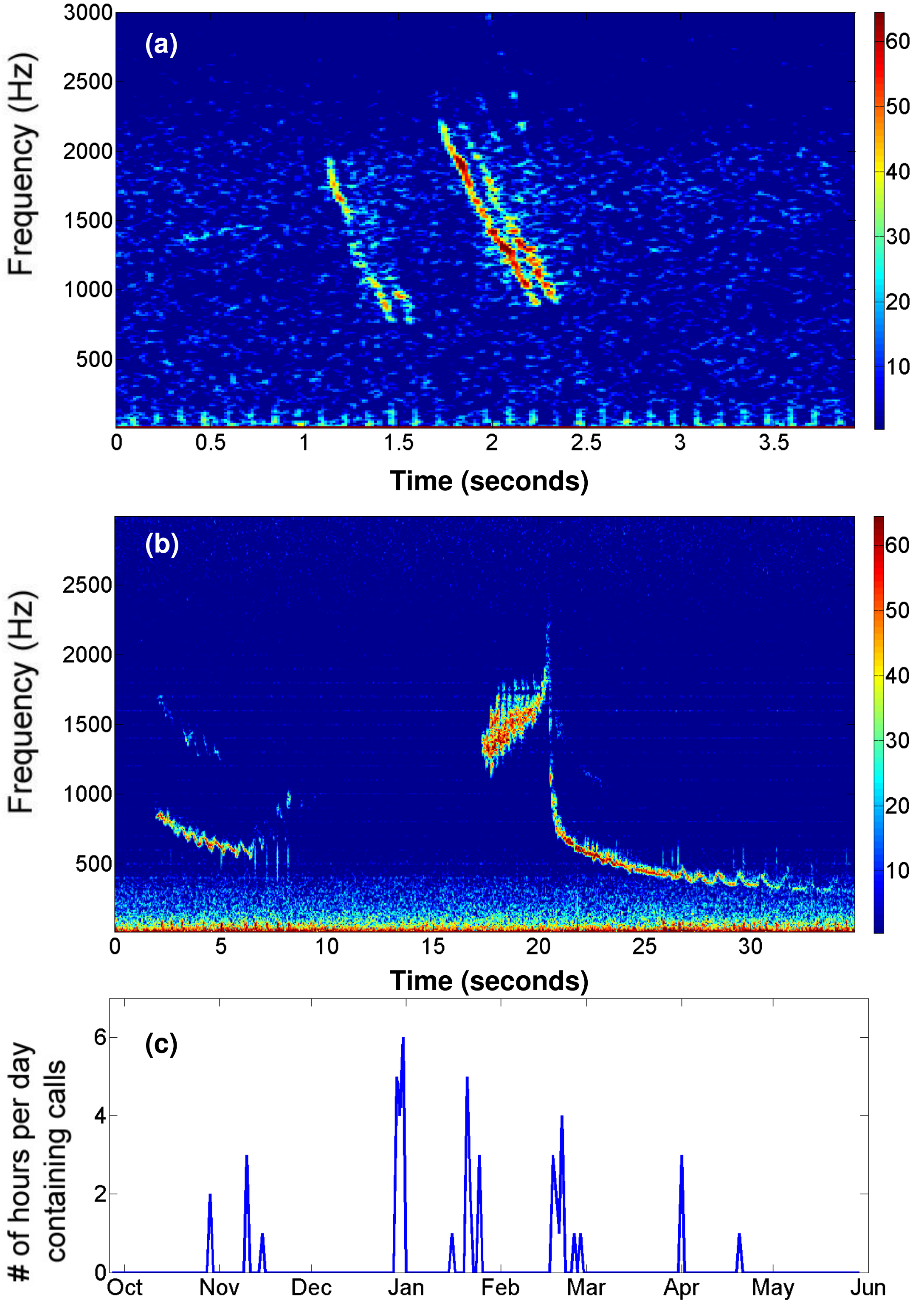

Figure 4.11 – Bearded seal call detections: (a) typical early winter bearded seal downsweep (Nov-Dec), (b) bearded seal trills, (c) plot showing the hours per day during which bearded seal calls were present for all months of recorded data.

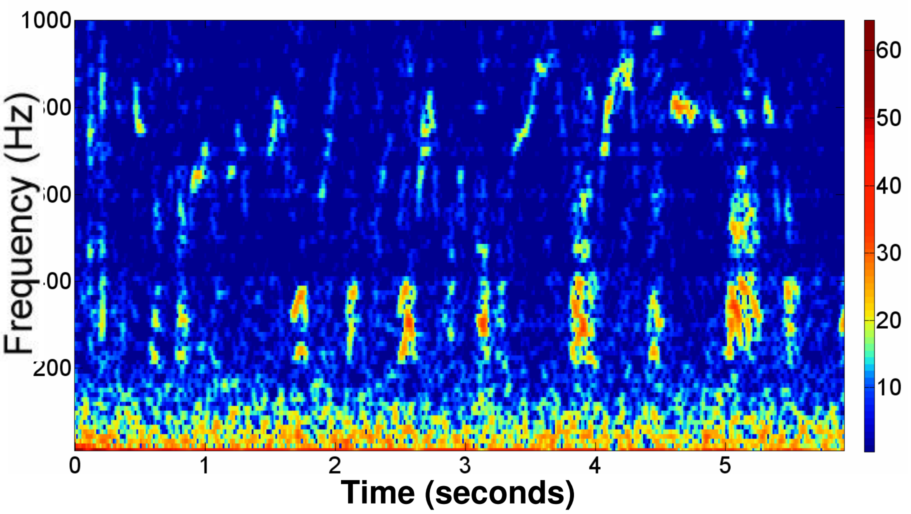

Figure 4.12 – Representative spectrogram of a commonly encountered ringed seal calling sequence in which multiple low-frequent barks are interspersed with higher frequency yelps.

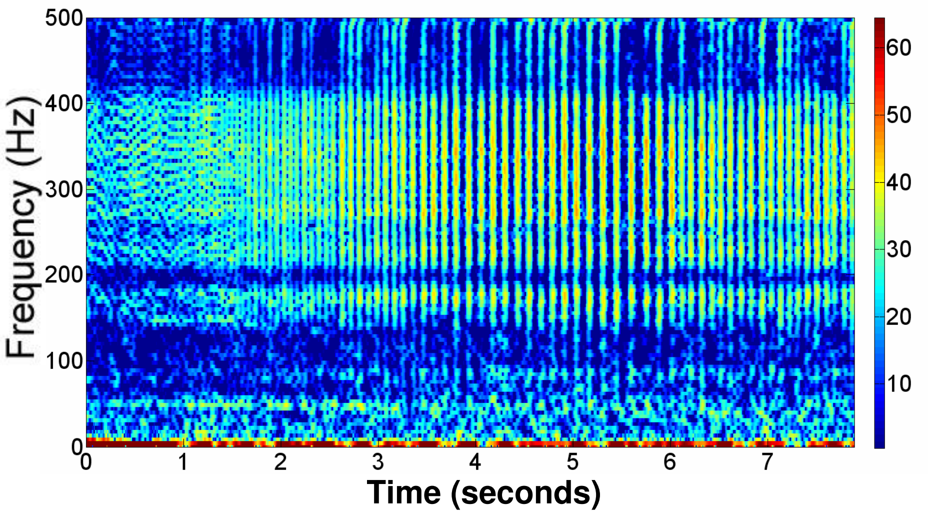

Figure 4.13 – Spectrogram showing a rapid series of walrus knocks. Although walrus are known to produce a variety of sounds, including the unique bell-like call of the male, this rapid knocking represents the predominant walrus call in the dataset.

V. DISCUSSION

Arctic Sound Propagation

Because of the combination of upward refraction, under-ice reflection, and high scattering strength, long-range sound propagation is highly dependent on the state of sea ice. Therefore transmission loss may increase at a rate faster than cylindrical spreading as frequency increases (see Figure 5.1); thus high-frequency acoustic waves will attenuate with increased range (Yang and Votaw, 1981). Reflection and transmission coefficients are typically dependent on interactions with the boundary interfaces, but in the Arctic they are generally proportional to the thickness of sea ice, and as a result determine the shape of the frequency-dependent ambient noise spectrum (Diachok and Winokur, 1974).

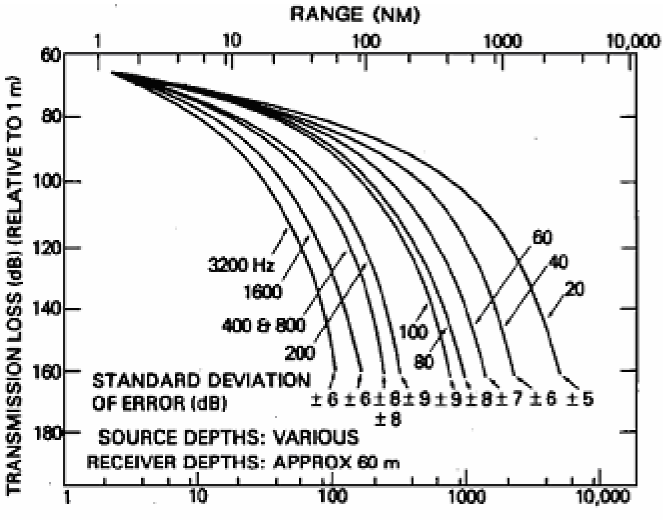

Figure 5.1 – Transmission loss measurements versus range in the Arctic Ocean for various frequencies (Buck, 1968).

Geometric spreading and bulk attenuation alone cause low-frequency transmission loss in the Arctic waveguide by as much as 10^{-2} dB/km at 20 Hz and 10^{-1} dB/km at 80 Hz. Frequency dependence of such loss is proportional to $f^{1.5}$ or f^{2}

(LePage and Schmidt, 1994). The highly refractive upper duct – which extends about a hundred meters into the water column layer – completely strips energy from trapped ray bundles after propagating less than a hundred kilometers, leaving a residual field of deeper diving rays. At shallow depths these rays are less excited and sound sources couple most energy into the lower-order modes, thus surface interaction losses still dominate at low frequencies (LePage and Schmidt, 1994). This mode stripping is the result of lower-order modes being trapped in the surface channel and interacting continuously with the underside of the ice cover, resulting in high scattering loss. Higher-order modes are influenced by the deep pressure gradient associated with convergence zone paths, and therefore interact less with the ice cover. This implies that lower-order modes can be neglected when considering long-range propagation (LePage and Schmidt, 1994). In a shallow-water waveguide there is a remarkable loss of higher propagating modes in the 12.5-25 Hz band (Milne and Ganton, 1964).

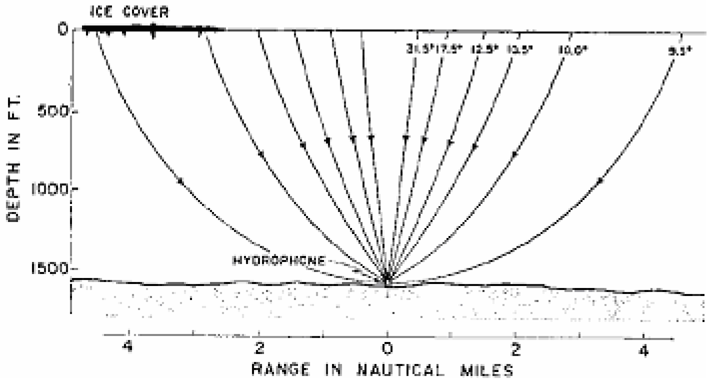

Figure 5.2 – Ray paths from sources at the surface propagate directly to a bottom-mounted hydrophone. Angles are with respect to the surface. The bottom limiting ray grazed the ice-water surface at 9.5° with a range of 4.3 miles, enclosing a circular area of 59 square miles (Milne & Ganton, 1964).

The contribution of high-frequency acoustic waves is largely the result of noise-generating mechanisms from sea ice that propagate to the hydrophone by direct ray paths. Lower frequencies around 10 Hz contribute from much farther distances, with wavelengths in excess of the scale size for under-ice projection (Milne and Ganton, 1964). According to Snell's law, acoustic rays can only propagate across distances greater than 30 km in the ice-water interface if the grazing angle φ is less than 15° (see Figure 5.2). Reflection loss has to be much greater than zero because the sea ice canopy is interspersed with rough ridges (Diachok, 1976). Statistically, the loss per under-ice reflection is almost 15 dB when grazing angles are between ±7.5° and ±8.5°. Waves reflected off the seafloor make many more under-ice reflections (see Figure 5.3) than those confined to refracted paths within the upper water column (Milne and Ganton, 1964).

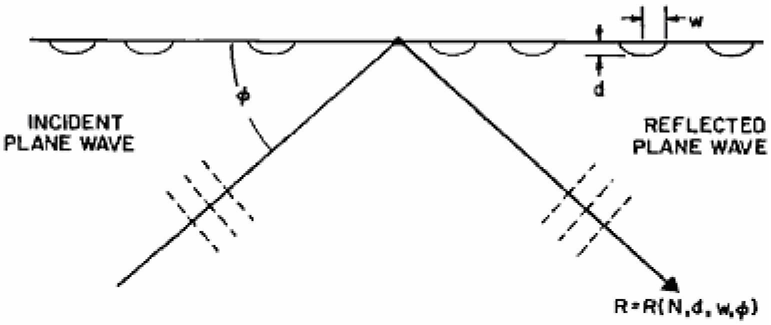

Figure 5.3 – An acoustic plane wave reflected from a random distribution of elliptical half-cylinders (Diachok, 1976).

Ambient Noise Level Distributions

It has been demonstrated that Arctic ambient noise varies uniquely from all other ocean environments in regards to its spatial and temporal variability related to sea ice and in many cases wind. Already during summer and early fall though, there is significant acoustic energy derived from other transient signals, namely anthropogenic noise sources. When examining the low-frequency spectral levels in Figures 3.3 and 3.4 compared to the background noise levels in Figure 3.1, it appears that September should be the noisiest month based on the natural variability of sea ice and wind in space and time, but in actuality the October sound-spectrum experiences substantially higher noise-levels primarily due to the residual energy of seismic exploration reflecting off the seafloor and propagating through the waveguide.

Buck and Wilson reported ice cracking noise levels near a ridge to be 100 dB at 10 Hz; Lewis and Denner also detected noise levels at 10 Hz as high as 100 dB in winter; Makris and Dyer observed a broad peak associated with ice cracking around 15 Hz reaching 90 dB. Background noise levels in Figure 3.1 vary above and below 87 dB re µPa at 10 Hz and are consistent with the tail end of Webb's microseism band, but by observing the density distributions for all transient acoustic events present in the data, ambient noise levels can reach upwards of 150 dB re µPa to as low as 70 dB re µPa. The shape of spectral background-noise in the 10-50 Hz band is normally attributed to the influence of distant global shipping for Pacific deep-ocean ambient noise (McDonald, 2006). Since the shallow waters of the Bering Sea prevent this trans-oceanic propagation from being introduced to the Arctic underwater environment, there is no explicit frequency band attributed to the influence of ship cavitation noise.

Noise levels for nearly every month are shown to be non-Gaussian below 20 Hz since the mean sound-pressure levels are above that of the median and translate into a shift of the distribution peak to the right. In addition, the contributions of localized high-energy impulsive noise to the sound spectrum imply that the distribution function is long-tailed on the right side. Building upon the concept of

Dyer’s statistical sound transmission, since multipath propagation is affected so much by high under-ice scattering strengths, then the lower spectral levels for nearly every month generally exhibit the same shape and are often close to median levels, implying the distribution function is short-tailed on the left side. For certain months, probability densities were very broad and were found to resemble chi-square distributions. As frequency increases and extends into higher bands, the ambient noise level density distributions become closer to near-Gaussian levels.

Sea Ice Kinematics

The dynamics of sea ice determine its extent, concentration, thickness, rigidity, and variations throughout different seasons and regions, thus introducing causality on both temporal and spatial scales. One noise-generating mechanism can produce broadband spectral energy across many frequencies, which in turn can mask other noise variations induced by a different mechanism. For instance, fluctuations in thermal fracturing of sea ice for a given air temperature is highly regionally dependent, but during non-summer months when acoustic-noise amplitudes reach pressures greater than 10^3 μPa, thermal fracturing is the dominant noise source responsible for Arctic ambient noise episodes at 1 kHz (Lewis and Denner, 1988).

Pack ice consists of seasonal and perennial (i.e. multiyear) floes up to 2-3 meters thick in near-continuous contact over large areas of the high Arctic, and interspersed with pressure ridges heaped together by piled rubble formed through collisions and shear interactions between adjacent floes (see Figure 5.4). These ridges are several meters wide and can weather to heights of a few meters above the sea surface (i.e. ice "sails"); ice keel depths reach three to five times the ridge height and their cross-sectional contours are highly variable. Most ridge keels are flattened at the bottom due to ablations and scouring over time, and tend to converge with the surface at steep angles (Diachok, 1976). Although completely random, the average spacing between pressure ridges has been shown to be about 100 meters (Diachok, 1976). Historically, nearly 80% of sea ice would lie beneath the sea surface, but due to the rapid decline of thick perennial sea ice, newly formed thin and frail seasonal ice is mostly found at the surface, where it is exposed and vulnerable to solar radiation.

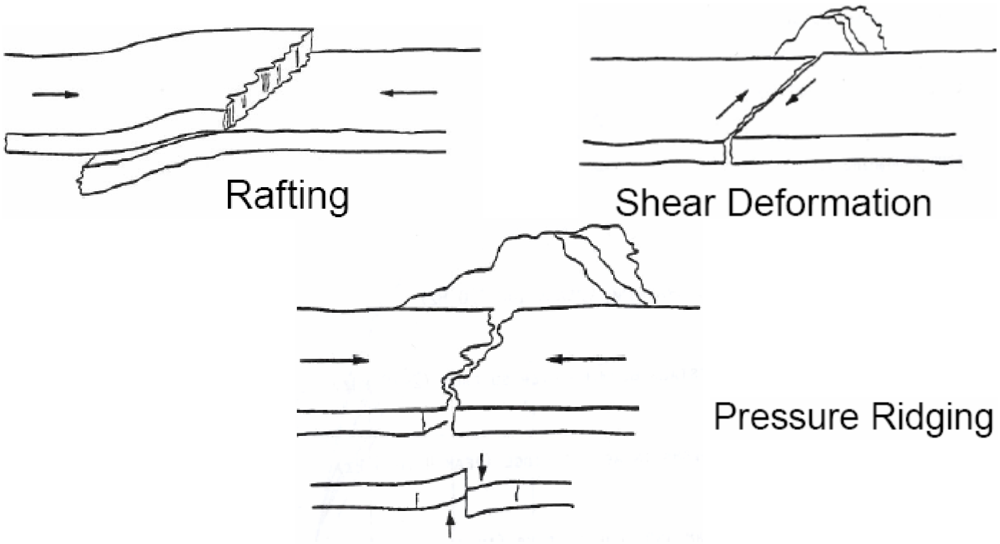

Figure 5.4 – Sea ice kinematics

Following low atmospheric-pressures, low air temperatures and decreasing winds lead to thermal fracturing of sea ice, which makes significant contributions to ambient noise at frequencies less than 150 Hz. Broadband noise associated with thermal ice cracking processes extends from 5 kHz to as low as 30 Hz and sound-pressure levels can exceed those of sea sate two in open ocean conditions. Most thermal stress occurs within the upper 20 cm of sea ice. It has been shown that 30% - 40% of acoustic noise events in non-summer months correspond with changes in heat flux (Lewis and Denner, 1988). Transmission in the 32-Hz frequency band reaches length scales of 660 km in fall and 1000 km in spring (Lewis and Denner, 1988), while high-frequency fracture noise can propagate over ranges of approximately 150 km during the fall season, increasing to 300 km in spring. Thermal fracturing appears to dominate noise transmission during non-summer months, as opposed to motion-induced fracturing, but the natural variability in atmospheric forcing decides these length scales.

It is not entirely the temperature value itself, but in fact the rate or flux of decrease in air temperature over time that produces fracturing due to thermal stress; this corresponds with large increases in impulsive noise (Ganton and Milne, 1965). Milne and Ganton observed that the production of tensile cracks associated with this impulsive noise is characterized by a Poisson density distribution over time. Under rising air temperatures, the sporadic nature of this noise disappears and a near-Gaussian distribution reappears (Kibblewhite and Jones, 1976). In the fall and winter seasons, thermal fracturing processes involve the loss of heat as a result of long-wave radiation, whereas the spring season is subjected to a combination of atmospheric short-wave solar radiation, snow cover, and long-wave radiation, driving thermal waves into the sea ice. The resulting fracture noise can be radically modified on a daily basis as a result of meteorological conditions such as cloud cover and blowing snow (Lewis and Denner, 1988).

The slow fracturing of hardened pack ice over several tens of kilometers – resulting in open leads – releases tremendous amounts of acoustic spectral-energy. Thermal ice-cracking noise however, is more localized and propagates on the order of meters or tens of meters, generating less spectral-energy per crack than lead-forming fractures. In order for ice to crack, its temperature must be lower than typically -23 °C, but also depends on the thickness of the pack ice (Zakarauskas et al. 1991).

Makris and Dyer described the behavior of sea ice concentration on short spatial and temporal scales through semidiurnal inertial oscillations of ice floes in free drift. Meunch et al. speculated that long internal waves originating near the ice edge at the sea surface may be generated by wind-stress forcing, thereby advecting the ice field into bands of alternating convergence and divergence zones. It was shown that the generation mechanism for long internal waves was absent in the presence of wind-driven surface gravity waves (Makris and Dyer, 1991).

Shifts in Sea Ice & Waveguide Propagation

The viability of sea ice in the Arctic Ocean – namely the thickness and concentration of perennial ice coverage – is crucial in allowing the water column to retain thermal energy by limiting melt and evaporation at the surface layer. The ice albedo effect is a vital process necessary to prolonging the stability of thermohaline circulation between the exchange of cold salty bottom water in polar regions and warm fresh surface water in equatorial regions. Simply put, sea ice plays a pivotal role in the Earth's water cycle. This study recognizes that critical importance, but endeavors to take a different approach than large-scale remote sensing by exploring the intricate seasonal variability inherent in correlations between local sea ice conditions and ambient sound-pressure levels that acousticians like Milne and Ganton first observed in the 1960s.

As the rate in which the disappearance of multiyear pack ice increases due to warming climate regimes, sea ice thickness will be considerably reduced and the ice field will become more susceptible to solar heat radiation. If the strength of ice albedo is diminished, then melt ponds will form due to surface interactions with air temperature. These bodies of water will in turn absorb sensible heat flux exchange and sea surface temperatures will rise. Thermal breakup, melt, and evaporation will begin to occur earlier in spring each year because of this positive feedback mechanism, and will also cause ice formation to occur later in fall depending on the variability of atmospheric circulation. Once the majority of historic multiyear ice is replaced by frail seasonal ice floes, water temperatures may consistently increase over many months throughout the year, and feedback may occur exponentially in time.

The unique seasonal and temporal variability associated with noise spectrum levels in the Arctic underwater sound environment will begin to also disappear during many months of the year, and eventually may resemble ambient noise in the open ocean more so than when subjected to ice cover. The rough surface boundary layer of sea ice – which generally scatters and attenuates sound waves subjected to under-ice reflections – will be replaced by the common air-water interface – a nearly perfect reflector due to such a significant density gradient. Transmission loss will decrease substantially and long-range propagation will contribute more to ambient noise levels. Additionally, the continental shelf north of Alaska is only 50-100 m deep, so shallow-water propagation will trap acoustic energy in the waveguide and transmit over great distances.

It will become rare for background noise levels to generally maintain low pressure levels while being interspersed with transient impulsive events. Ambient noise will become uniformly noisier and may resemble the near-Gaussian distributions attributed to noise in the Pacific and Atlantic Oceans. Only during the fixed winter freeze-up of seasonal ice cover will the presence of impulsive noise still be encountered.

The Marginal Ice Zone

The Marginal Ice Zone (MIZ) is spatially defined as irregularly scattered ice floes along the pack edge, ranging from a few hundred meters to tens of kilometers depending on local wind velocity, current velocity, air temperature, and water temperature (Diachok and Winokur, 1974). Stress and strain mechanisms are uncoupled when the ice field is subjected to free-drift conditions. Incoming surface waves can cause flexural fractures and unloading motions that directly radiate noise, while asperities on the edge of adjacent floes also produce noise as they break off or vibrate in response to gravity wave motion. Collisions between ice floes contribute noise to frequencies less than 20 Hz (Makris and Dyer, 1991).

The MIZ boundaries are prevailing sources of ambient noise, where sound-pressure levels have been measured 12 dB higher near a compact ice edge than in open water, and almost 20 dB higher than under the ice canopy; a dispersed or scattered ice edge exhibits levels 4 dB higher than measured in open water and 10 dB higher than under the ice canopy. Relatively high ambient noise levels extending from the MIZ to the ice edge result from interactions with physical phenomena such as gravity waves, storm swells, and wind-driven surface waves. These propagating ocean waves eventually dissipate through nonlinear interaction with individual ice floes or the compact ice edge, and the resultant energy is converted into flexural motion, thereby breaking up sea ice and inducing turbulence (Diachok and Winokur, 1974).

Diachok and Winokur demonstrated that the spectral shape of ambient noise throughout the MIZ is spatially dependent on sea ice regardless of sea state (see Figure 5.5); noise levels at the diffuse ice edge differ by 15 dB between sea state 1 and 5 due to increases in wind velocity (Diachok and Winokur, 1974). During summer, there is a broadband correlation associated with ice floes moving through water, while the kinetic energy of ice parcel translation is the dominant source of high-frequency noise generation. In the fall, ambient noise levels at 10 and 32 Hz correlate linearly in proportion with both ice parcel speed and shape due to the deformation and translation of pack ice. As individual ice floes grind and slip past one another, adjacent bonds are broken and rearranged into new shapes. Only in winter is the differential motion of ice floe convergence responsible for low-frequency noise (Lewis and Denner, 1988).

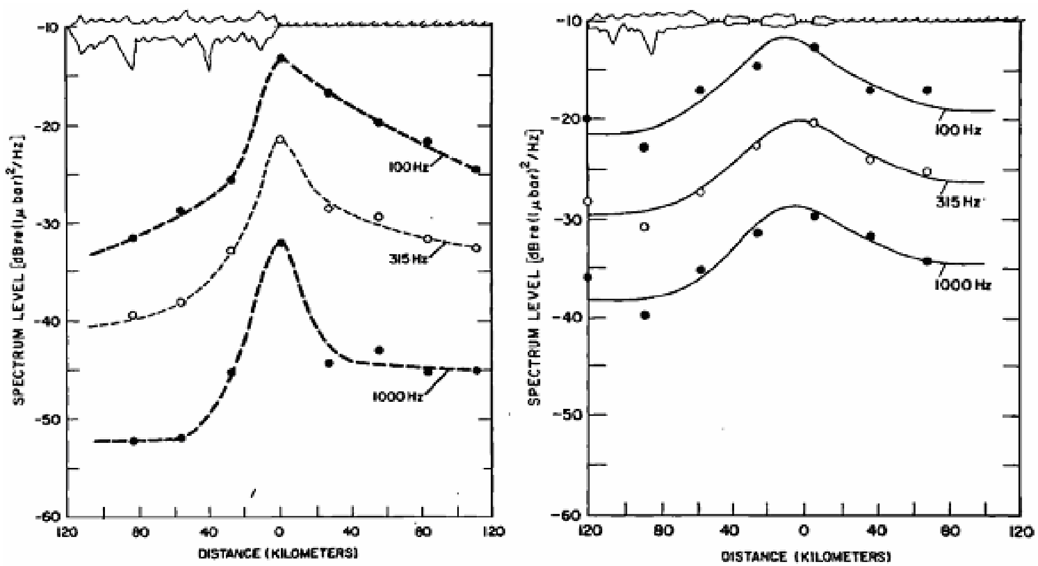

Figure 5.5 – Variations in ambient noise spectrum levels for frequencies of 100, 315, and 1000 Hz. On the left is a compact ice edge at sea state 2; on the right is a diffuse ice edge at sea state 5 (Diachok and Winokur, 1974).

Contribution of Noise-Generating Mechanisms

The two primary noise-generating mechanisms attributed to sea ice dynamics include pressure ridging and thermal fracturing. As the Arctic increasingly becomes seasonsally ice-free, these two processes will both be affected, but in different ways. Ridging is primarily the result of moving ice floes interacting with one another in the ice field until increases in pressure and wind forcing determine the spatial dimensions of pack ice. The MIZ will continue to increase both spatially and temporally throughout the year, with greater spacing between adjacent floes. This allows for the excitation of wind-driven surface waves to speed up moving ice floes, thus instigating more substantial collisions due to shear translation and deformation. Ice keels and ridges may be formed every year on an accelerated basis, inciting high levels of noise due to such ridging processes.

The variations in sound-pressure levels due to thermal fracturing are dependent upon the rate in which atmospheric air temperatures suddenly decrease. Besides the height of winter, most other months will keep undergoing climate regime shifts toward warmer air temperatures, thus the temporal extent in which impulsive thermal noise is prevalent will potentially narrow down to around the peak winter season. This will raise some issues during spring regarding the opening of leads and the tensile breakup of pack ice; melt and evaporation are already dominating most of the spring ice breakup.

Anthropogenic noise sources such as seismic exploration and shipping activity will undoubtedly increase as the seasonal decline of sea ice presents more opportunity for maritime presence. We will observe that as the open-water season continually increases in both space and time, industry will take advantage of these conditions during months that have never before been exposed to substantial pressure levels of man-made noise. There is concern not only for significant increases in future ambient noise measurements, but more importantly the potential impact that such anthropogenic effects can have on marine mammals in the local region.

Statistical Density Distributions

If acoustic transient events occur often, propagate over long distances, and overlap in time, then the central limit theorem infers that the complete noise spectrum will exhibit Gaussian statistics. During winter and spring, Arctic ambient noise is characterized by the composite of discrete and highly impulsive sea ice fracturing events caused by thermal, wind, drift, and current stresses acting on pack ice (see Figure 5.6). Such impetuous and localized episodes stand out above the continuous Gaussian background, therefore changing the overall density distribution to non-Gaussian and nonstationary (Zakarauskas et. al, 1991).

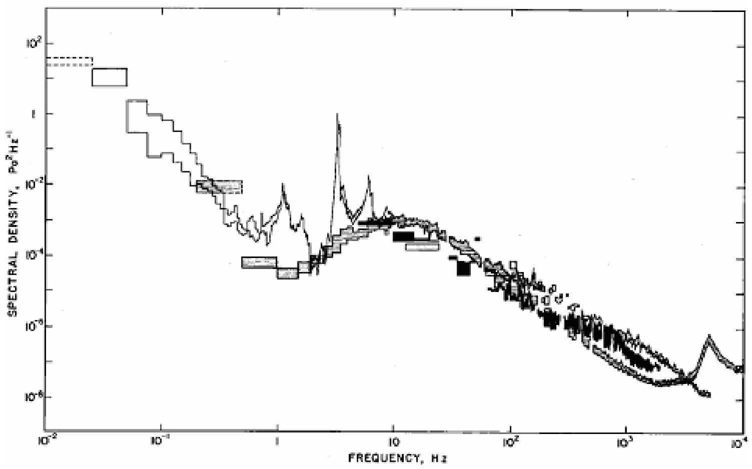

Figure 5.6 – Composite of ambient noise observed in April 1982 at the Fram IV ice camp. Peaks from 1-10 Hz are caused by hydrophone cable strum, the 15-Hz peak is associated with ice cracking events in response to various environmental forces, the 300-Hz peak occurs only during periods of atmospheric cooling, and the 6-kHz peak is hypothesized to occur only upon floe-floe bumping (Makris and Dyer, 1991).

Inherent differences in statistical density distributions between winter/spring and summer seasons led Milne and Ganton to suggest there are fundamental differences in noise-generating mechanisms and processes due to sea ice dynamics. Highly impulsive, non-Gaussian ambient noise levels in the 12.5-25 Hz frequency band during spring are dominated by mechanical activity associated with thermal stresses that often occur in shore-fast sea ice. The influence of relative motion on ice floes during late summer also exhibits a similar non-Gaussian statistical distribution in this frequency band. It is only in winter however that high-energy noise spectra at these frequencies is close to Gaussian and contrasts that of spring and summer due to fully-hardened ice coverage. The absence of impulsive noise in the 200-400 Hz band reveals a near-Gaussian spectral distribution during summer in contrast to that of springtime, while the 3.2-6.4 kHz band is impulsive and therefore non-Gaussian during summer in contrast to a Gaussian distribution in spring (Milne and Ganton, 1964).

The non-Gaussian nature of thermally induced impulsive noise is characterized by a spectral-energy peak between 100-400 Hz with a slope of -12 dB/octave at higher frequencies (see Figure 5.7). Milne and Ganton observed that a profusion of localized thermal fracturing accounted for a near-normal Gaussian statistical density distribution for ambient noise spectra above 1 kHz when derived from a superposition of these impulsive acoustic events. They also noticed though that the frequency band between 100 Hz and 10 kHz exhibited spectral levels that could either decrease as a function of logarithmically increasing frequency or were entirely frequency independent. Because of sea ice cover, spectrum levels for wind-generated noise were usually Gaussian in nature and essentially frequency independent between 100 Hz and 10 kHz (Milne and Ganton, 1964).

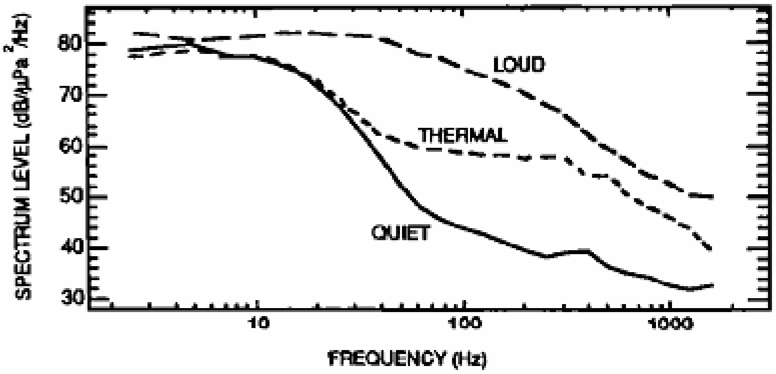

Figure 5.7 – Power spectrum levels in third-octave bands of three ambient noise samples (Zakarauskas et. al, 1991).

Implications for Arctic Marine Mammal Research

Long-term continuously recorded acoustic data from the coastal Arctic Ocean can provide an effective tool for studying aspects of marine mammal populations that are difficult or impossile to study using other methods of observation. Intra-annual variability in calling behavior of three species was readily assessed, showing the strong seasonal signal expected for animals whose distribution is closely tied to the extent and state of sea ice. By overwintering the instruments under 100% ice cover, aspects of ice seal distribution and behavior that had not been previously recorded were observed; sporadic events like the appearance of a calling bowhead whale in January were detected. There were also several unidentified biological calls recorded. Further investigation may show the presence of rarer ice seal species in this region, like ribbon and spotted seals.

The 2006 data from the two HARPs deployed north of Barrow will provide an important baseline for future comparisons of the distribution and seasonal behavior of marine mammals in the western Arctic. For example, multi-year comparisons will make it possible to infer whether ice seals are shifting closer to or farther away from the coast during the winter or spring seasons, or whether formerly uncommon or rare species are moving into the study area. Correlation with the environmental variables of ice cover and wind may help to explain some of these changes. Furthermore, male bearded seals typically produce calls during the breeding season from April to July, but all four types of mating calls were recorded as early as December. While it is not possible to determine if this is typical due to a lack of previous recordings during winter months, a time series of year-long recordings spanning multiple years should help to shed light on trends, if any exist, in the timing of mating behavior of this species.

Another example of the value of multi-year comparisons of biological detections in this region is the gray whale, not treated in this analysis. It is important to note that although historically uncommon in this region of the Arctic, gray whale sightings have increased over the past decade and calls were recorded throughout the winter during a 2003 long-term deployment of three previous-generation HARPs in the Beaufort Sea to the southwest (Stafford et al. 2007). This implies that significant changes in the distribution of this species may be underway. It will be possible to study this by recording year-round continuous acoustic data.

Autonomous acoustic recording can be used reliably to confirm the presence of marine mammal species within some radius of detection from the instrument locations. For this reason, long-term acoustic recording can provide an effective tool for monitoring changes in the distribution of marine mammal species over time as changes in sea ice and other environmental conditions cause shifts in the ecological regimes of the Arctic. Current limitations of autonomous long-term recording are that, while presence of a species can be confirmed from call detections, species abundance can not be infered from calling rates. Furthermore, species absence can not be confirmed by acoustic methods alone when calls are not present, due to variations in calling behavior (Stirling 1983, Van Parijs 2001). One special exception to some of the limitations in the area of more detailed population studies may be the bearded seal.

Vocalizations of male bearded seals north of Point Barrow have shown individual characteristics that have remained stable on decadal time scales (Van Parijs 2006). By providing an acoustic proxy for traditional mark recapture methods, this opens up the possibility to study demographic and behavioral aspects of marine mammal populations.

VI. CONCLUSION

Combined with ancillary measurements, long-term acoustic monitoring provides an effective tool for observing changing levels of ambient sound related to declining sea ice, environmental mechanisms, and man-made noise, while simultaneously detecting marine mammals. Acoustic baseline measurments over the next several years are needed for further analysis in order to observe and compare shifts in ambient noise due to the current trends in sea ice decline and increases in anthropogenic noise. Continuing the long-term acoustic data time series at monitoring sites around the North Slope will facilitate inter-comparison to reveal shifts in seasonal trends. The critical timing of this study is substantiated by the time-variant impact of sea ice decline due to the advent of climate change in polar regions.

A particularly interesting facet contained in the first-year dataset is being explored as a separate study. There is much potential for accurate development of an acoustic-source propagation model for seismic airgun activity – based on modal dispersion data collected by the hydrophone – used in conjunction with survey track lines from 2006. This will help to investigate the possibility of potential impact on bowhead behavior by providing estimates of received sound-pressure levels that animals are exposed to, based on the amount of energy transmitted from the seismic source and the dispersion characteristics associated with attenuation across the waveguide. Bowheads are a crucial species to consider because of the frequency band in which they call overlaps with the band containing residual seismic energy.

New and better hardware is needed, most importantly: (1) increasing hydrophone sensitivity at high-frequencies; (2) switching to lithium batteries in order to achieve a full year of autonomous data recording capability; (3) simaltaneously deploying upward-looking sonar profilers to explore the complex relationship between sea ice thickness and associated ambient noise levels; (4) developing shallow-water mooring configurations that are safe from ice scours and can be deployed near the coast to monitor marine mammal populations. These improvements will not only increase acoustic recording capability, but will allow for new avenues in signal processing and data analysis.

Social implications for acoustics in a seasonal Arctic include increases in ambient noise levels across the North Slope of Alaska, due in significant part to anthropogenic noise sources like seismic oil exploration, eventual oil and gas extraction, maritime shipping activites and vessel traffic, and possible consequences for marine mammals and the subsistence hunting culture of the North Slope.

REFERENCES

Albers, V. M., "Underwater Acoustics Handbook II," University Park, Pennsylvania State University Press (1965).

Bel'kovitch, V. M. and M. N. Sh'ekotov, "The Belukha Whale: Natural Behavior and Bioacoustics," Translated by M. A. Svanidze, Edited by J. C. Haney and C. Recchia, Woods Hole Oceanographic Institution (1993).

Buck, B. M., "Arctic Acoustic Transmission Loss and Ambient Noise," Arctic Drifting Stations, A Report on Activities Supported by the Office of Naval Research, The Arctic Institute of North America, coordinated by J. E. Sater (1968).

Buck, B. M. and C. R. Green, "Arctic Deep Water Propagation Measurements," J. Acoust. Soc. Am. Vol. 36, pp. 1526-1533 (1964).

Clark, C. W., R. A. Charif, S. G. Mitchell, J. Colby, "Distribution and behavior of the bowhead whale, *Balaena Mysticetus*, based on analysis of acoustic data collected during the 1993 spring migration off Point Barrow, Alaska," Scientific Report, International Whaling Comission 46: 541-552 (1996).

Diachok, O. I., "Arctic Hydroacoustics," Cold Regions Sci. Tech. Vol. 2, pp. 299-321 (1980).

Diachok, O. I., "Effects of Sea-Ice Ridges on Sound Propagation in the Arctic Ocean," J. Acoust. Soc. Am. Vol. 59, No. 5, pp. 1110-1120 (1976).

Diachok, O. I. and R. S. Winokur, "Spatial Variability of Underwater Ambient Noise at the Arctic Ice-Water Boundary," J. Acoust. Soc. Am. Vol. 55, No. 4, pp. 750-753 (1974).

Dyer, I., "Statistics of Sound Propagation in the Ocean," J. Acoust. Soc. Am. Vol. 48, No. 1 (Part 2) (1970).

Dyer, I., "The Song of Sea Ice and Other Arctic Ocean Melodies," Arctic Technology and Policy, edited by I. Dyer and C. Chryssostomidis, McGraw-Hill, New York, pp. 11-37 (1984).

Emery, W. J. and R. E. Thomson, "Data Analysis Methods in Physical Oceanography" 2nd edition, Pergamon Press, Amsterdam, 634 pp (1998).

Foldy, L. L., "The Multiple Scattering of Waves: General Theory of Isotropic Scattering by Randomly Distributed Scatterers," Physical Review Vol. 67, No. 3 & 4, pp. 107-119 (1945).

Ganton, J. H. and A. R. Milne, “Temperature and Wind-Dependent Ambient Noise Under Midwinter Pack Ice” J. Acoust Soc. Am. Vol. 38, pp. 406-411 (1965).

Green, C. R. and B. M. Buck, “Arctic Ocean Ambient Noise,” J. Acoust. Soc. Am. Vol. 36, pp. 1218-1220 (1964).

Kahru, M., “Windows Image Manager—Image display and analysis program for Microsoft Windows with special features for satellite images,” WWW page, http://wimsoft.com (2000).

Kaufman, M., “Perennial Arctic Ice Cover Diminishing, Officials Say,” Washington Post, Pg. A03 (March 19, 2008).

Kibblewhite, A. C. and D. A. Jones, “Ambient Noise Under Antarctic Sea Ice,” J. Acoust. Soc. Am. Vol. 59, No. 4 (1976).

LePage, K. and H. Schmidt, “Modeling of Low-frequency Transmission Loss in the Central Arctic,” J. Acoust. Soc. Am. Vol. 96, No. 3 (1994).

Lewis, J. K. and W. W. Denner, “A Study of Sea Ice Kinematics and Their Relationships to Arctic Ambient Noise,” Report to the Office of Naval Research, Science Applications International Corporation Report No. SAIC 85/1950, pp. 770 (1986).

Lewis, J. K. and W. W. Denner, “Arctic Ambient Noise in the Beaufort Sea: Seasonal Relationships to Sea Ice Kinematics,” J. Acoust. Soc. Am. Vo1. 83, No.2, pp. 549-565 (1988).

Lewis, J. K. and W. W. Denner, “Arctic Ambient Noise in the Beaufort Sea: Seasonal Space and Time Scales,” J. Acoust. Soc. Am. Vo1.82, No.3, pp. 988-997 (1987).

Lewis, J. K. and W. W. Denner, “Higher Frequency Ambient Noise in the Arctic Ocean,” J. Acoust. Soc. Am. Vol. 84, No. 4, pp. 1444-1455 (1988).

Mackenzie, K. V., “Nine-term equation for sound speed in the oceans,” J. Acoust. Soc. Am. Vol. 70, No. 3 (1981).

MacPherson, J. D., “Some Under-Ice Acoustic Ambient Noise Measurements,” J. Acoust. Soc. Am. Vol. 34 (L), pp. 1149-1150 (1962).

Makris, N. C. and I. Dyer, “Environmental Correlates of Arctic Ice Edge Noise,” J. Acoust. Soc. Am. Vol. 90, No. 6 (1991).

Makris, N. C. and I. Dyer, “Environmental Correlates of Pack Ice Noise,” J. Acoust. Soc. Am. Vol. 79, No. 5, pp. 1434-1440 (1986).

McDonald, M. A., J. A. Hildebrand, S. M. Wiggins, “Increases in deep ocean ambient noise in the Northeast Pacific west of San Nicolas Island, California,” J. Acoust. Soc. Am. Vol. 120, No. 2, pp. 711-718 (2006).

Milne, A. R., “Sound Propagation and Ambient Noise Under Sea Ice,” in Underwater Acoustics, edited by V. M. Albers (Plenum, New York), Vol. 2, Ch. 7, pp. 103-137 (1967).

Milne, A. R., “Statistical Description of Noise Under Shore-Fast Sea Ice in Winter,” J. Acoust. Soc. Am. Vol. 39, pp. 1174-1182 (1966)

Milne, A. R., “Thermal Tension Cracking in Sea Ice: A Source of Under Ice Noise,” J. Geophysics Res. Vol. 77, pp. 2177-2192 (1972).

Milne, A. R., “Wind Noise Under Winter Ice Fields,” J. Geophysics Res. Vol. 79, pp. 803-809 (1974).

Milne, A. R. and J. H. Ganton, “A Statistical Description of Noise Under Shore-Fast Sea-Ice in Winter,” Pacific Naval Lab. Report 65-1 (1965).

Milne, A. R. and J. H. Ganton, “Ambient Noise Under Arctic Sea Ice,” J. Acoust. Soc. Am. Vol. 36, No. 5, pp. 855-863 (1964).

Milne, A. R. and J. H. Ganton, “Diurnal Variations in Underwater Noise Beneath Spring-Time Sea Ice,” Nature Vol. 221, pp. 851-852 (1969).

Milne, A. R. and J. H. Ganton, “Noise Beneath Sea Ice and its Dependence on Environmental Mechanisms,” JUA (USN) Vol. 21, pp. 69-81 (1971).

Milne, A. R., J. H. Ganton, and D. J. McMillin, “Ambient Noise Under Sea Ice and Further Measurements of Wind and Temperature Dependence,” J. Acoust. Soc. Am. Vol. 41 (L), pp. 525-528 (1967).

Moore, S. E., K. M. Stafford, D. K. Mellinger, J. A. Hildebrand, “Listening for Large Whales in the Offshore Waters of Alaska,” Bioscience Vol. 56, No. 1, pp. 49-55 (2006).

Payne, F. A., “Effect of Ice Cover on Shallow-Water Ambient Sea Noise,” J. Acoust. Soc. Am. Vol. 36, pp. 1943-1947 (1964).

Pritchard, R. S., “Arctic Ocean Background Noise Caused by Ridging of Sea Ice” J. Acoust. Soc. Am. Vol. 75, No. 2 (1984).

Pritchard, R. S., “Mechanical Behavior of Pack Ice,” in Mechanics of Structured Media, edited by A.P.S. Selvadurai (Elsevier, Amsterdam), pp. 371-405 (1981).

Risch, D., C. W. Clark, P. J. Corkeron, A. Elepfandt, K. M. Kovacs, C. Lydersen, I. Stirling, S. M. Van Parijs, “Vocalizations of male bearded seals, *Erignathus barbatus*: classification and geographical variation,” Animal Behaviour, Vol. 73, No. 5, pp. 747-762 (2007).

Ross, D., “Mechanics of Underwater Noise,” Pergamon, New York, p. 375 (1976).

Spreen, G., L. Kaleschke, G. Heygster, “AMSR-E ASI 6.25 km Sea Ice Concentration Data, V5.2,” Institute of Environmental Physics, University of Bremen, Germany, digital media: www.iup.physik.uni-bremen.de (2008).

Spreen, G., L. Kaleschke, G. Heygster, “Sea Ice Remote Sensing Using AMSR-E 89-GHz Channels,” J. Geophys. Res. Vol. 113, C02S03 (2008).

Squire, V., J. Dugan, P. Wadhams, P. Rottier, A. Liu, “Of Ocean Waves and Sea Ice,” Annu. Rev. Fluid Mech. Vol. 27, pp. 115-168 (1995).

Stafford, K. M., S. E. Moore, M. Spillane, S. M. Wiggins, “Gray whale calls recorded near Barrow, Alaska, throughout the winter of 2003-04,” Arctic, Vol. 60, pp. 167 (2007).

Stirling, I., W. Calvert, H. Cleator, “Underwater Vocalizations as a Tool for Studying the Distribution and Relative Abundance of Wintering Pinnipeds in the High Arctic,” Arctic, Vol. 36, No. 3, pp. 262-274 (1983).

Stroeve, J., M. M. Holland, W. Meier, T. Scambos, M. Serreze, “Arctic Sea Ice Decline: Faster than Forecast,” Geophysical Research Letters, Vol. 34, L09501 (2007).

Suydam, R. S., L. F. Lowry, K. J. Frost, G. M. O’Corry-Crowe, D. Pikok, “Satellite Tracking of Eastern Chukchi Sea Beluga Whales into the Arctic Ocean,” Arctic, Vol. 54, No. 3, pp. 237-243 (2001).

Van Parijs, S. M., K. M. Kovacs, C. Lydersen, “Spatial and Temporal Distribution of Vocalizing Male Bearded Seals – Implications for Male Mating Strategies,” Behaviour, Vol. 138, pp. 905-922 (2001).

Van Parijs, S. M., C. W. Clark, "Long-term mating tactics in an aquatic-mating pinniped, the bearded seal, *Erignathus barbatus*," Animal Behaviour, Vol. 72, No. 6, pp. 1269-1277 (2006).

Webb, S. C. and A. Schultz, "Very Low Frequency Ambient Noise at the Seafloor Under the Beaufort Sea Icecap," J. Acoust. Soc. Am. Vol. 91, No. 3 (1992).

Welch, P., "The use of fast Fourier transform for the estimation of power spectra: A method based on time averaging over short, modified periodograms," IEEE Transactions on Audio and Electroacoustics, Vol. 15, Issue 2, pp. 70-73 (1967).

Wenz, G. M., "Acoustic Ambient Noise in the Ocean: Spectra and Sources," J. Acoust. Soc. Am. Vol. 34, No. 12, pp. 1936-1956 (1962).

Wiggins, S. M., "Autonomous Acoustic Recording Packages (ARPs) for Long-Term Monitoring of Whale Sounds," MTS Journal, Vol. 37, No. 2, pp. 13-22 (2003).

Wiggins, S. M. and J. A. Hildebrand, "High-frequency Acoustic Recording Package (HARP) for Broad-band, Long-term Marine Mammal Monitoring," Symposium on Underwater Technology and Workshop on Scientific Use of Submarine Cables and Related Technologies**,** pp. 551-557 (2007).

Yang, T. C. and C. W. Votaw, "Under Ice Reflectivities at Frequencies Below 1 kHz," J. Acoust. Soc. Am. Vol. 70, No. 3 (1981).

Zakarauskas, P., "Observation of Thermal Ice Cracking in the Arctic Basin," J. Acoust. Soc. Am. Suppl. 1, Vol. 82, No. S30 (1987).

Zakarauskas, P., C. J. Parfitt, J. M. Thorleifson, "Automatic Extraction of Spring-Time Arctic Ambient Noise Transients," J. Acoust. Soc. Am. Vol. 90, No. 1 (1991).